Universitetet i Stavanger
Faculty of Science and Technology

University of Stavanger

Faculty of Science and Technology

MASTER'S THESIS

Study Program/ Specialization: Marine and Offshore Technology	Spring semester, 2021 Open / ~~Restricted~~ access
Writer: Jingyuan Wan	Jingyuan Wan. (Writer's signature)
Faculty supervisor: Prof. Muk Chen Ong Dr. Guang Yin Dr. Shengnan Liu Mr. Petter Moen	
Thesis title: Computational Fluid Dynamics (CFD) Investigations of flow past subsea cover	
Credits (ECTS): 30	
Key words: GRP cover, subsea cover, oscillatory flow, DMD, CFD, overset mesh, lift force, OpenFOAM	Pages: 90 + Enclosure: 0 Stavanger, July 14, 2021 Date/year

Abstract

Glass reinforced plastic (GRP) subsea protection covers are often used to protect offshore pipelines, umbilicals and other important subsea structures from dropped objects released from offshore oil and gas and fishing activities. These covers are often subjected to waves. The study of the GRP subsea cover under wave and current is a challenge, and it is the aim of this study to develop and build a numerical model that can be accurately simulated in response to the experimental implementation difficulties. This study performs a series of numerical simulations of the flow of different geometry structures under different flow condition at a series of KC numbers. The thesis is divided into three main procedures. The Chapter 5, 6 and 7 are the essential parts of this thesis and follow a sequence of modeling, revision, and analysis. In the present study, flows around an oscillating GRP subsea cover and oscillatory flows around a stationary subsea cover are investigated using numerical simulations at three different KC numbers of 5, 11 and 20, which are representative for low, medium and large KC number regions. For comparison, the solid structures of subsea cover are also investigated. The simulations of flows around an oscillating subsea cover are used to compare with the experiments done by SINTEF Ocean (formerly MARINTEK) and validate the present numerical model. This study mainly validates that the drag force and lift force acting on the static subsea cover subjected to the oscillatory flow can be used to predict the forces of flow on a moving subsea cover, which provides the foundation for further studies. It is found that the hydrodynamic forces for the two cases (flows around the oscillating cover and oscillatory flows around the stationary cover) are almost the same, which verifies that the experimental tests of subsea covers with forced motions can be used to study hydrodynamic forces on the stationary cover subjected to waves. The horizontal and vertical force coefficients and the surrounding flow fields around the covers are discussed. For further revision to improve lift forces with different geometry subsea covers is conducted. Three geometry categories are Case 1: cover only shell connected with domain respectively, Case 2: cover on the domain bottom and Case 3: subsea covers with baffles of different lengths. These cases discuss various aspects of the forces on the upper surface of the cover, the effect of the plate, and the effect of the water interaction inside the cover, for fully exploring the mechanism of the interaction between water flow and cover. Finally, the final numerical model that is the best match to the experimental data is determined. For this case, DMD post-processing will be performed to capture the dominant modes that determine flow filed and vorticity.

Table of Contents

List of Figures

List of Tables

1 Introduction

1.1. Background and motivation

Subsea pipelines are commonly used in offshore industries to transport the oil and gas. Subsea covers are made of concretes as well as Glass Reinforced Plastic (GRP) and used to provide overall protection for seabed installations, such as offshore pipelines, umbilical and other important subsea structures, against commercial trawling operations. Especially due to its low-cost, high strength and good corrosion properties, GRP covers have recently been widely used. However, under extreme subsea environmental conditions, the subsea covers are subjected to waves and currents, which induce complex vortex systems around them. Furthermore, the stability of the subsea covers on the seabed is highly affected by the hydrodynamic forces on them. Therefore, it is of great significance to investigate the hydrodynamic forces on the subsea covers subjected to waves and currents for safety design and installations.

The GRP covers (Figure 1.1) are produced in various shapes and sizes, and often in the form of elongated ribs to cover pipeline segments. Many experimental and numerical studies have been conducted to investigate the flow over such bottom-mounted structures with different shapes. The pressure distributions around square wall-mounted structures subjected to a turbulent boundary layer were studied using experiments by Arie et al. (1975). Martinuzzi et al (1993) investigated flow over square ribs with varying spanwise lengths and it was found that the flow around rib structures with $W/D > 10$ (where W denotes the spanwise length of the rib structures and D denotes the height of the structures) can be considered as 2D. Liu et al. (2008) used experiments to study the spatio-temporal behaviors of the separation and reattachment of turbulent flows over a two- dimensional square rib. Apart from experiments, Computational Fluid Dynamics (CFD) was also adopted to investigate the relevant subjects. Tauqeer et al. (2017) conducted numerical simulations using RANS for current flows around subsea covers with different shapes subjected to turbulent boundary layer with different boundary layer thicknesses. Andersen et al. (2020) used RANS simulations for flow around square and trapezoidal wall-mounted structures and analyzed the effects of the edge angles on the hydrodynamic forces and the surrounding flow fields. Yin et al. (2020) investigated the turbulent boundary layer flows over two subsea covers with different distances using RANS simulations.

Figure 1.1 GRP cover

Most of these mentioned studies focused on bottom-mounted structures subjected to steady currents. There are few studies considering these bottom-mounted structures subjected to waves. So far, many works investigated cylindrical structures subjected to waves and the wave-induced flows were often simplified by sinusoidal oscillatory flows in Chen et al. (2008), An et al. (2011), Yang et al. (2013, 2014) Tong et al. (2017) and Xiong et al. (2018). Various flow phenomena such as acoustic streaming, Honji instability and transition to turbulence were investigated in these studies. However, simulations of oscillatory flows around subsea covers have not been performed and analysis of hydrodynamic forces caused by oscillatory flow on the structures have not been reported. In experiments, the oscillatory flow conditions are often difficult to achieved. Therefore, forced motions and towing of subsea covers are used to mimic the wave effects. However, the equivalence to the situation where the stationary subsea covers subjected to oscillatory flow has not been discussed in detail.

However, the experiments that conducted by MARINTEK SINTEF only can measure the horizontal and vertical forces by using forced motion and towing to mimic the wave forces. The main purpose of the present study is to discuss how to build a proper numerical model to predict the hydrodynamic forces on subsea covers under oscillatory flow. To fully utilize the experimental data for validating the numerical model, numerical simulations are used to study both flow around an oscillating subsea cover and oscillatory flow around a static subsea cover under the same KC number. The numerical simulations results are compared with the experimental data under different KC number to validate the numerical model.

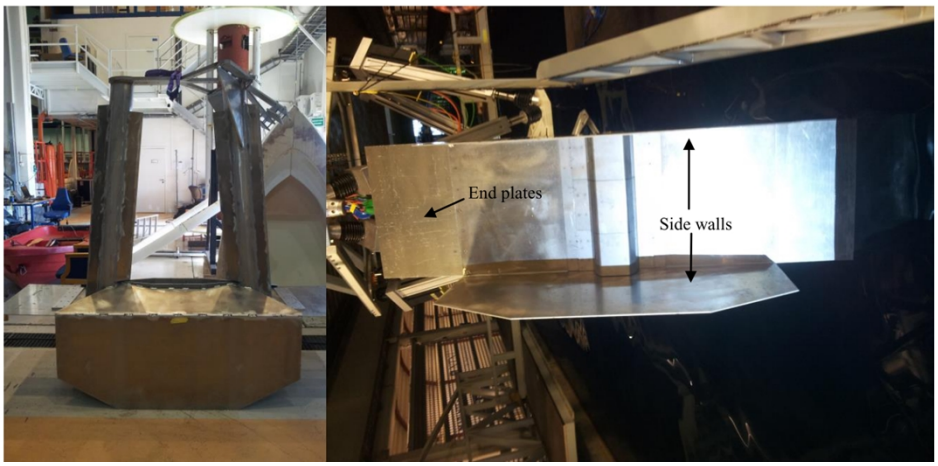

Figure 1.2 The actual experimental set up done by SINTEF Ocean (formerly MARINTEK)

To further extracting the dominant flow features obtained using numerical simulations, Dynamic Mode Decomposition (DMD) is used to perform postprocessing of the flow data to understand the physics of the coherent structures in the flow field. The overall goal of this modal decomposition analysis is to first extract the building blocks (which is called modes that play a dominant role in the dynamical evolution of the flow system) of the flow field and then build a reduced order model to describe the spatial and temporal behavior of the flow. Therefore, finding a suitable basis to represent the whole flow field information will be closely related to these objectives. There are also different modal decomposition methods. Proper Orthogonal Decomposition (POD) has been widely used to capture the dominant characteristics of large-scale energetic coherent structures and build a low-dimensional representation of the turbulent flow fields using only a finite number of modes according to Podvin (2009) and Lehnasch et al. (2011) to capture the dominant flow feature with largest energy fraction. Despite this property, it is well known that POD-based Reduced-order models are inherently inaccurate due to truncation errors if there are some transient modes with large energy but decay fast along their temporal evolutions. Therefore, in order to obtain both spatial and temporal behavior of the coherent structures, the DMD method proposed by Schmid (2010) is used in this paper. This algorithm extracts dynamically relevant flow features from time series of experimental or numerical model data, and decomposes the flow field into structural, amplitude and temporal properties of the modes by using Koopman operator to describe the flow field and even to predict the flow field at future time steps.

1.2. Problem Definition and Objectives

In the present study, numerical simulations are performed to study both flows around an oscillating subsea cover and oscillatory flow around a stationary subsea cover under the same KC number. And a series of cases under different conditions (flow conditions and subsea cover geometries) are also studied and compared against experimental data for evaluating the feasibility of the numerical model. The results of the numerical simulation for an oscillating subsea cover cases are compared with the experiments conducted by SINTEF Ocean (formerly MARINTEK). In their experiments, a GRP cover is attached to a hexapod. The forced motions of the cover are imposed by the hexapod. The setup is shown in the Figure 1.2. Two vertical side walls are also attached along with the cover and are used to force a two-dimensional horizontal flow. The regular motions are sinusoidal in horizontal direction. The forcing period T is fixed at $T = 4.01s$ and the amplitude is adjusted to achieve desired KC numbers. A total number of 25 KC numbers in the range of $1 \leq \mathrm{KC} \leq 25$ are tested in this experiment. The numerical results of the present study can further prove that this experimental set up can be used to study the subsea cover subjected to oscillatory flows. Several typical KC numbers which categorize three different flow regions are discussed in the present study.

The objective of this paper is to evaluate a numerical model that provide an alternative of the experiments with high cost. After selecting the most suitable numerical model, the results under different flow conditions can be analyzed and discussed and the surrounding flow fields can be obtained in addition to the hydrodynamic forces. Furthermore, DMD analysis is used to obtain the dominant modes of the flow field and provide a reduced order representation of the flow field that exerting the forces on the subsea cover.

1.3. Structure of the Thesis

Chapter 2 gives a review of the flow characteristics, turbulent boundary layer in which the structures are immersed, and the hydrodynamic forces acting on the subsea cover and gives a brief introduction of the Dynamic Mode Decomposition (DMD) method

Chapter 3 describes CFD, the computational tools and turbulence modeling.

Chapter 4 explains the computational domain, mesh, boundary conditions used to perform the numerical simulations.

Chapter 5 discuss convergence studies, validation studies and provides the results of the hydrodynamic forces on the subsea cover as well as the surrounding flow fields.

Chapter 6 presents the revision of different geometry and structure of cover under oscillatory flow.

Chapter 7 illustrates the Dynamic Mode Decomposition analysis of the numerical simulation results.

Chapter 8 gives the conclusion of the master thesis.

Chapter 9 presents recommendations for further work.

2 Theory

2.1 Flow Characteristics

A periodic oscillatory flow around a circular cylinder is characterized by two important flow parameters. The first one is the Reynolds number modified for unsteady flow by replacing the constant current with the amplitude of the oscillation velocity as:

$$Re = \frac{U_m D}{\nu} \tag{2.1}$$

and the second one is the Keulegan-Carpenter number, defined by $\frac{U_m T}{D}$. This parameter can be defined in alternate ways. In a sinusoidal wave, $U_m = \omega x_a$, in which x_a is the (horizontal) water displacement amplitude and KC can be given as:

$$KC = 2\pi \frac{water\ displacement\ amplitude}{cylinder\ diameter} = 2\pi \frac{x_a}{D} \tag{2.2}$$

In the definitions of Re and KC, U_m is the maximum oscillatory velocity, D is the cylinder diameter, ν is the fluid kinematic viscosity, and T is the period of the oscillatory flow. A third often-used Stokes parameter, β, of the oscillatory flow can be defined as $\beta = \frac{D^2}{\nu T}$, and it is revealed that $\beta = \frac{Re}{KC}$.

2.2 Forces acting on the subsea cover

Drag force of fixed cover in oscillatory water

In steady currents, the force acting on a cylinder in the in-line direction is given by

$$F = \frac{1}{2}\rho C_D D U|U| \tag{2.3}$$

where F is the force per unit length of the cylinder and C_D is the drag coefficient.

And In case of oscillatory flow, there will be two additional contributions to the total in-line force expect drag force:

$$F = \frac{1}{2}\rho C_D D U|U| + m'\dot{U} + \rho V \dot{U} \tag{2.4}$$

in which $m'\dot{U}$ is called the *hydrodynamic-mass force* while $\rho V\dot{U}$ is called the *Froude-Krylov force* where m' is the hydrodynamic mass and V is the volume of the cylinder, which for a unit length of the cylinder reduces to A, the cross-sectional area of the cylinder.

When a body is moved with an acceleration a in stationary water, there will be a force on the body, namely the hydrodynamic mass force. This force is caused by the acceleration of the fluid in the *immediate surroundings* of the body. The hydrodynamic mass is defined as the mass of the fluid around the body which is accelerated with the movement of the body due to the action of pressure. Traditionally, the hydrodynamic mass is written as

$$m' = \rho C_m A \tag{2.5}$$

in which A is the cross-sectional area of the body and the coefficient C_m is called the hydrodynamic-mass coefficient or coefficient of added mass which usually derived by experiments. Usually $C_m < 1$.

The second effect will be that the accelerated motion of the fluid in the *outer-flow region* will generate a pressure gradient according to

$$\frac{\partial p}{\partial x} = -\rho\frac{dU}{dt} \tag{2.6}$$

where U is the velocity far from the cylinder. This pressure gradient in turn will produce an additional force on the cylinder, which is termed the **Froude-Krylov force.** The force on the body due to this pressure gradient can be calculated by the following integration:

$$F_p = -\int_S p\, d\mathbf{S} \tag{2.7}$$

For a *cylinder* with the cross-sectional area A and with unit length, F_p will be

$$F_p = \rho A\dot{U} \tag{2.8}$$

Therefore, the total force F will be write as

$$F = \underbrace{\frac{1}{2}\rho C_D DU|U|}_{\text{Drag force}} + \underbrace{\rho C_m A\dot{U}}_{\text{Hydrodynamic mass force}} + \underbrace{\rho A\dot{U}}_{\text{Froude -Krylova force}} \tag{2.9}$$

The last two term is induced by inertia force, so they are combined to resultant inertia force in the Morison equation:

$$F_{total} = F_{drag} + F_{inertia} \tag{2.10}$$

$$F_I = \rho C_m A\dot{U} + \rho A\dot{U} \tag{2.11}$$

And introduced the dimensionless inertia coefficient $C_M = 1 + C_m$, then the force per unit length acting on the cover can be predicted using the Morison equation with two empirical coefficients:

$$F = \frac{1}{2}\rho C_D D U|U| + \rho C_M A\dot{U} \tag{2.12}$$

The values of the dimensionless force coefficients C_D and C_M can be determined experimentally in a variety of ways.

Drag force of oscillatory cover in still water

As to oscillatory cover in still water, even though the flow around an oscillating cylinder in still water would be kinematically identical to that of an oscillating flow past a fixed cylinder and that the resulting forces would be identical, in fact they are different.

There is no ambient dynamic pressure gradient present in still water so that the first inertia force term above, the Froude-Krylov force, is now identically equal to zero.

$$F = \frac{1}{2}\rho C_D D U|U| + \rho C_m A\dot{U} \tag{2.13}$$

$$U = U_m \sin(\theta) \tag{2.14}$$

$$\theta = \frac{2\pi}{T}t \tag{2.15}$$

The values of the drag coefficient and the hydrodynamic-mass coefficients for various two- and three-dimensional bodies can follow by Keulegan and Carpenter (1958):

$$C_m = \frac{KC}{\pi^3}\frac{1}{\frac{1}{2}\rho U_m^2 BD}\int_0^{2\pi} F_c \cos(\theta)\, d\theta \tag{2.16}$$

$$C_d = \frac{3}{8}\frac{1}{\frac{1}{2}\rho U_m^2 BD}\int_0^{2\pi} F_c \sin(\theta)\, d\theta \tag{2.17}$$

$\theta = \frac{2\pi}{T}.U_m$, T, B and D are the amplitude of ambient velocity, period of oscillation, length of the cover normal to flow direction and height of the section/cover, respectively. $F_c$is the measured/calculated force.

Lift force

Expect for the force acting on the cylinder in the in-line direction (the drag force) does change periodically in time oscillating around mean drag, there exists a non-zero force component (with a zero mean, however) on the cylinder (the lift force), even though the incoming flow is completely symmetric with respect to the cylinder axis.

The expression for lift force is similar to drag force:

$$F_L = \frac{1}{2}\rho C_L D U^2 \tag{2.18}$$

C_L is the hydrodynamics coefficient of lift.

2.3 Dynamic Mode Decomposition

2.3.1 General description and solution

The Dynamic Mode Decomposition (DMD) is a data processing algorithm that extracts coherent structures with their single temporal frequency from a numerical or experimental data. It can be thought of as a model reduction or low-dimensional technique. DMD is a snapshot-based post-processing algorithm that provides a spatiotemporal decomposition of huge amount of time and spatial resolved flow data into a finite number of modes. The aim of the method is to develop a reduced order representation of snapshots from a dynamical system and provide temporal information and the spatial structures of the dominant modes used to build the reduced order model as

$$u(x,y,z) \approx \sum_{i=1}^{N} a_i \phi_i(x,y,z) \exp(\lambda_i t)$$

where ϕ_i is the spatial mode with their amplitude a_i and λ_i is the complex frequency of each mode ($\mathrm{Re}(\lambda_i)$ is the temporal growth and $\mathrm{Im}(\lambda_i)$ is the frequency).

To achieve this, the algorithm can be outlined as follows: The data $\boldsymbol{X}$ collected N snapshots into a matrix as:

$$\boldsymbol{X} = [\boldsymbol{u_1}, \boldsymbol{u_2}, \boldsymbol{u_3}, \ldots, \boldsymbol{u_N}] \in \mathbb{C}^{3m \times N} \tag{2.19}$$

where $3m$ stands for the 3 components of velocity $\boldsymbol{u}$, $\boldsymbol{v}$, of number of m spatial points saved per time snapshot. It should be pointed out that in the present study, as 2D simulations are conducted, only the velocity components ($\boldsymbol{u}$, $\boldsymbol{v}$) can be considered and the dimension of the matrix $\boldsymbol{X}$ can be $2m$.

$$\boldsymbol{X} = \begin{bmatrix} \boldsymbol{u}(x_1,y_1,z_1,t_1) & \boldsymbol{u}(x_1,y_1,z_1,t_2) & \cdots & \boldsymbol{u}(x_1,y_1,z_1,t_N) \\ \boldsymbol{u}(x_2,y_2,z_2,t_1) & \boldsymbol{u}(x_2,y_2,z_2,t_2) & & \boldsymbol{u}(x_2,y_2,z_2,t_N) \\ \vdots & \vdots & & \vdots \\ \boldsymbol{u}(x_m,y_m,z_m,t_1) & \boldsymbol{u}(x_m,y_m,z_m,t_2) & & \boldsymbol{u}(x_m,y_m,z_m,t_N) \\ \boldsymbol{v}(x_1,y_1,z_1,t_1) & \boldsymbol{v}(x_1,y_1,z_1,t_2) & & \boldsymbol{v}(x_1,y_1,z_1,t_N) \\ \boldsymbol{v}(x_2,y_2,z_2,t_1) & \boldsymbol{v}(x_2,y_2,z_2,t_2) & \ddots & \boldsymbol{v}(x_2,y_2,z_2,t_N) \\ \vdots & \vdots & & \vdots \\ \boldsymbol{v}(x_m,y_m,z_m,t_1) & \boldsymbol{v}(x_m,y_m,z_m,t_2) & & \boldsymbol{v}(x_m,y_m,z_m,t_N) \\ \boldsymbol{w}(x_1,y_1,z_1,t_1) & \boldsymbol{w}(x_1,y_1,z_1,t_2) & & \boldsymbol{w}(x_1,y_1,z_1,t_N) \\ \boldsymbol{w}(x_2,y_2,z_2,t_1) & \boldsymbol{w}(x_2,y_2,z_2,t_2) & \cdots & \boldsymbol{w}(x_2,y_2,z_2,t_N) \\ \vdots & \vdots & & \vdots \\ \boldsymbol{w}(x_m,y_m,z_m,t_1) & \boldsymbol{w}(x_m,y_m,z_m,t_2) & & \boldsymbol{w}(x_m,y_m,z_m,t_N) \end{bmatrix} \tag{2.20}$$

Next, the key steps of DMD are briefly described. First, DMD begins by collecting a sequence of snapshots from numerical simulations and form a data matrix whose columns represent the individual data samples. The method relies simply on collecting snapshots of data x_k from a dynamical system at a number of times t_k, where $k = 1,2,3,\ldots,N$. M = number of spatial points saved per time snapshot (M=$3m$), N = number of snapshots taken.

$$\boldsymbol{X} = \begin{bmatrix} | & | & & | \\ \boldsymbol{x}_0 & \boldsymbol{x}_1 & \cdots & \boldsymbol{x}_{N-1} \\ | & | & & | \end{bmatrix} \in \mathbb{C}^{M \times N} \tag{2.21}$$

$$\boldsymbol{X}' = \begin{bmatrix} | & | & & | \\ \boldsymbol{x}_1 & \boldsymbol{x}_2 & \cdots & \boldsymbol{x}_N \\ | & | & & | \end{bmatrix} \in \mathbb{C}^{M \times N} \tag{2.22}$$

and postulate that the snapshots have been generated by a discrete-time linear time-invariant system, In the first step, we assume that a linear mapping $\boldsymbol{A}$ connects the flow field x_k to the subsequent flow field x_{k+1}, that is,

$$\boldsymbol{x}_{k+1} = \mathrm{A}\boldsymbol{x}_k \tag{2.23}$$

For fluid flows, the matrix A typically contains a large number of entries (usually complex). Dynamic mode decomposition provides a lower-order representation of a matrix $\mathrm{A} \in \mathbb{C}^{M \times M}$ that captures the dynamics inherent in the data sequence. In fluid problems, the number of

components (measurement points) in each snapshot x_k is typically much larger than the number of snapshots $M \gg N$, thus implying that $\boldsymbol{X}$ and $\boldsymbol{X}'$ are highly tall rectangular matrices.

And that this mapping is approximately the same over the full sampling interval $[0, (N-1)\,\Delta t]$. If the flow field originates from a nonlinear process, this assumption corresponds to a linear tangent approximation. For slowly varying systems, multiscale parameters can provide the basis for the above assumptions. In the special case of purely linear processes, it is assumed that the constant mapping will not invoke any approximation method. In any case, the assumption of a constant mapping between snapshot x_k will allow us to formulate the flow field sequence as a Krylov sequence.

As the number of snapshots increases and the data series given by $\boldsymbol{X}$ captures the main features of the underlying physical processes, it is reasonable to assume that beyond the critical number of snapshots, the vectors given by (2.2) will be linearly correlated. In other words, adding another flow field $\boldsymbol{x}_k$ to the data sequence will not N improve the vector space spanned by $\boldsymbol{x}_1$. When this limit is reached, we can represent the vector $\boldsymbol{x}_N$ as a previous and linearly independent vector vi with k = 1, ... according to the following equation, a linear combination of $N-1$:

$$\boldsymbol{X}' = \begin{bmatrix} | & | & & | \\ \boldsymbol{x}_1 & \boldsymbol{x}_2 & \dots & \boldsymbol{x}_N \\ | & | & & | \end{bmatrix} = \begin{bmatrix} | & | & & | \\ \boldsymbol{A}\boldsymbol{x}_0 & \boldsymbol{A}\boldsymbol{x}_1 & \dots & \boldsymbol{A}\boldsymbol{x}_{N-1} \\ | & | & & | \end{bmatrix} = \boldsymbol{A}\boldsymbol{X} \tag{2.24}$$

The goal of DMD then is the extraction of the dynamic characteristics (eigenvalues, eigenvectors, pseudo eigenvalues, energy amplification, resonance behavior, etc.) of N the dynamical process described by $\boldsymbol{A}$ based on the sequence $\boldsymbol{X}$.

For the Rank-r matrix of snapshot $\boldsymbol{X}$, the DMD algorithm provides an optimal representation $\boldsymbol{F} \in \mathbb{C}^{r\times r}$ of the matrix $\boldsymbol{A}$ based on the POD mode spanning of $\boldsymbol{X}$.

$$\boldsymbol{A} \approx \boldsymbol{U}\boldsymbol{F}\boldsymbol{U}^* \tag{2.25}$$

Here, $\boldsymbol{U}^*$ denotes the complex conjugate transpose of the POD mode $\boldsymbol{U}$ matrix, which is obtained from the economic size singular value decomposition (SVD) of $\boldsymbol{X} \in \mathbb{C}^{M\times N}$,

$$\boldsymbol{X} = \boldsymbol{U}\boldsymbol{\Sigma}\boldsymbol{V}^* \tag{2.26}$$

where $\boldsymbol{\Sigma}$ is an r × r diagonal matrix with non-zero singular values $\{\sigma_1,\cdots,\sigma_r\}$ on its main diagonal, and

$$\boldsymbol{U} \in \mathbb{C}^{M\times r} \, with \, \boldsymbol{U}^* \boldsymbol{U} = \boldsymbol{I} \tag{2.27}$$

$$\boldsymbol{V} \in \mathbb{C}^{r\times N} \, with \, \boldsymbol{V}^* \boldsymbol{V} = \boldsymbol{I} \tag{2.28}$$

The matrix $\boldsymbol{F}$ can be determined from the matrices of snapshots $\boldsymbol{X}$ and $\boldsymbol{X}'$ by minimizing the Frobenius norm of the difference between $\boldsymbol{X}'$ and $\boldsymbol{AX}$ with $\boldsymbol{A} = \boldsymbol{UFU}^*$ and $\boldsymbol{X} = \boldsymbol{U\Sigma V}^*$,

$$\text{minimize } \|\boldsymbol{X}' - \boldsymbol{UF\Sigma V}^*\|_{\boldsymbol{F}}^2 \tag{2.29}$$

where the Frobenius norm of the matrix $\boldsymbol{Q}$ is determined by

$$\|\boldsymbol{Q}\|_{\boldsymbol{F}}^2 = \text{trace}(\boldsymbol{Q}^*\boldsymbol{Q}) = \text{trace}(\boldsymbol{QQ}^*). \tag{2.30}$$

It is straightforward to show that the optimal solution to (2.29) is determined by

$$\boldsymbol{F}_{\text{dmd}} = \boldsymbol{U}^*\boldsymbol{X}'\boldsymbol{V\Sigma}^{-1} \tag{2.31}$$

2.3.2 Optimal amplitudes of DMD modes

The matrix $\boldsymbol{F}_{\text{dmd}} \in \mathbb{C}^{r\times r}$ determines the best low-dimensional representation of the inter-snapshot mapping $A \in \mathbb{C}^{M\times M}$ on the subspace covered by the POD pattern. The dynamics of the r-dimensional subspace is controlled by

$$\boldsymbol{x}_{k+1} = \boldsymbol{F}_{\text{dmd}}\boldsymbol{x}_k \tag{2.32}$$

You can also use the matrices of POD mode $\boldsymbol{U}$ to map xt to a higher dimensional spatial $\mathbb{C}^M$,

$$\boldsymbol{X}_k \approx \boldsymbol{U}\boldsymbol{x}_k \tag{2.33}$$

If $\boldsymbol{F}_{\text{dmd}}$ has a whole martinet of linearly independent eigenvectors $\{y_1,\cdots,y_r\}$, has an eigenvalue for each object $\{\lambda_1,\cdots,\lambda_r\}$, then put it in diagonal coordinate form,

$$\boldsymbol{F}_{\text{dmd}} = \underset{Y}{[y_1 \quad \cdots \quad y_r]} \underset{D_\lambda}{\begin{bmatrix}\lambda_1 & & \\ & \ddots & \\ & & \lambda_r\end{bmatrix}} \underset{Z^*}{\begin{bmatrix}z_1^* \\ \vdots \\ z_r^*\end{bmatrix}} \tag{2.34}$$

the solution to (2.35) is determined by

$$x_k = YD_\lambda^k Z^* x_0 = \sum_{i=1}^{r} y_i \lambda_i^k z_i^* x_0 = \sum_{i=1}^{r} y_i \lambda_i^k a_i \tag{2.35}$$

Where $a_i = z_i^* x_0$ represent the ith modal contribution of the initial condition x_0. Therefore, you can use linear combinations in DMD mode to estimate experimental or numeric snapshots:

$$\boldsymbol{\phi}_i = \boldsymbol{U} y_{\mathrm{i}} \tag{2.36}$$

$$\boldsymbol{X} \approx \boldsymbol{U}\boldsymbol{x}_k = \sum_{i=1}^{r} \boldsymbol{\phi}_i \lambda_i^k a_i,\ k \in \{0,\ldots,N-1\}, \tag{2.37}$$

And a_i can be interpreted as the "amplitude" of the corresponding DMD mode. Note that the choice of amplitude a_i can be interpreted as the choice of Koopman mode that has the strongest effect on the response of the system resulting from the use of certain initial conditions and the time interval in which snapshots are collected. cf. (2.37) Equally, in matrix format:

$$\boldsymbol{X} \approx \underbrace{[\boldsymbol{\phi}_1\ \boldsymbol{\phi}_2\ \ldots,\boldsymbol{\phi}_r]}_{\text{Modes } \Phi}{}_{3m\times N} \times \underbrace{\begin{bmatrix} a_1 & & 0 \\ & a_2 & \\ 0 & & a_r \end{bmatrix}_{r\times r}}_{\text{Amplitude } D_a = diag_{\{a\}}} \times \underbrace{\begin{bmatrix} 1 & \lambda_1^1 & \lambda_1^2 & \lambda_1^3 & \cdots & \lambda_1^{N-1} \\ 1 & \lambda_2^1 & \lambda_2^2 & \lambda_2^3 & \cdots & \lambda_2^{N-1} \\ \vdots & & \ddots & & & \vdots \\ 1 & \lambda_r^1 & \cdots & & \cdots & \lambda_r^{N-1} \end{bmatrix}_{r\times N}}_{\text{Vandermonde matrix } \mathrm{V_{and}}} \tag{2.38}$$

$$\approx [a_1\boldsymbol{\phi}_1\ a_2\boldsymbol{\phi}_2\ \ldots,a_r\boldsymbol{\phi}_r] \times \begin{bmatrix} 1 & \lambda_1^1 & \lambda_1^2 & \lambda_1^3 & \cdots & \lambda_1^{N-1} \\ 1 & \lambda_2^1 & \lambda_2^2 & \lambda_2^3 & \cdots & \lambda_2^{N-1} \\ \vdots & & \ddots & & & \vdots \\ 1 & \lambda_r^1 & \cdots & & \cdots & \lambda_r^{N-1} \end{bmatrix}_{r\times N} \tag{2.39}$$

$$\approx \left[\begin{array}{c|c|c|c|c} a_1\boldsymbol{\phi}_1 + a_2\boldsymbol{\phi}_2 + \ldots + a_r\boldsymbol{\phi}_r & a_1\boldsymbol{\phi}_1\boldsymbol{\lambda_1} + a_2\boldsymbol{\phi}_2\boldsymbol{\lambda_2} + \ldots + a_r\boldsymbol{\phi}_r\boldsymbol{\lambda_r} & a_1\boldsymbol{\phi}_1\boldsymbol{\lambda_1^2} + a_2\boldsymbol{\phi}_2\boldsymbol{\lambda_2^2} + \ldots + a_{\mathrm{r}}\boldsymbol{\phi}_{\mathrm{r}}\boldsymbol{\lambda_{\mathrm{r}}^2} & \ldots\ldots & a_1\boldsymbol{\phi}_1\boldsymbol{\lambda_1^{N-1}} + a_2\boldsymbol{\phi}_2\boldsymbol{\lambda_2^{N-1}} + \ldots + a_{\mathrm{r}}\boldsymbol{\phi}_{\mathrm{r}}\boldsymbol{\lambda_{\mathrm{r}}^{N-1}} \end{array}\right]_{1\times N} \tag{2.40}$$

The core idea of DMD is to decompose the r snapshots of the flow field data over time into modes, amplitude and dynamics that expanded by space and time, which are analyzed. A schematic overview is provided in Figure 2.1.

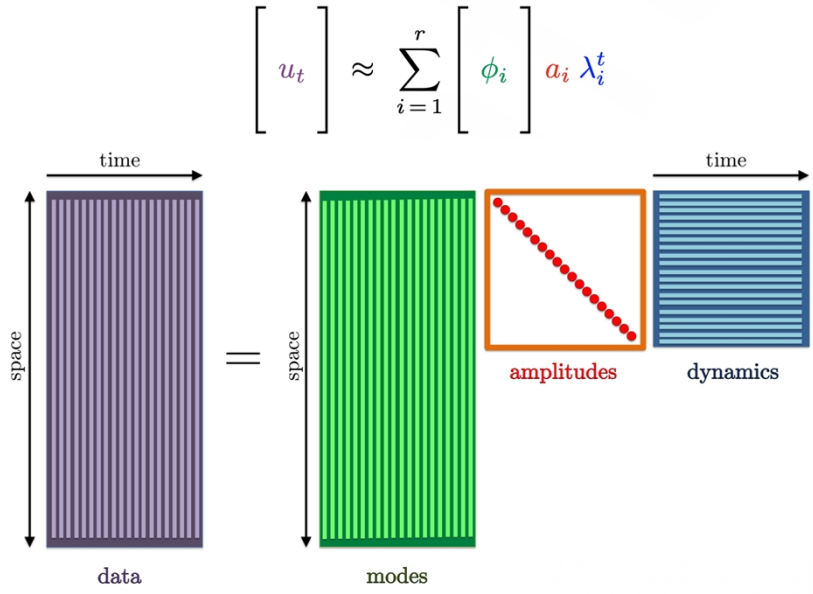

Figure 2.1 The Dynamic Mode Decomposition (DMD) schematic overview

Eq. (2.38) shows that the temporal evolution of the dynamic modes is governed by the Vandermonde matrix $\mathrm{V}_{\mathrm{and}} \in \mathbb{C}^{r\times N}$, which determined by the eigenvalue for $\boldsymbol{F}_{\mathrm{dmd}}$. And due to complex, each eigenvalue λ_i can be written as

$$\begin{aligned} \lambda_i &= e^{N(i\omega_i+\omega_r)\Delta t} \\ &= e^{N\omega_r\Delta t} * e^{iN\Delta t\omega_i} \\ &\quad \text{Real} \quad \text{Imag} \\ &= e^{N\omega_r\Delta t} * [\cos(N\Delta t\omega_i) + i\sin(N\Delta t\omega_i)] \end{aligned} \tag{2.41}$$

therefore it can be deduced,

$$\omega_i = \mathrm{Real}\left(\frac{\ln(\lambda_i)}{\Delta t}\right) \tag{2.42}$$

$$\omega_r = \mathrm{Imag}\left(\frac{\ln(\lambda_i)}{\Delta t}\right) \tag{2.43}$$

ω_i is underlying temporal frequencies and ω_r represents growth/decay rates.

Then, determination of the unknown vector of amplitudes $D_a = diag_{\{a\}}$ is to find the solution of the optimization equation:

$$\text{minimize} \quad \|\boldsymbol{X} - \Phi D_a \mathrm{V}_{\mathrm{and}}\|_F^2 \tag{2.44}$$

By using SVD of $\boldsymbol{X}$ from Eq. (2.26) and combining the Eq. (2.36), the equation comes to:

$$\text{minimize } J(a) = \|\boldsymbol{\Sigma V}^* - \mathrm{Y} D_a \mathrm{V}_{\text{and}}\|_F^2 \tag{2.45}$$

where $J(a)$ is the least-squares approximation.

2.3.3 Sparsity-promoting dynamic mode decomposition

In this section we turn our attention to the problem of choosing the subset of DMD modes that has the greatest impact on the quality of the approximation of a particular sequence of snapshots. In other words, we are interested in a hierarchical description of the data sequences with respect to a series of dynamic modes. Our approach to dynamic mode decomposition, which promotes sparsity, consists of the following two steps:

1. The first step is to find a sparsity structure that satisfies the user's definition, has the smallest possible number of modes among all the extracted mods but contains the key information, high quality of approximation and the minimum approximation error.

The term **card** (a), that penalizes the number of non-zero elements in the vector of unknown amplitudes a, and γ are added to approach the problem of inducing sparsity:

$$\text{minimize } J(a) + \gamma \mathbf{card}\,(a) \tag{2.46}$$

γ is a positive regularization parameter that reflects the degree of weight of sparsity of the vector $a \in \mathbb{C}^r$. To simplify this problem, a relaxed version of (2.46) is introduced by replacing the cardinality function by the ℓ_1-norm of the vector a.

$$\text{minimize } J(a) + \gamma \sum_{i=1}^{r} |a_i| \tag{2.47}$$

2. In the second step, after the sparsity structure has been determined in the first step, the vector of amplitudes is modified to determine the optimal value for the non-zero amplitudes.

$$\text{minimize } J(a) \text{ subject to } E^T a = 0 \tag{2.48}$$

where the matrix $E \in \mathrm{R}^{r \times m}$ encodes information of vector a.

In conclusion, step 1 identified the location of non-zero entries of vector a and step 2 optimize the values of these non-zero entries for the best approximation of the whole data sequence.

3 Computational Fluid Dynamics

3.1 Introduction to CFD

Computational Fluid Dynamics (CFD) is the process of mathematically modelling and numerically solving physical phenomena involving fluid flow using computational softwares or codes. CFD is the product of the combination of recent fluid mechanics, numerical mathematics and computer science, and is a powerful science. It is the approximation of the integral and differential terms in the control equations of fluid dynamics into discrete algebraic forms, making them into sets of algebraic equations, and then solving these discrete sets of algebraic equations by computer to obtain numerical solutions at discrete time/space points.

Mathematical models of the physical case and numerical methods are used in CFD software tools to analyses fluid flows. For example, the Navier-Stokes (N-S) equations are specified as the mathematical model for the physical case. It describes the changes in all these physical properties of both the fluid flow and the heat transfer. The mathematical model depends on the nature of the problem, e.g. heat transfer, mass transfer, phase change or chemical reaction. Furthermore, the reliability of CFD analysis is highly dependent on the overall structure of the process. Validation of the mathematical model is crucial in order to make an accurate case for solving the problem. Furthermore, determining the appropriate numerical solution is key to generating a reliable solution. As the number of physical prototypes can be significantly reduced, CFD analysis is a key element in generating a sustainable product development process.

CFD operations involve three main components: pre-processing, solving, and post-processing. Pre-processing is where the geometry is defined. The generation of the computational domain and mesh is also part of this process. The mesh or grid is the cells into which the domain is divided, and each cell is part of a discretization of the domain. Cells are also referred as elements. In general, increasing the number of elements will produce more accurate numerical results. Finer meshes are needed in domains where larger velocity and pressure gradients occur. Since higher computational cost is associated with finer meshes, the resolution of the mesh depends on the required numerical accuracy and the available computational cost. More than 50% of the time spent solving CFD problems in industry is spent on geometry and meshing (Versteeg & Malalasekera, 2007).

Fluid properties and boundary conditions are also specified in the pre-processing part. Many CFD software packages use the finite volume method (FVM). For example, OpenFOAM, which is employed in the present study, uses a vertex-based FVM approach for discretization. A control volume is built around each cell node or corner where fluid variables are stored. The RANS equations are integrated in each control volume and the discretized equations are solved (Stenmark, 2013). This is the solution part of the CFD problem. Post-processing includes extraction and visualization of the results.

CFD is attractive to the industry because it is often more cost effective than experiments (Sayma, 2009). However, it should be noted that simulations of complex flows are error-prone and require appropriate implementations of meshes, domains, geometries, boundary conditions, a good sense of physical understanding, and preferably reference experimental data to validate the numerical results.

3.2 OpenFOAM

OpenFOAM is the leading free open source software. OpenFOAM is an object-oriented CFD class library written entirely in C++, which uses a similar approach to describe the finite volume discretization of partial differential equations in software as we are used to, supports polyhedral meshes (such as those generated by CCM+ from CD-adapco) and thus can handle complex geometric shapes, with its own snappyHexMesh can quickly and efficiently divide hexahedral + polyhedral meshes with high mesh quality. Massively parallel computation is supported, and GPU optimization for OpenFOAM library is in progress.

In simple terms, OpenFOAM is a collection of C++ programs written for different flows, each of which can be represented by a series of partial differential equations, and the code that solves the partial differential equations for this motion is a solver for OpenFOAM. For a simple laminar motion of a single-phase Newtonian fluid, icoFoam can be solved.

The software is organized through a set of applications and libraries and is controlled through text files and terminal commands. The OpenFOAM simulation example consists of various directories containing information about the flow problem, as shown in the example from this study in Figure 3.1.

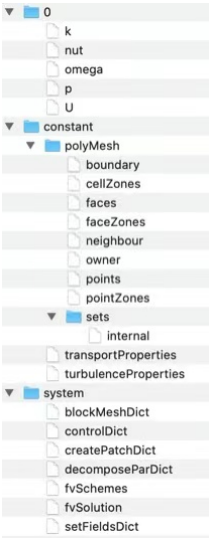

Figure 3.1 Organized OpenFOAM folders for the present study

The 0 directory contains text files that define the boundary conditions for the flow properties that characterize the boundary condition. The constants folder has files containing information about the mesh and the physical boundaries of the simulation. The system folder contains files related to the solver scheme and simulation options.

3.3 Mesh

The first step in creating OpenFOAM is to build a good geometric model and divide it into discrete cells according to its boundary conditions. These cells are called meshes or grids, and the quality and fineness of the mesh division directly determines the accuracy of the numerical simulation and is therefore crucial. Encrypted meshes are required in the region of interest and in areas with large variation gradients to accurately and thoroughly capture critical areas in the boundary layer. It is also necessary to avoid excessive mesh skewness and abrupt changes in mesh size, since OpenFOAM solves the flow problem spatially using a finite volume method. The grid generation software used in this study was Gmsh due to the grid generation tools, scripting options and OpenFOAM support.

Gmsh is a 3D finite element mesh generator with a built-in CAD engine and post-processor. Interactive actions generate script files in the input and vice versa. The integration of code from ASCII text files using Gmsh's own scripting language (.geo files), or C++, C, Python or Julia Application Programming Interface (API) into Gmsh.

3.4 Governing equation and turbulent model

The Reynolds-averaged Navier-Stokes equations for the conservation of mass and momentum for steady-state turbulent flow are given as follows:

$$\frac{\partial u_i}{\partial x_i} = 0 \tag{3.1}$$

$$\frac{\partial u_i}{\partial t} + u_j\frac{\partial u_i}{\partial x_j} = -\frac{1}{\rho}\left(\frac{\partial P}{\partial x_i}\right) + \frac{1\partial^2 u_i}{\nu\partial {x_j}^2} - \frac{\partial \overline{u_i{}'u_j{}'}}{\partial x_j} = 0 \tag{3.2}$$

where i, j = 1, 2 (for x, y) denote the streamwise and cross-stream directions, respectively; u_1 and u_2 (for u and v) are the corresponding mean velocity components. $\overline{u_i{}'u_j{}'}$ is the Reynold stress component where $u_i{}'$ represents the fluctuating part of the velocity; P is the mean pressure; and ρ is the fluid density. Based on the Boussinesq eddy viscosity assumption, the Reynolds stress tensor is expressed by:

$$\overline{u_i{}'u_j{}'} = \tau_{ij} = \nu_t\left(\frac{\partial u_i}{\partial x_j} + \frac{\partial u_j}{\partial x_i}\right) - \frac{2}{3}k\delta_{ij} \tag{3.3}$$

Where ν_t denotes the turbulent eddy viscosity, k represents the turbulent kinetic energy and δ_{ij} is the Kronecker function.

The $k-\omega$ Shear Stress Transport (SST) turbulent model is employed in the present study. The $k-\omega$ SST turbulence model (Menter, 1994) is a two-equation eddy-viscosity model which is used in the present study because of its good performance in predictions of adverse pressure gradients and separating flow around bluff bodies. The $k-\omega$ SST turbulence model is a combination of the standard $k-\omega$ model and the standard $k-\varepsilon$ model. The near wall region of the computational domain is treated with the $k-\omega$ model developed by Wilcox (1998) while the standard $k-\varepsilon$ model developed by Jones & Launder (1973) is applied in the outer wake region and in the free shear layers. According to Menter et al. (2003), the equations of k and ω are expressed as follow:

$$\frac{D(\rho k)}{Dt} = \widetilde{P_k} - \beta^*\rho\omega k + \frac{\partial}{\partial x_j}\left[(\mu + \sigma_k\mu_t)\frac{\partial k}{\partial x_j}\right] \tag{3.4}$$

$$\frac{D(\rho\omega)}{Dt} = \alpha\rho S^2 - \beta\rho\omega^2 + \frac{\partial}{\partial x_j}\left[(\mu + \sigma_\omega\mu_t)\frac{\partial\omega}{\partial x_j}\right] + 2(1-F_1)\rho\sigma_{\omega 2}\frac{1}{\omega}\frac{\partial k}{\partial x_j}\frac{\partial\omega}{\partial x_j} \tag{3.5}$$

where $\widetilde{P_k}$ is given by

$$\widetilde{P_k} = \min\left[\mu_t \frac{\partial u_i}{\partial x_j}\left(\frac{\partial u_i}{\partial x_j} + \frac{\partial u_j}{\partial x_i}\right), 10\beta^* \rho k\omega\right] \tag{3.6}$$

If ϕ_1 represents any constant in the original k–ω model (σ_{k1},…) and ϕ_2 represents any constant in the original k–ε model (σ_{k2},…), then ϕ, the corresponding constant of the new model given by Eqs. (3.4) and (3.5), is

$$\phi = F_1\phi_1 + (1 - F_1)\phi_2 \tag{3.7}$$

$$F_1 = \tanh\left(\arg_1^4\right) \tag{3.8}$$

$$\arg_1 = \min\left[\max\left(\frac{\sqrt{k}}{\beta^*\omega y}, \frac{500\nu}{y^2\omega}\right), \frac{4\rho\sigma_{\omega 2}k}{CD_{k\omega}y^2}\right] \tag{3.9}$$

$$CD_{k\omega} = \max\left(2\rho\sigma_{\omega 2}\frac{1}{\omega}\frac{\partial k}{\partial x_j}\frac{\partial \omega}{\partial x_j}, 10^{-10}\right) \tag{3.10}$$

Here y is the distance to the nearest wall and $CD_{k\omega}$ is the positive portion of the cross-diffusion term of Eq. (3.5).

The turbulent eddy viscosity is defined as

$$\nu_t = \frac{a_1 k}{\max(a_1\omega, SF_2)} \tag{3.11}$$

where S is the invariant measure of the strain rate and F_2 is given by

$$F_2 = \tanh\left(\arg_2^2\right) \tag{3.12}$$

$$arg_2 = \max\left(2\frac{\sqrt{k}}{0.09\omega y}, \frac{500\nu}{y^2\omega}\right) \tag{3.13}$$

The constants of SST are: $\beta^* = 0.09$, $a_1 = 0.31$, $\alpha_1 = 0.5532$, $\alpha_2 = 0.4403$, $\beta_1 = 0.075$, $\beta_2 = 0.0828$, $\sigma_{k1} = 0.85034$, $\sigma_{k2} = 1.0$, and $\sigma_{\omega 1} = 0.5$, $\sigma_{\omega 2} = 0.85616$.

OpenFOAM, a license free and open source computational fluid dynamic (CFD) code is used in the present study. OpenFOAM is based on the finite volume method. OpenFOAM solvers, PimpleDyMFoam and pimpleFoam are used in flow around a moving subsea cover cases and oscillatory flow around a static subsea cover respectively. The spatial discretization schemes for gradient, Laplacian and divergence are cellLimited Gauss linear, Gauss linear limited and Gauss linear Upwind. All these schemes are in second order. The second order Euler scheme is used for the time integration.

3.5 Post-processing

The F_x and F_z data are obtained by adding a module to controlDict to obtain forces.dat, which is generated by OpenFOAM and read and plotted by MATLAB. The velocity field, vorticity field and streamline field were also obtained by calculating each time step from the boundary condition 0 directory. All graphs were visualized and plotted with Tecplot360.

4 Computational model

4.1 The experiment setup

In the present study, numerical simulations are performed to study both flows around an oscillating subsea cover and oscillatory flow around a stationary subsea cover under the same KC number. The results of cases are compared with the experiments conducted by Reza Firoozkoohi (2014) (checked by Trygve Kristiansen and approved by Øyvind Hellan) from SINTEF Ocean (formerly MARINTEK). In the experiments, flow around an oscillatory subsea cover was considered and the forces on the subsea cover were measured. The setup is shown in the Figure 4.1 which is Base cover with no edge, 6.5mm gap in the regular motion. The cross section (Figure 4.2) is usually a combination of rectangular at the bottom and trapezoid at the top. Two vertical side walls are also attached along with the cover and are used to force a two-dimensional horizontal flow. The regular motions are sinusoidal in horizontal direction.

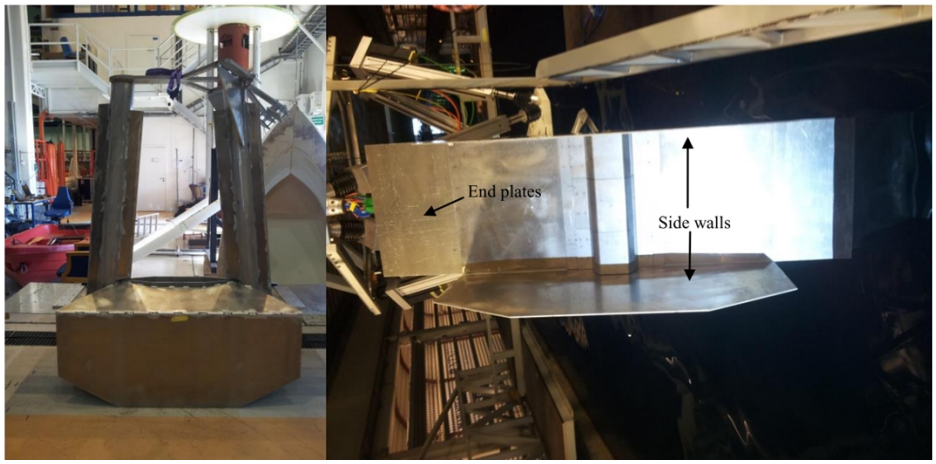

Figure 4.1 The actual experimental set up done by SINTEF Ocean (formerly MARINTEK)

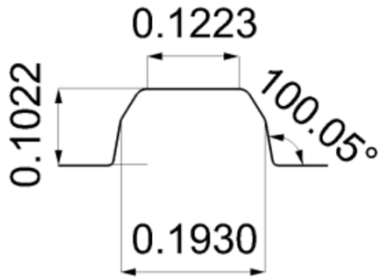

Figure 4.2 Base cover geometry

Hydrodynamic horizontal and vertical forces due to wave and current on a bottom-mounted GRP cover are measured experimentally by forced harmonic motions and towing. Forced motions are applied only in the horizontal direction. Regular motions follow periodic:

$$\eta_1 = Asin\left(\frac{2\pi}{T}t\right) \tag{4.1}$$

T and A are period and amplitude of force motions. And 13 to 25 KC numbers ($KC = \frac{2\pi A}{D}$) were tested in the regular tests. The scale is 15 in model tests and $T = 4.01s$ was used in model scale ($T = 15.53s$ in full scale). The current speed is $U = 0.178\ m/s$ in model scale corresponding to $U = 0.69\ m/s$. The numerical results of the present study can further prove that this experimental set up can be used to study the subsea cover subjected to oscillatory flows. Three typical KC numbers which categorized three different flow regions are discussed in the present study.

Need to mention that since the whole setup was accelerated, the $F_{X\_total\_C}$ should be corrected for the inertia force due to acceleration of frozen mass, cover mass and the transducer bar. Therefore, in the simulation the resulting forces should be subtracted the force influenced by the frozen mass and numerically equaling to F_{FK}.

4.2 Model description

Two-dimensional (2D) simulations are carried out for the same structure shown in Section 4.1 as that used in the experiments done by MARINTEK SINTEF. The sizes of structure are the same with the experimental setup and shown in Figure 4.3. The plate below subsea cover is regarded as the seabed and moves together with the subsea cover. This plate below the subsea cover is also included in the experimental setup.

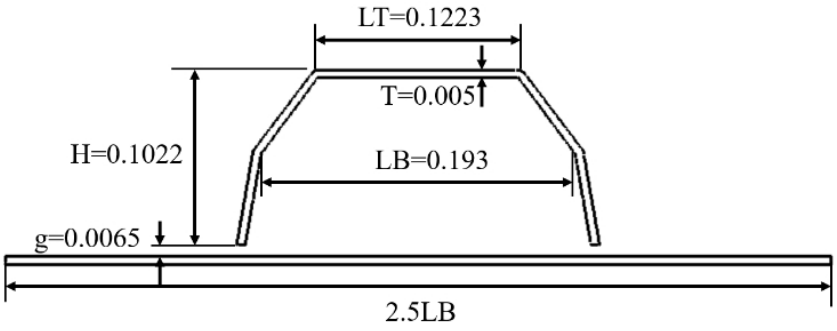

Figure 4.3 The subsea cover simulation model

For validating the simulation in oscillatory which has comparable results with dynamic motion experiment, this study also simulated the whole subsea cover simulation model with the same regular motion as the experiment in still water.

Considering that in the experimental analysis, the water affection under the subsea cover was neglected and the water inside the subsea cover was seen as frozen water, in the study, additional simulations for both moving subsea cover and static subsea cover subjected to an oscillatory flow condition with non-hollow solid subsea cover (shown in Figure 4.4) are also conducted. For this geometry, there is no water inside and the effects caused by the complex interactions between the inside and outside water due to the complicated geometry in Figure 4.2 can be ruled out.

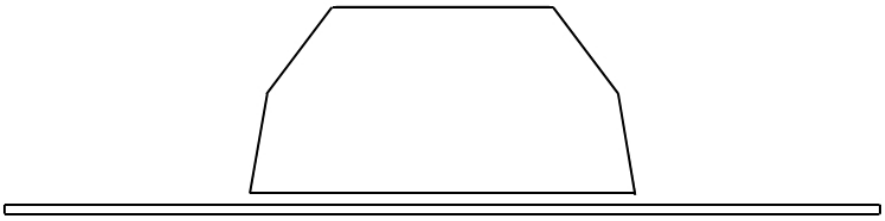

Figure 4.4 the inner-solid subsea cover simulation model

4.3 Computational domain and boundary conditions

Flow around a moving subsea cover

The 2D computational domain for moving subsea cover cases is shown in Figure 4.5. The origin of the coordinates is located at the bottom center of the subsea cover. The height of subsea cover is denoted as H. The size of the computational domain is 20H*8H and the whole setup is 2H from the bottom. The overset mesh region containing the subsea cover and plate is sinusoidal moving during simulations by using the overset function implemented in OpenFOAM.

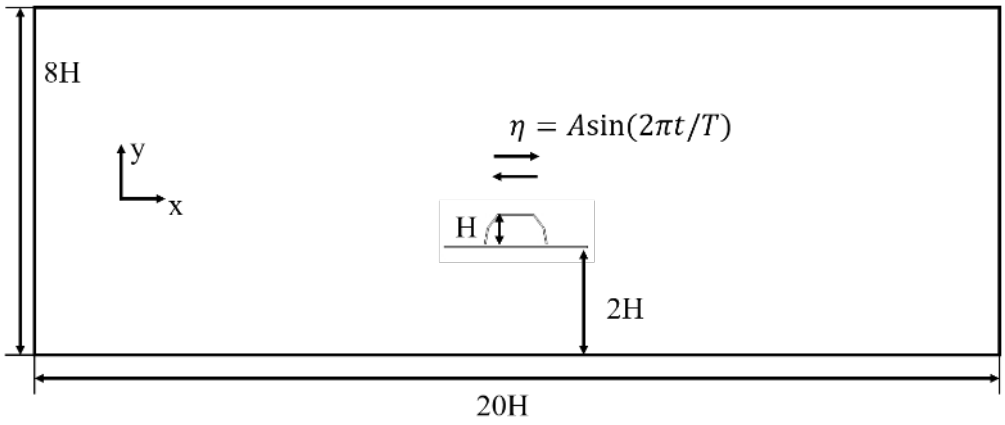

Figure 4.5 The computational domain of dynamic motion cases

The boundary conditions used for the present numerical simulations for moving structure are set as follows:

1. At the inlet, the velocities are set to be zero and the pressure is set as zero normal gradient. k and ω are specified as zero normal gradient.

2. At the outlet, the velocities are set as zero normal gradient and the pressure is set to be zero. k and ω are specified as zero normal gradient.

3. On the surface of the subsea cover and the plate, no slip boundary conditions are applied for the velocities and the wall functions are used for the value of k and ω.

4. At the top and bottom of the boundary conditions, all the quantities are assumed to be symmetry.

Oscillatory flow

For the oscillatory flow cases, a larger computational domain is used to suppress the far-field effects on the structures. The domain is set to be 40H*24H.

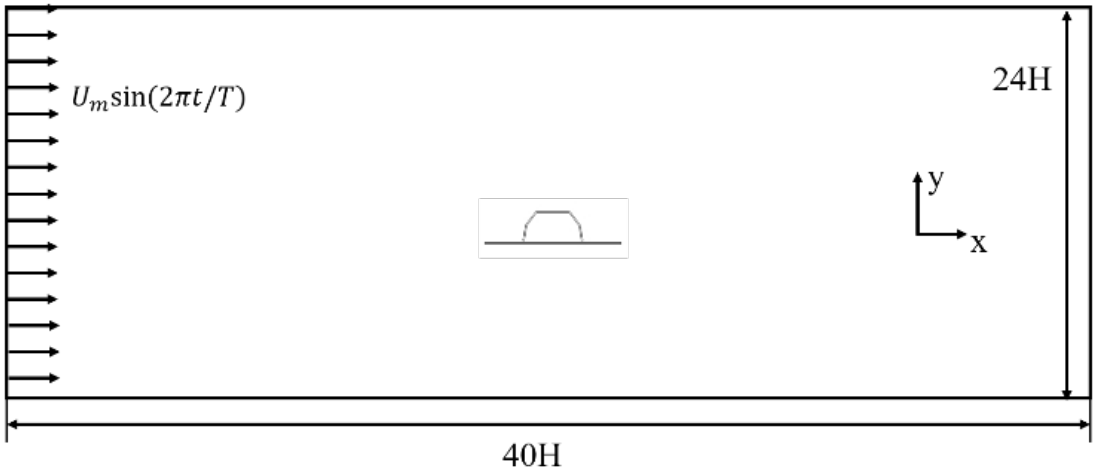

Figure 4.6 the computational domain of oscillatory flow cases

The boundary conditions used for the present numerical simulations for oscillatory flow are set as follows:

1. At the inlet, the velocities are set to be a sinusoidal velocity (U_m) flow and the pressure is set as zero normal gradient. k and ω are specified as zero normal gradient.

2. At the outlet, the velocities are set as zero normal gradient and the pressure is set to be zero. k and ω are specified as zero normal gradient.

3. On the surface of the subsea cover and the plate, no slip boundary conditions are applied for the velocities and the wall functions are used for the value of k and ω.

4. At the top and bottom of the boundary conditions, all the quantities are assumed to be symmetry.

4.4 Oscillatory flow around a static subsea cover

In the present study, oscillatory flow around the subsea cover is investigated. KC number is important governing parameter that influence hydrodynamic forces on the subsea cover. Different values of KC in the simulations are obtained by changing the value of U_m defined as

$$U_m = KC\frac{d}{T} \tag{4.2}$$

where the same T and d are kept in all simulations. Therefore, small KC numbers mean that the orbital motion of the water particles is small relative to the total width of the cylinder. Large

KC numbers, on the other hand, mean that the water particles travel quite large distances relative to the total width of the cylinder, resulting in separation and probably vortex shedding.

4.5 Flow around a moving subsea cover

To validate the present numerical model against the experiments, flow around a moving subsea cover is investigated. The moving subsea cover are oscillating under the same KC number. The hydrodynamic forces on the subsea cover are also compared with those obtained from the simulations of oscillatory flow around a static subsea cover. Overset mesh method is used to treat the moving subsea cover. The benefit of using overset mesh is that highly distorted cells when large motions take place will be avoided. In the overset mesh method, a background static mesh and an overset moving mesh are created and then the two meshes are merged together. The overset moving mesh will move on top of the background fixed mesh. Flow data in the overset mesh regions is interpolated and the information is exchange between the overset mesh and the background mesh.

5 Convergence studies, validation studies and Results and discussion

This section presents and discusses the numerical results under 4 conditions (oscillatory flow around a hollow cover or solid structure; and flow around a moving hollow cover or solid structure) and 4 KC numbers (KC=3, 5, 11, 20). The discussion of the results is based on the horizontal force and vertical force. It worth noting that for the horizontal force, the FK force is subtracted compare the present predicted results with the experimental data.

5.1 Convergence study

The grid resolution study has been carried out for flow around a moving subsea cover using overset mesh under KC=5. Four mesh densities are categorized from coarse to dense grid resolutions are used and the evaluation of the grid resolution is based on the horizontal and vertical forces on the subsea cover. In each case, the cell numbers of the overset moving mesh around the cover (An overview is shown in Figure 5.1) and the background static mesh (An overview is shown in Figure 5.2) increase with 100% based on the mesh density of Case 0 as shown in Table 5.1. The time step for all cases is $\Delta t = 0.0001$ and the maximum Co is kept below 0.4.

Table 5.1 3 different density mesh for grid resolution study

Cases	Overset Mesh No.	Background Mesh No.	$F_{x,\mathrm{rms}}$	$\overline{F_z}$	$F_{z,\mathrm{rms}}$
Mesh 0	14333	24288	1268.1	617.85	328.73
Mesh 1	27765	48195	1167.8	587.93	346.28
Mesh 2	55675	96455	1212.7	536.85	380.03
Mesh 3	135176	192780	1255.7	509.40	384.75

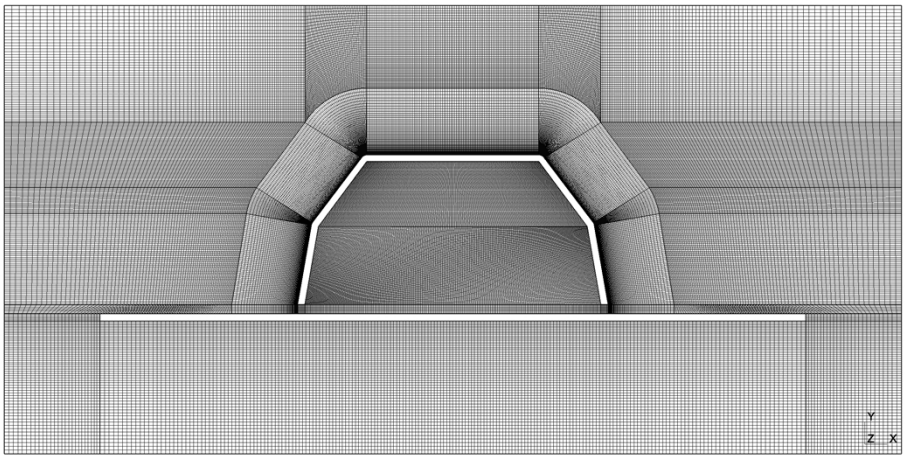

Figure 5.1 Details of the cover mesh for the mesh density of Mesh 3

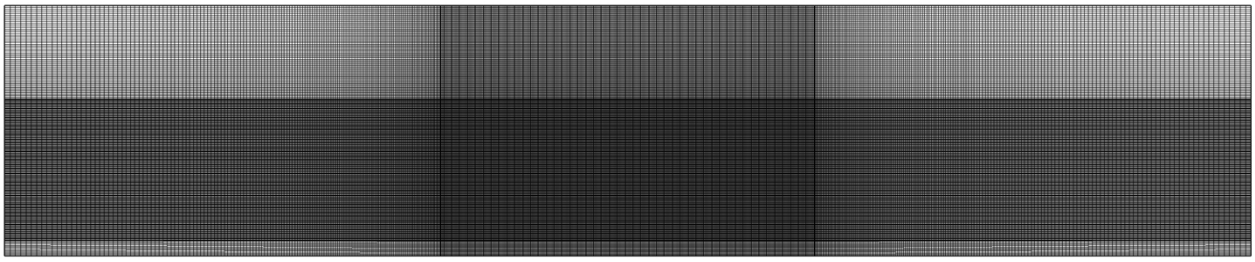

Figure 5.2 Details of the background mesh for mesh density of Mesh 3

The time histories of the horizontal force F_x and the vertical force F_z are shown in Figure 5.3 and Figure 5.4, respectively. It can be obviously seen that the time histories of the forces for different cases are similar, except that there are differences between meshes in the minimal values of F_z due to the sensitivity of the vertical force. The value of $F_{x,\mathrm{rms}}$, time-averaged $\overline{F_z}$ as well as $F_{z,\mathrm{rms}}$ are shown in Table 5.1. It can be seen that the relative differences between cases are reduced to less than 5% for Mesh 2 and 3. Therefore, in general, it can be concluded that Mesh 3 can provide sufficient converged results in terms of the hydrodynamic forces and its grid resolution is used for all the rest simulations. An example of the meshes used is shown in Figure 5.1 and Figure 5.2. In addition, the time-step for Mesh 3 is reduced to $\Delta t = 0.00005$ and the relative differences of the three values are all below 5% which is not shown in detail here. Therefore, it can be concluded that the mesh of Case 3 can provide sufficient converged results in terms of the hydrodynamic forces.

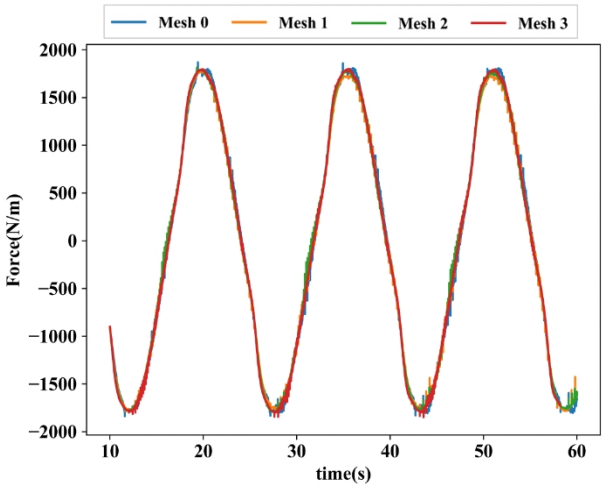

Figure 5.3 Fx of cover in model size for KC=5 dynamic cover

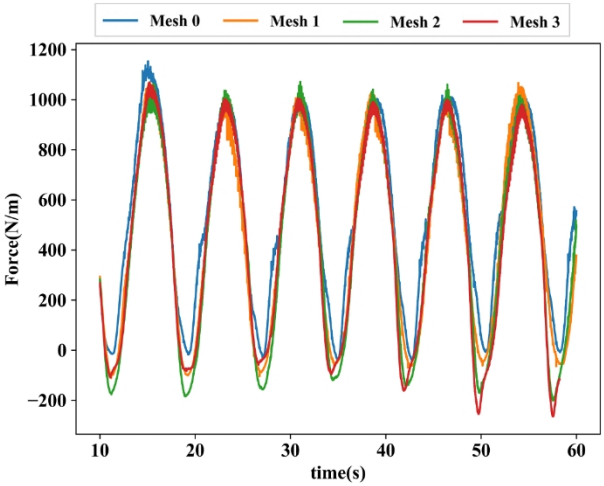

Figure 5.4 Fz of cover in model size for KC=5 dynamic cover

5.2 Comparison of F_x for dynamic motion case and oscillatory flow case in simulation

In the discussion of the following sections, the case name 'OCcover' denotes the oscillatory flow around a cover structure, the case name 'OCsolid' denotes the oscillatory flow around a solid structure, the case name 'dyncover' denotes the flow around an oscillatory cover and the case name 'dynsolid' denotes the flow around a oscillatory solid structure.

For KC=5, the time histories of F_x and F_z of flow around a moving cover and oscillatory flow around a static cover are shown in Figure 5.5. It can be seen that the value of F_x and F_z on the cover for both cases are almost the same. There is a half-period phase difference of F_x between the two cases which is resulted from the difference in the relative direction between the

horizontal flow and the cover. Therefore, it can be concluded that by oscillating a subsea cover under the same KC, the values of both the vertical force and the horizontal force are almost the same with those on a static subsea cover subjected to an oscillatory flow.

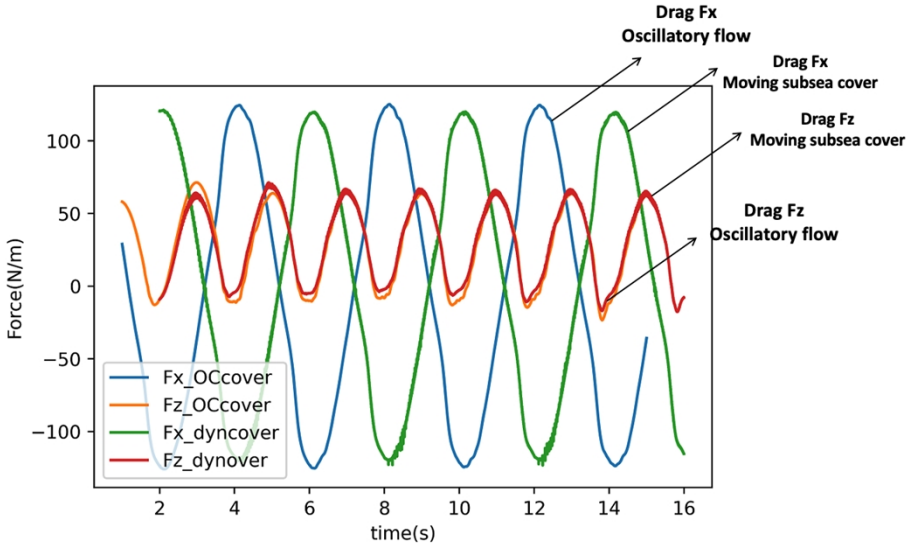

Figure 5.5 Comparsion of Fx and Fz for dynamic motion and oscillatory flow for KC=5 cover case

5.3 Comparison of F_x for KC=3,5,11,20 with the experimental data

The conclusion of section 5.2 above can be further proved by the results under KC=3,5,11,20 for the simulations cases with a solid structure as shown in Figure 5.6 to Figure 5.9. In this section, we mainly focus on the difference between the simulations results and the experimental data for both hollow subsea cover and solid structure cases, as well as the difference between the flow around moving cover cases and the oscillatory flow around a static cover case.

5.3.1 KC=3 and 5

The cases for KC=3 and 5 have the similar results due to the low and similar value of KC number, therefore we can categorize them as a low-KC region. In general, for both the hollow subsea cover shown in Figure 5.6 and Figure 5.7 (a), (b) and solid structure cases shown in Figure 5.6 and Figure 5.7 (c), (d), the time histories of F_x are similar to the experimental data. The maximum value of the present predicted F_x for the subsea cover is slightly larger than that of the experimental data which may be due to the influence of the strong flow into the hollow cover.

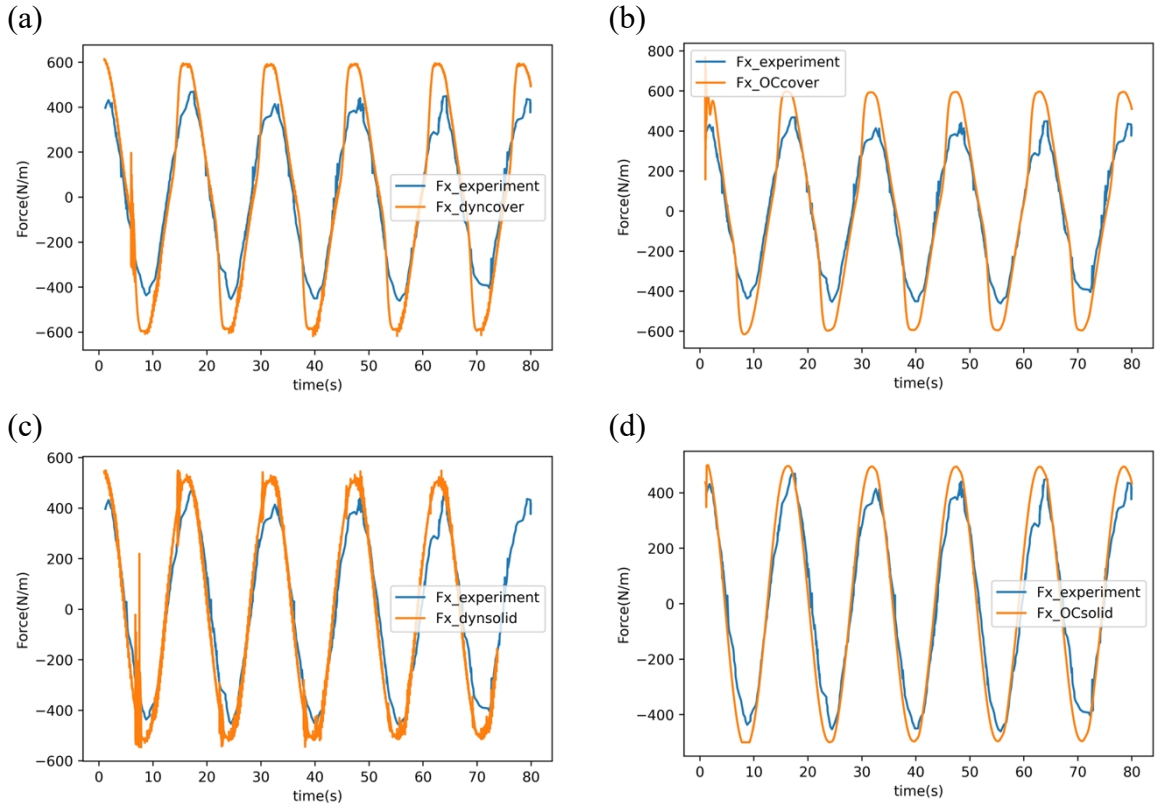

Figure 5.6 Fx comparison for KC=3

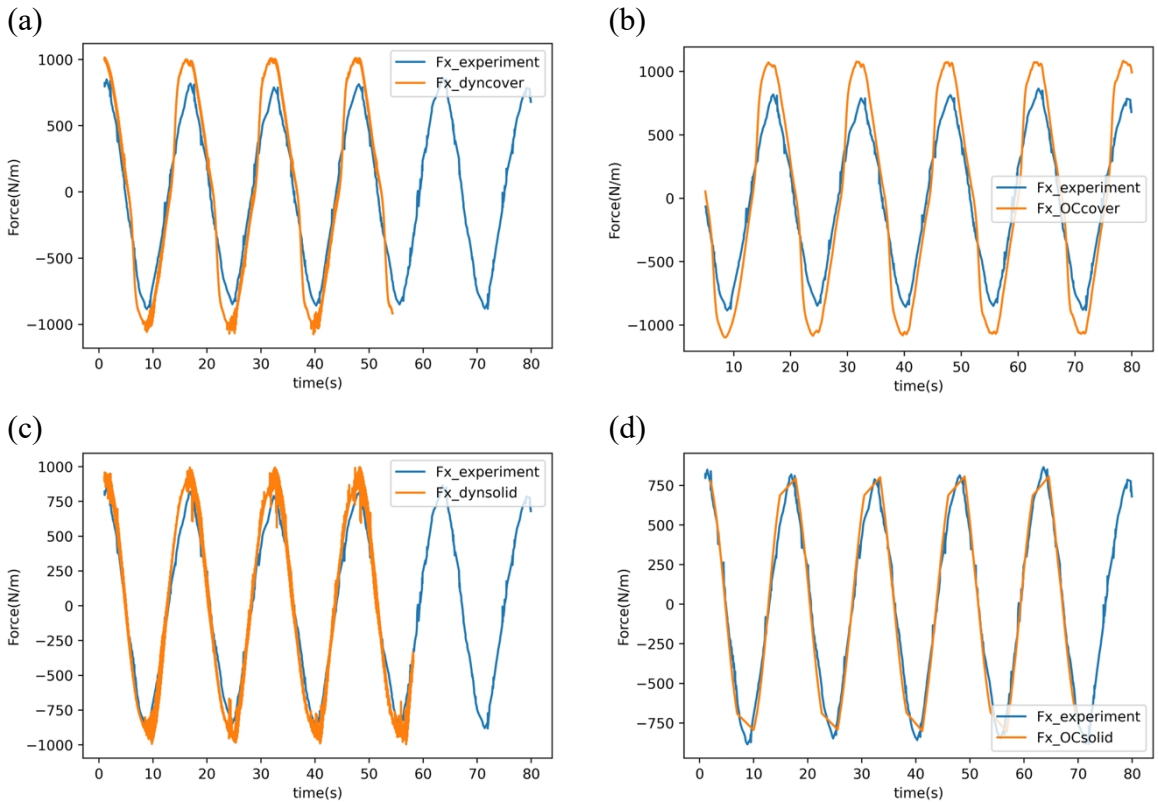

Figure 5.7 Fx comparison for KC=5

5.3.2 KC=11

The cases under KC=11 can be categorized as medium-KC region. The time histories of F_x are shown in Figure 5.8. The results of hollow cover cases and oscillatory flow around a solid structure case for KC=11 agree with the experimental data. However, for the oscillating solid structure case there is obvious maximum amplitude difference compared with the experimental data.

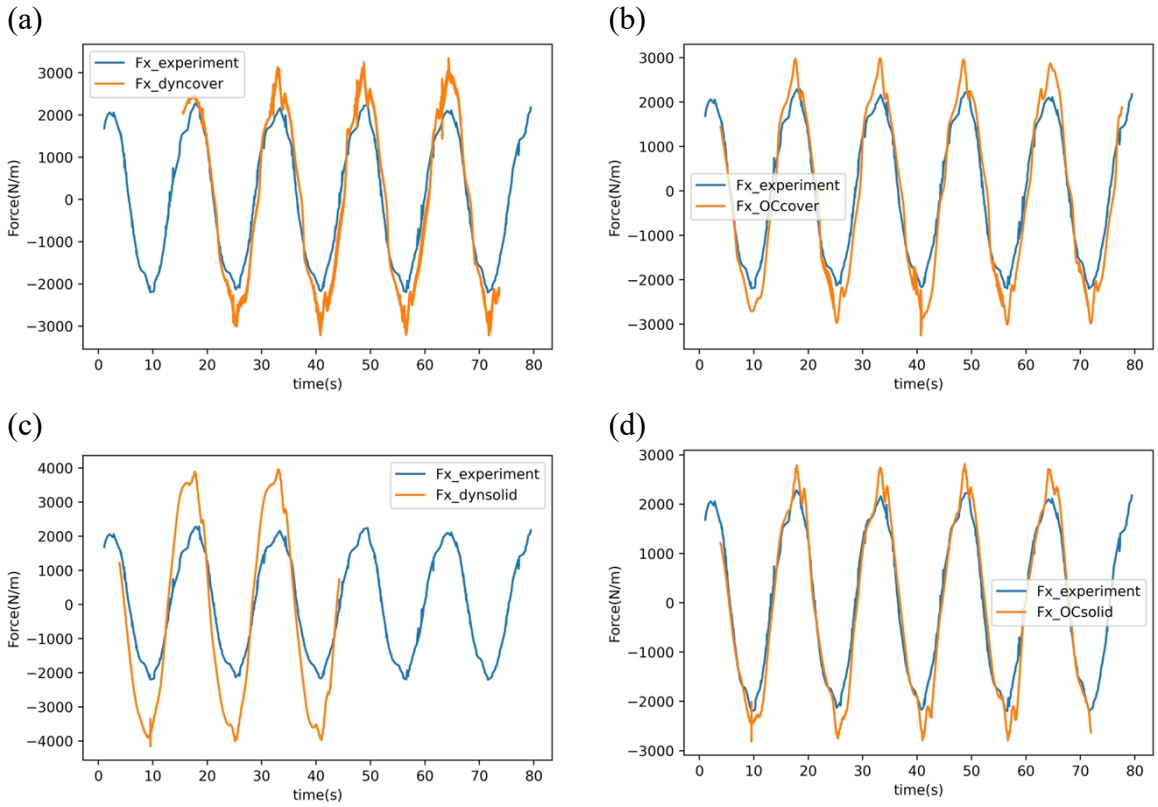

Figure 5.8 Fx comparison for KC=11

5.3.3 KC=20

Figure 5.9 shows the comparison of the time histories of F_x between the present numerical results under KC=20 with the experimental data under KC=19 and KC=21. It can be seen that the overall present predicted values of all cases match well with the experimental data. It should be mentioned that under this large KC, the maximum displacements of the oscillating cover cases are large and since the cell sizes of the background meshes far from the center of the domain is large, there is a large transition in the cell sizes from the dense overset mesh to the relatively coarser background mesh. Therefore, there is much noise on the crests and troughs of the F_x value. However, because of the conclusion that F_x and F_z obtained by oscillating the

structure and oscillatory flow case are almost equal for the cover cases, if neglecting the noise, the conclusion also can still be applied to these cases.

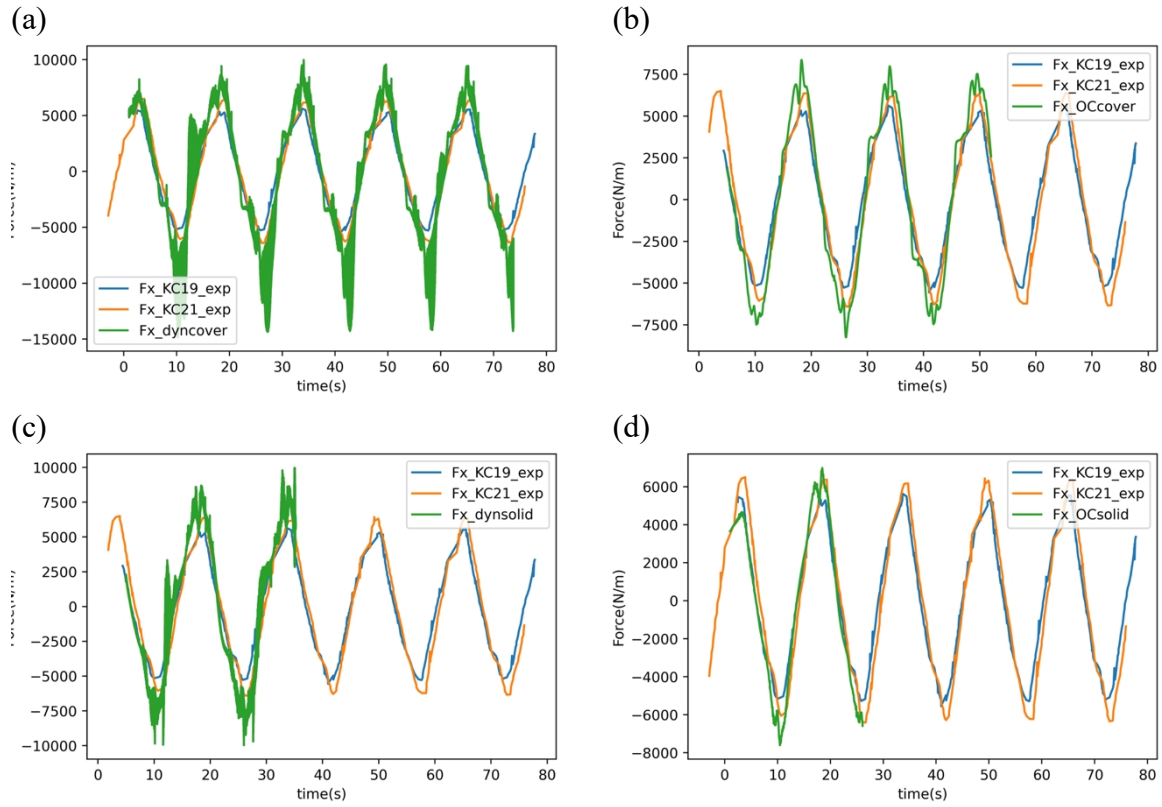

Figure 5.9 Fx comparison for KC=20

5.4 Comparison of F_z for KC=3,5,11,20 with the experimental data

The time histories of F_z under different KCs are shown in Figure 5.10 to Figure 5.13. It can be seen that there is evident difference between cover and solid cases. The maximum values of F_z for hollow cover cases are almost twice as much as those for solid structure cases. And as the KC becomes larger, the difference is more obvious. The reason why they have such a different behavior is due to the different geometries. F_z may be influenced by the communication between flow fields inside and outside the cover. The cover case with hollow cavity and small gap would produce a sudden acceleration of the flow in the gap and strong vorticity (which will be discussed in Section 5.5) in the cavity. And compared with the solid structure cases where there is weak flow interaction in the gap between the structures and the plate, the cover cases have more flow interaction that allow large vortices to fully develop inside the cover.

5.4.1 KC=3,5 and 11

The results of the cases for KC=3,5 and 11 have the consistent characteristics. It can be seen that the value of the solid structure cases is in general agreement with the experiments especially in the positive F_z part under KC=5 and 11, which implied the experiment assumption that the water inside cover is frozen and has almost none effect on vertical force. With the increasing KC number, the vertical forces are more and more asymmetry until KC=11, only having positive vertical force.

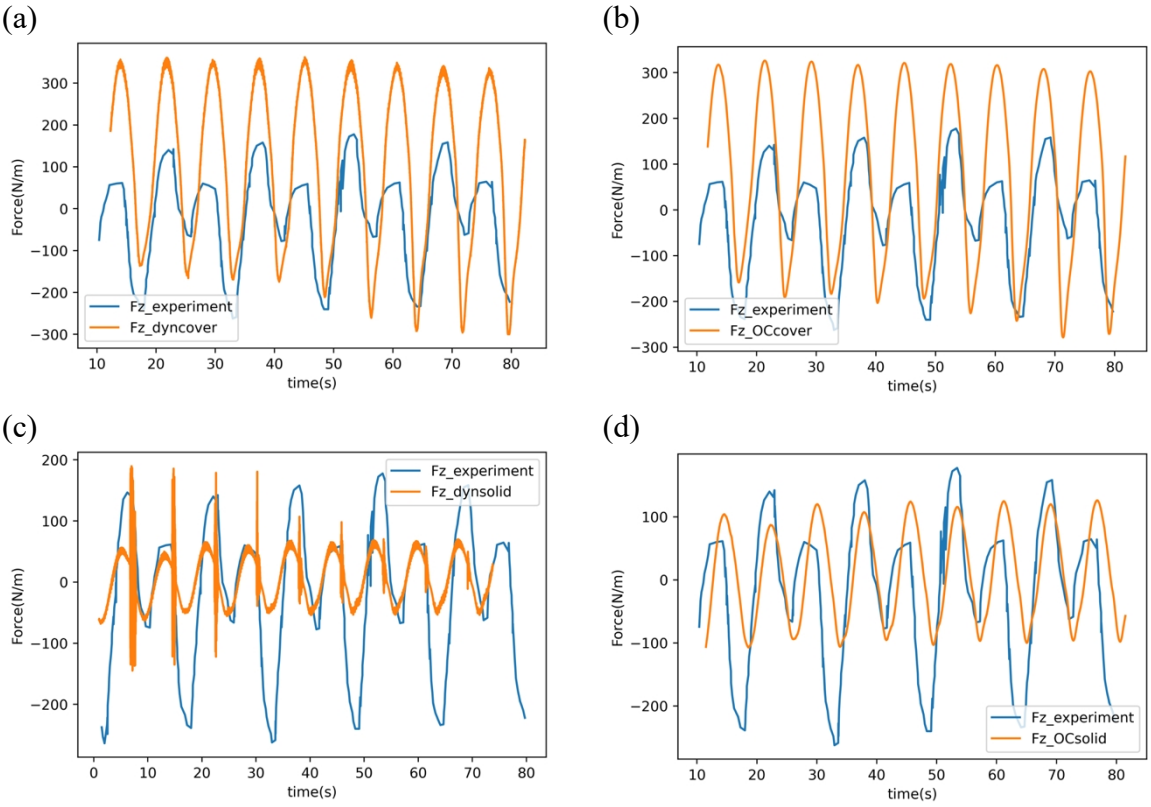

Figure 5.10 Fz comparison for KC=3

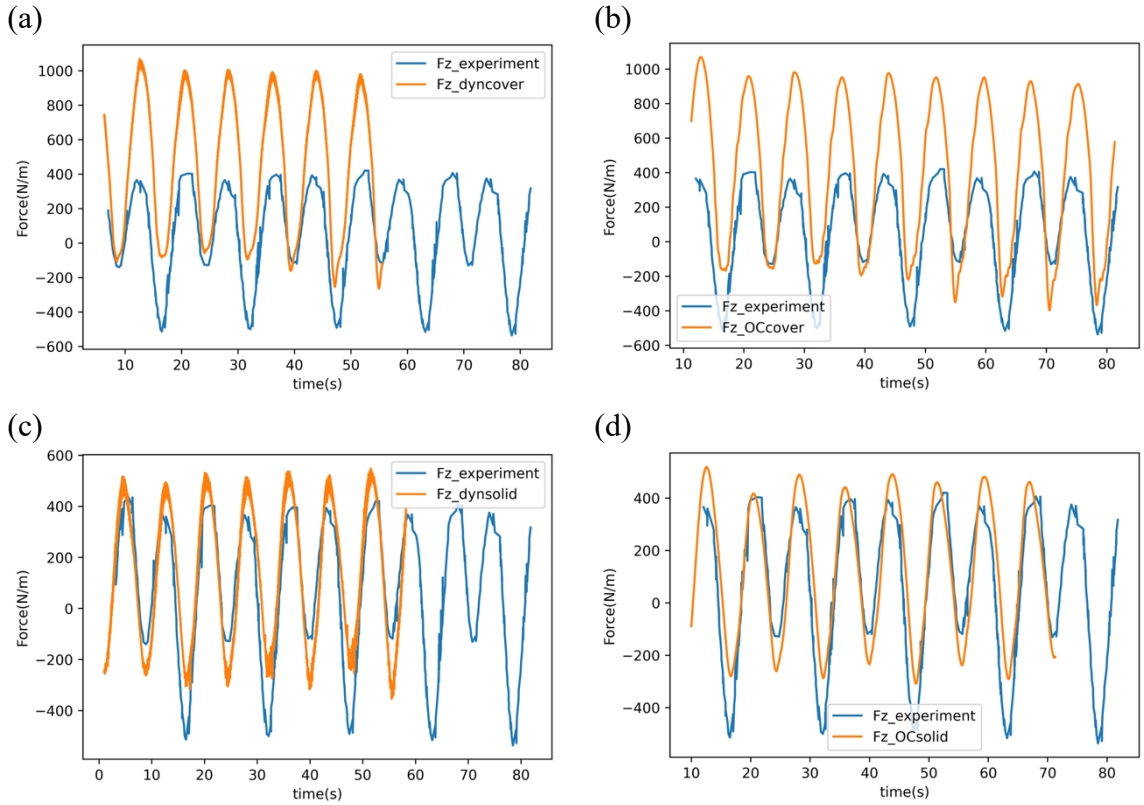

Figure 5.11 Fz comparison for KC=5

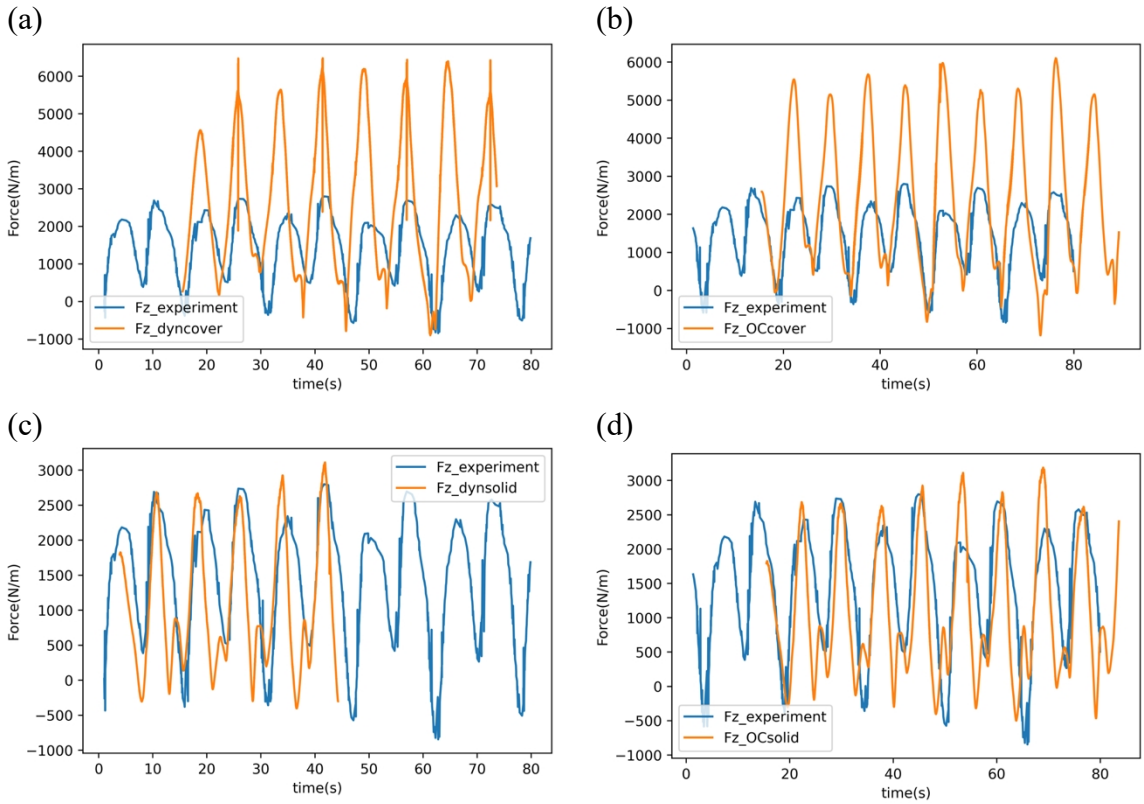

Figure 5.12 Fz comparison for KC=11

5.4.2 KC=20

For lager KC number of KC=20, on the contrary, the cover cases of both the flow around the oscillating cover and the oscillatory flow around static cover are comparable with experimental data, while the amplitude of F_z for the solid cases has almost vertical shift in the negative direction, which is quite different from the experimental data.

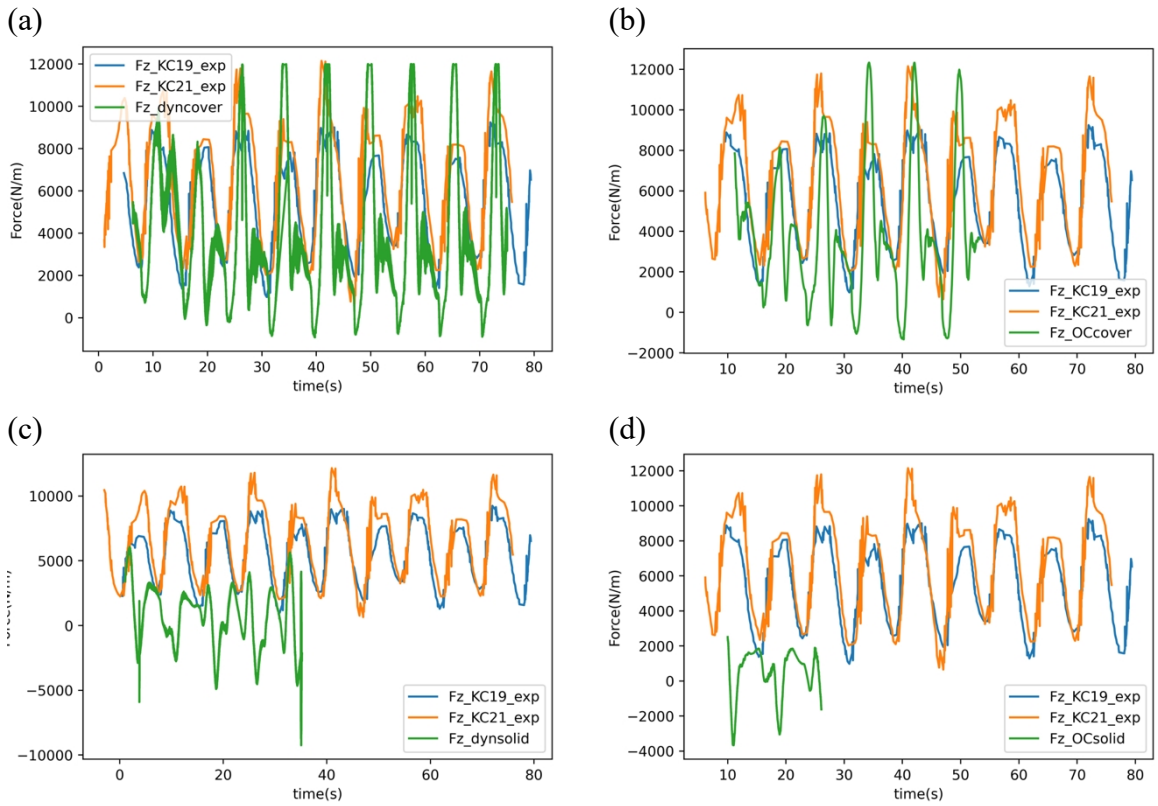

Figure 5.13 Fz comparison for KC=20

5.5 Contours of the spanwise vorticity and normalized pressure with streamlines for KC=3,5,11,20

Contours of the spanwise vorticity defined as $\omega_z = \partial v/\partial x - \partial u/\partial y$, the pressure and the streamlines are shown and discussed in this section covering all investigated cases. These flow fields are taken from 4-time instances within one period. The spanwise vorticity increases with the KC number increases. Compared with solid cases, the cover cases show the same flow field characteristics outside the cover, which confirms the conclusion that the horizontal forces of cover cases and solid cases are almost equal. And the vortices inside cover have the crucial influence on vertical forces, which can be found by comparing KC=20 cases with others: only the KC=20 case has one strong vorticity inside cover. With the increasing KC number, the

stronger vortices interaction inside cover, the bigger vertical forces difference between the cover cases and the solid cases.

5.5.1 KC=3 and 5

For the lower KC number of KC=3 and 5, they have the similar characteristic. The relative motions between the flow and the structure are small. Therefore, under KC=3, as seen from Figure 5.14 and Figure 5.16, the 4 vortices tended to be locally distributed around the 4 comers of the cover. There are also 2 vortices on the two ends of the plate for cover cases. The shedding of these vortices is weak. In addition, the vortices systems of the oscillating cover cases are also similar to those of the oscillatory flow cases. For the solid cases, there are only 3 vortices at the maximum location and at the meantime within the period: 2 on the top of cover and 1 on the end of plate. For cover cases, due to cavity and small displacement of flow, the vortices interact with inner wall and fully develop to 2 opposite vorticity phases. This is might cause that the vertical forces are much higher the experiment results which seen the water inside as frozen water.

(a) t=$\frac{1}{4}$T

(b) t=$\frac{1}{2}$T

(c) t=$\frac{3}{4}$T

(d) t=T

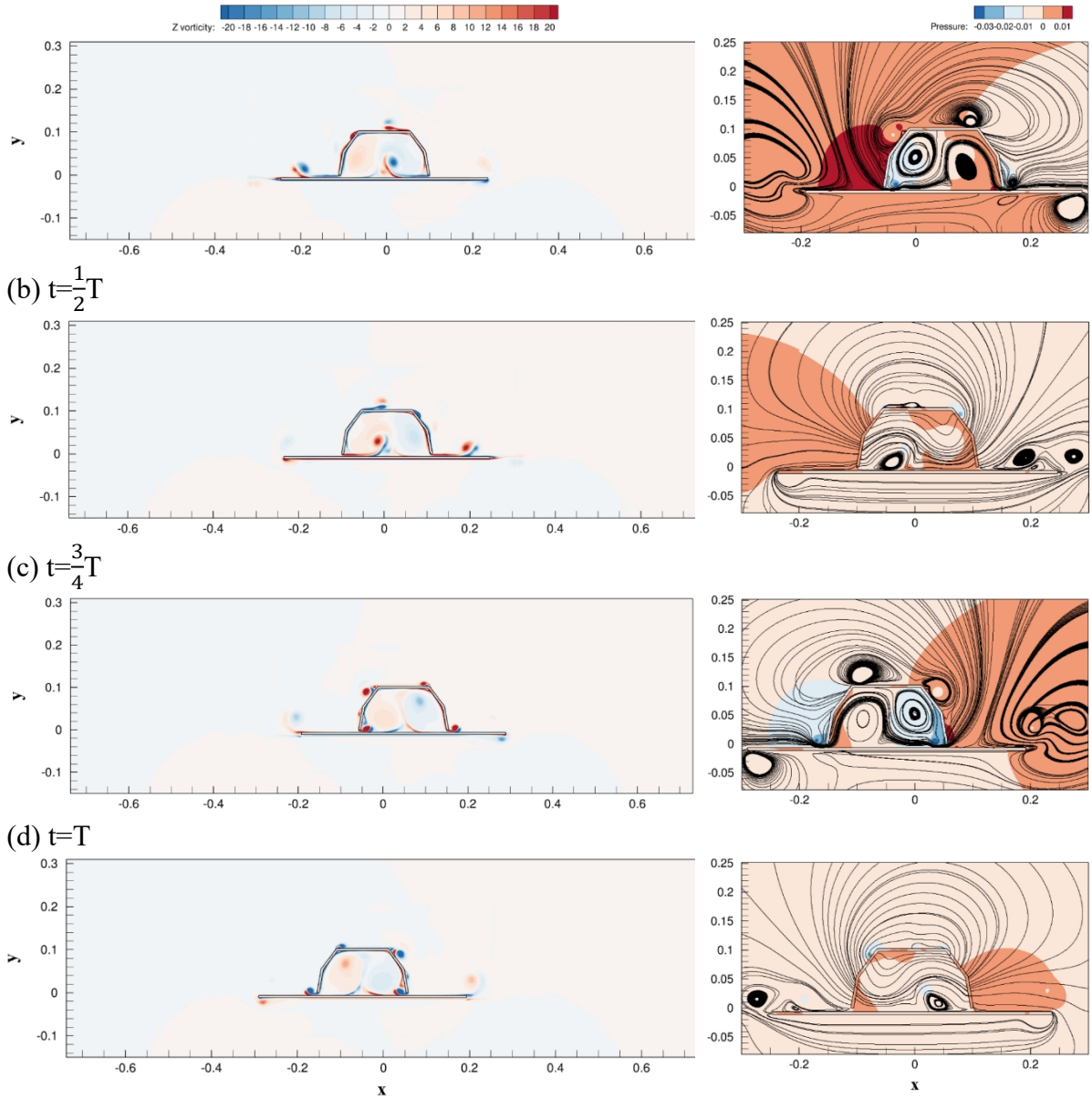

Figure 5.14 Contours of the spanwise vorticity and normalized pressure with streamlines of dyncover for KC=3

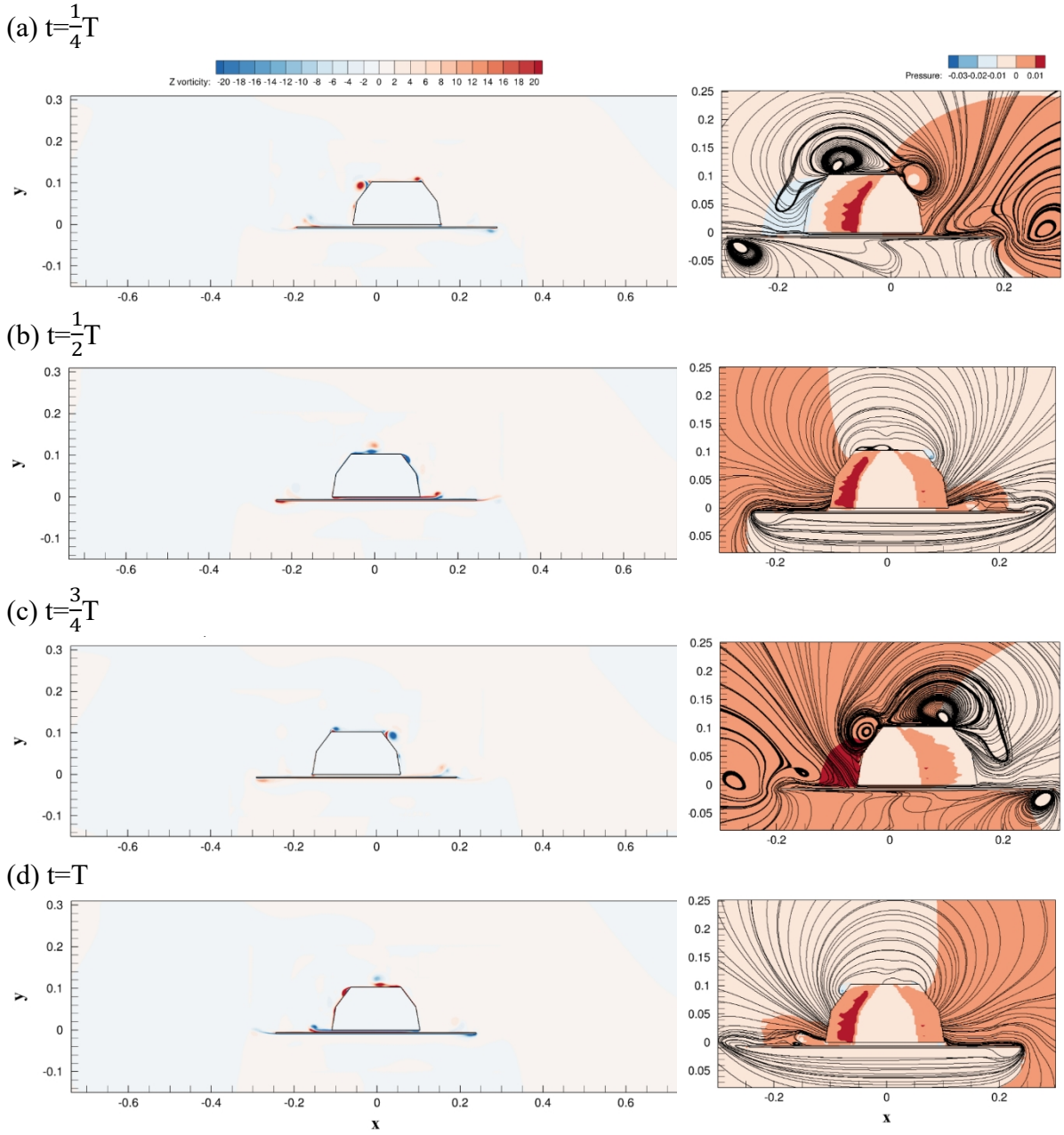

Figure 5.15 Contours of the spanwise vorticity and normalized pressure with streamlines of dynsolid for KC=3

(a) t=$\frac{1}{4}$T

(b) t=$\frac{1}{2}$T

(c) t=$\frac{3}{4}$T

(d) t=T

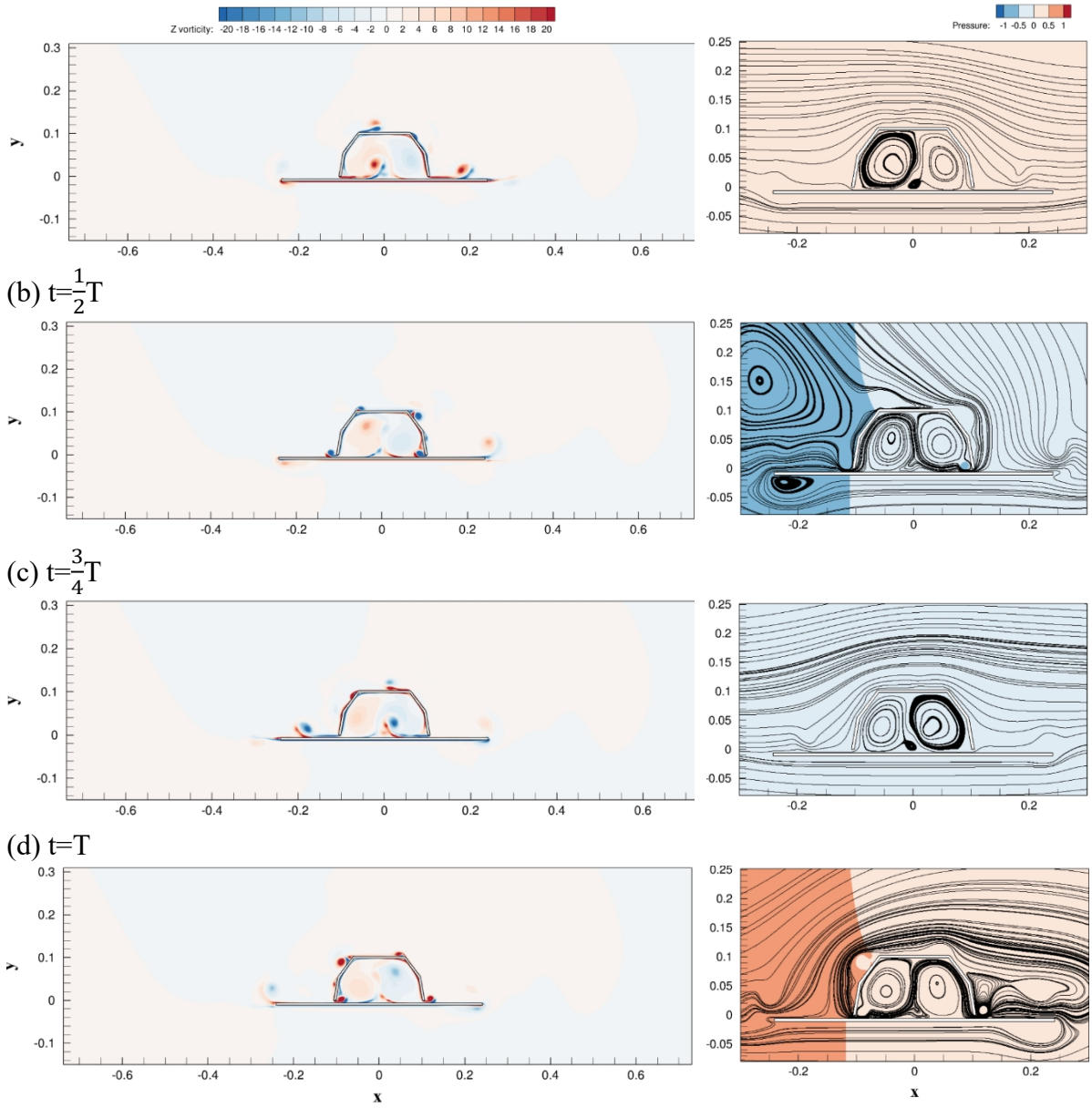

Figure 5.16 Contours of the spanwise vorticity and normalized pressure with streamlines of OCcover for KC=3

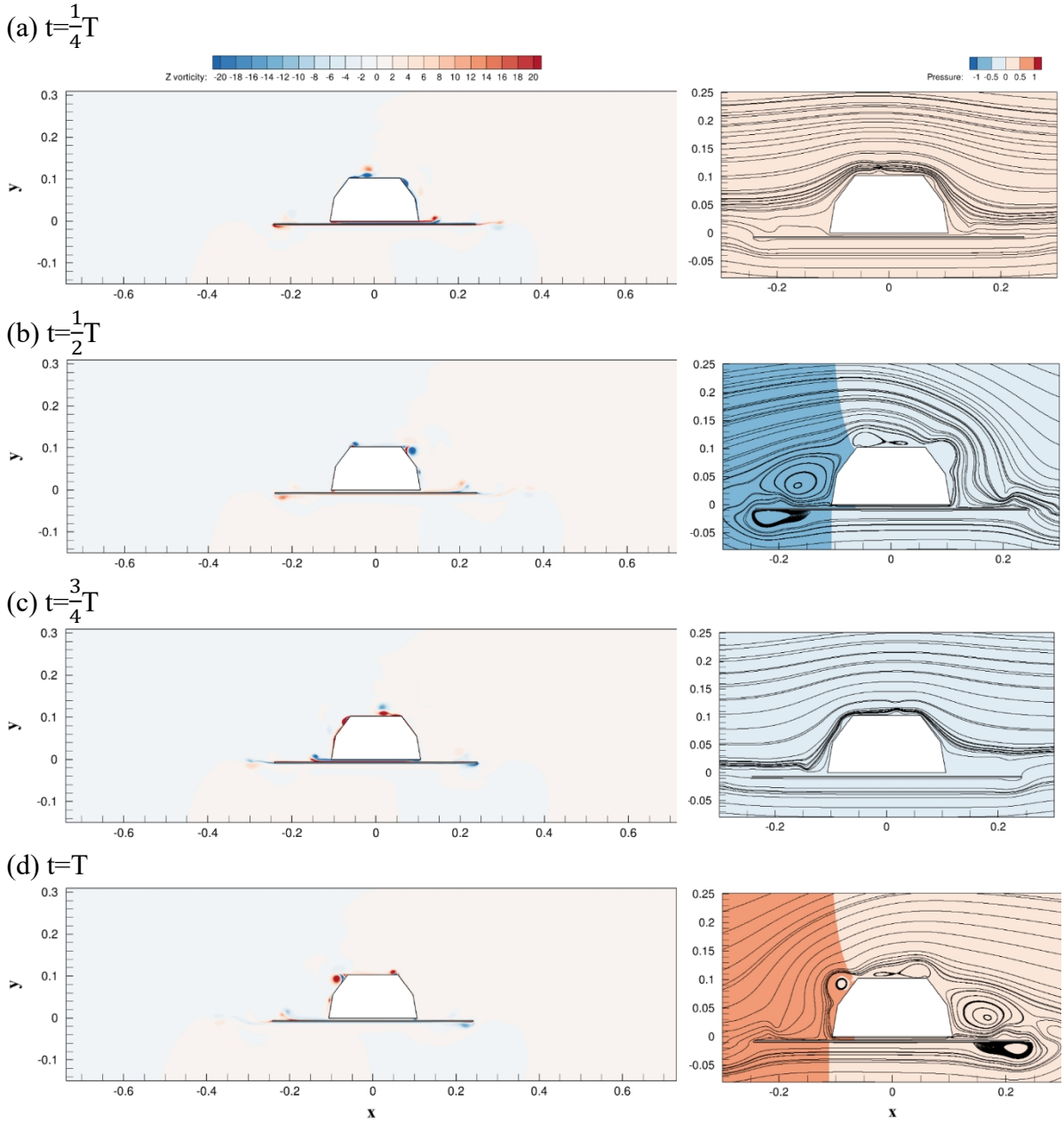

Figure 5.17 Contours of the spanwise vorticity and normalized pressure with streamlines of OCsolid for KC=3

(a) t=$\frac{1}{4}$T

(b) t=$\frac{1}{2}$T

(c) t=$\frac{3}{4}$T

(d) t=T

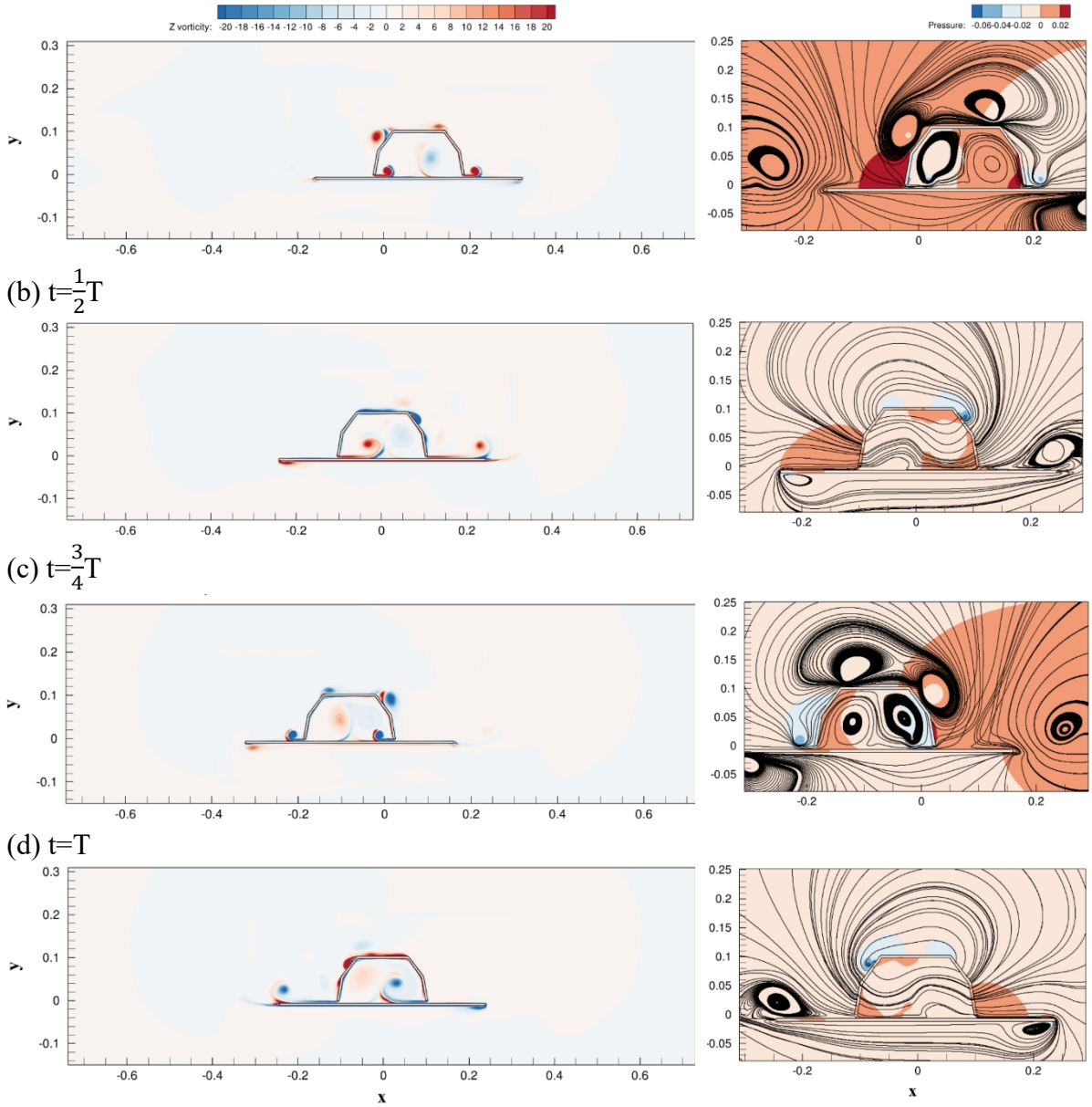

Figure 5.18 Contours of the spanwise vorticity and normalized pressure with streamlines of dyncover for KC=5

(a) t=$\frac{1}{4}$T

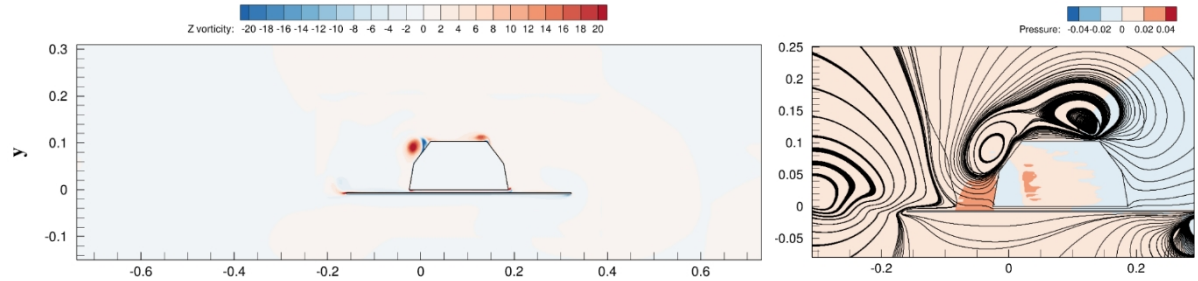

(b) t=$\frac{1}{2}$T

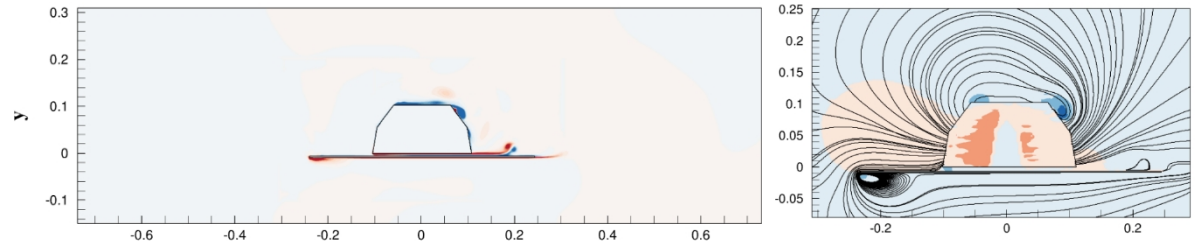

(c) t=$\frac{3}{4}$T

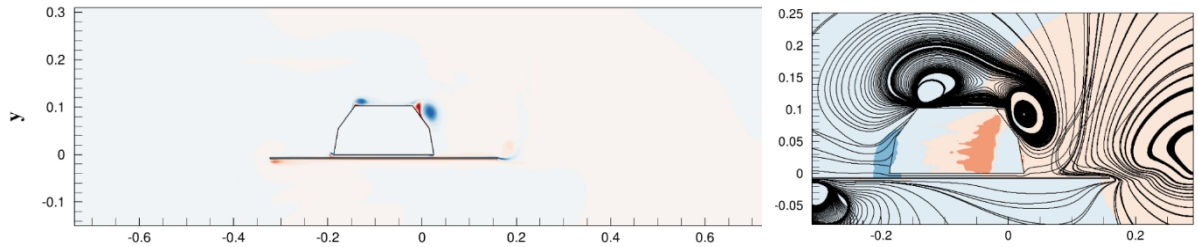

(d) t=T

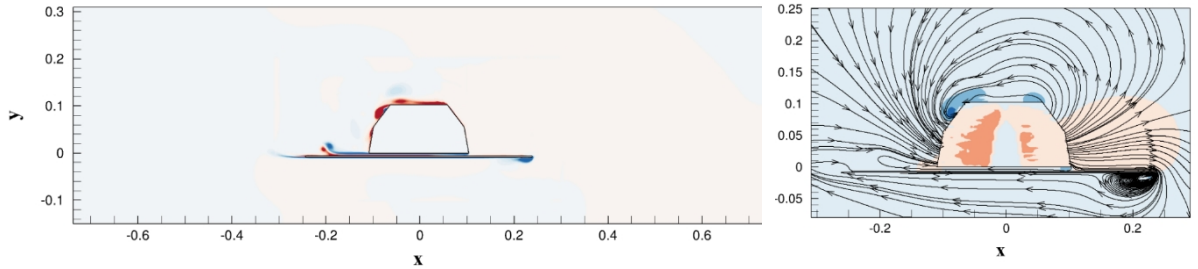

Figure 5.19 Contours of the spanwise vorticity and normalized pressure with streamlines of dynsolid for KC=5

(a) t=$\frac{1}{4}$T

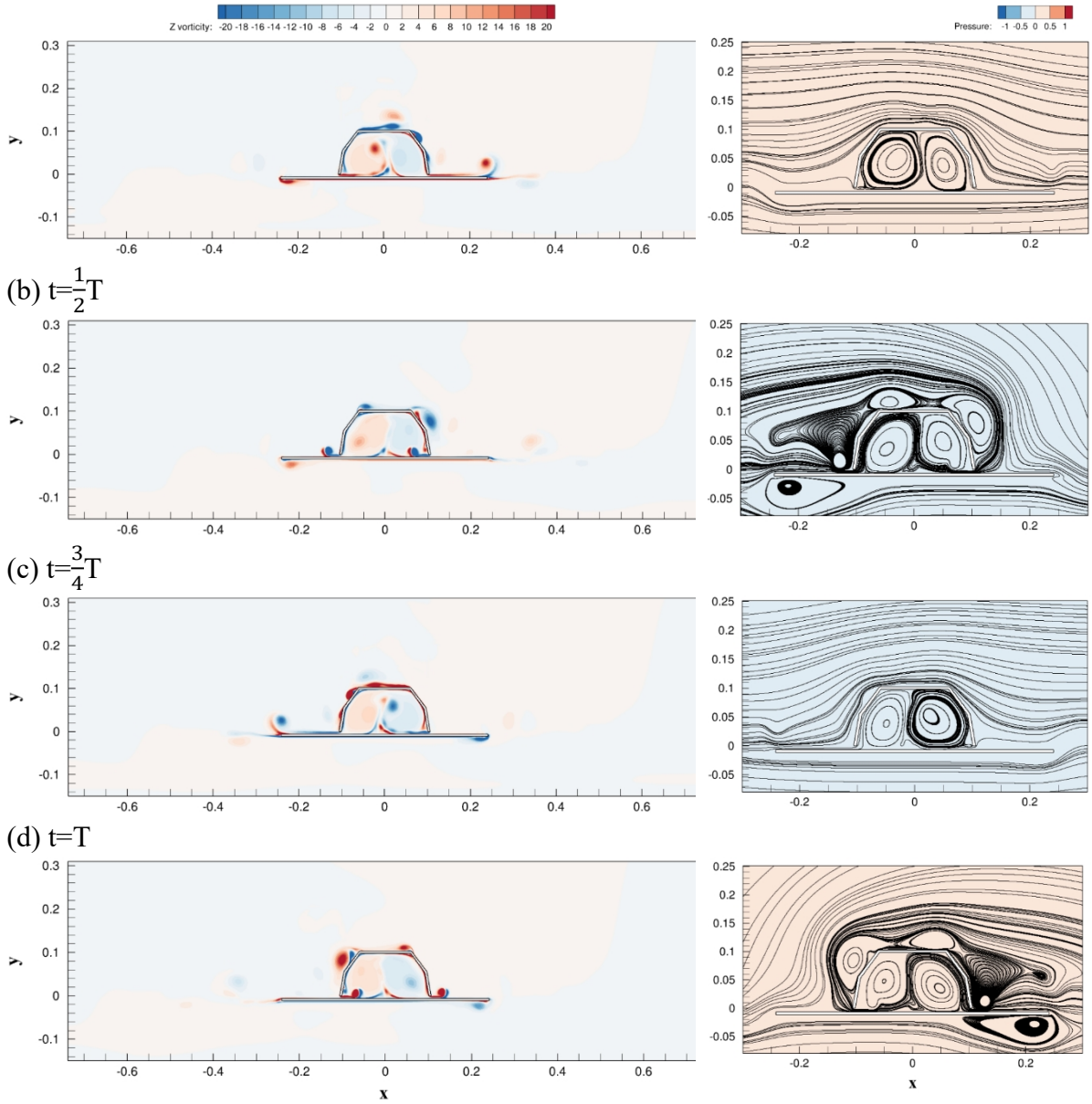

(b) t=$\frac{1}{2}$T

(c) t=$\frac{3}{4}$T

(d) t=T

Figure 5.20 Contours of the spanwise vorticity and normalized pressure with streamlines of OCcover for KC=5

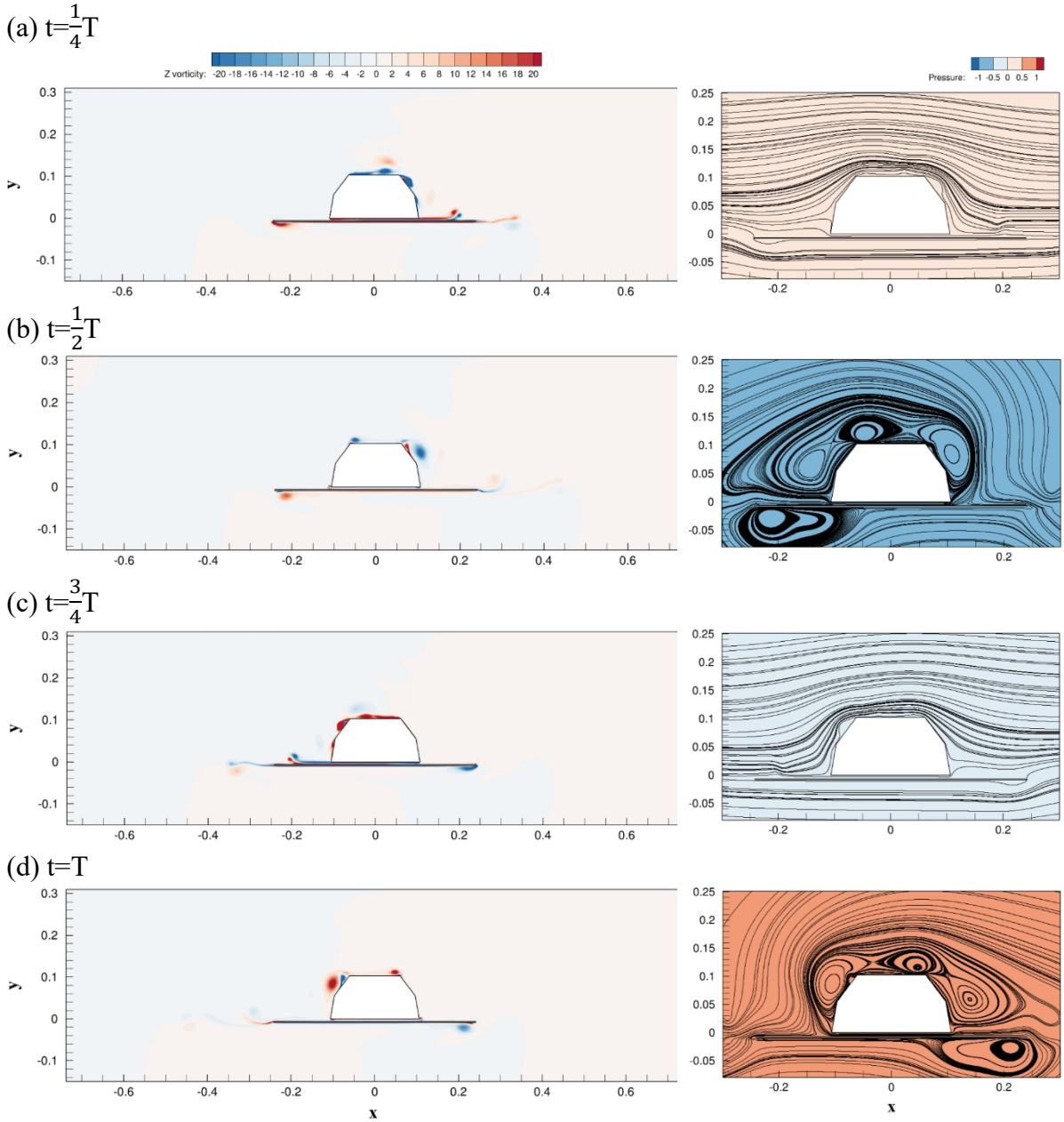

Figure 5.21 Contours of the spanwise vorticity and normalized pressure with streamlines of OCsolid for KC=5

5.5.2 KC=11

For the medium KC number of KC=11, the strength of the vortices is becoming large as seen from Figure 5.22 to Figure 5.25. The vortices at the top corner can cover the whole top edge and can be shed. The size of the shed vortices can be up to H. Furthermore, there are 3 vortices around the cover at two half period instances. As to inner vortices, the characteristics of KC=11 are similar to the cases for KC=3 and 5 so that the results of vertical forces have the same rules even though one vorticity is domain and another is passive generate.

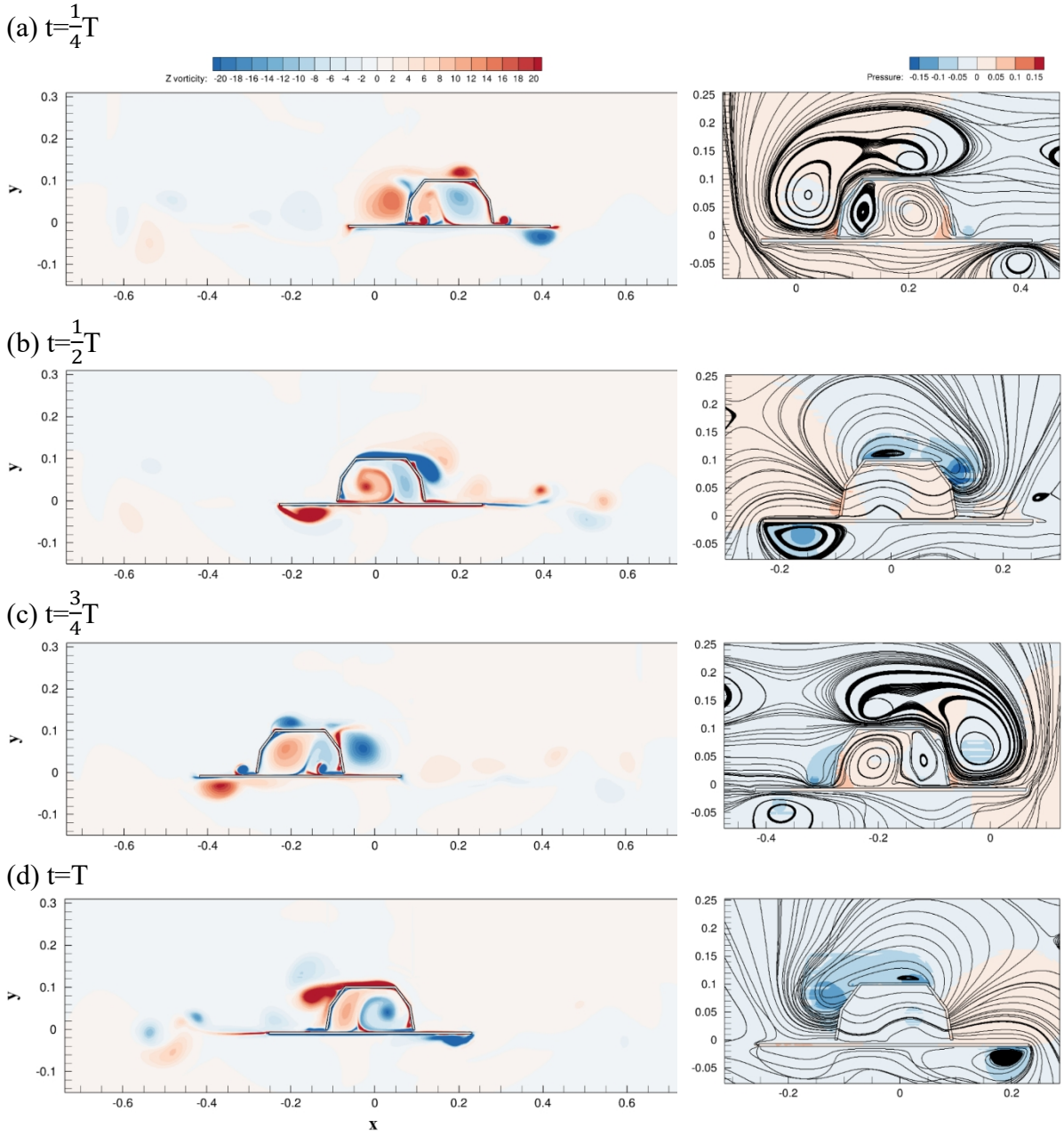

Figure 5.22 Contours of the spanwise vorticity and normalized pressure with streamlines of dyncover for KC=11

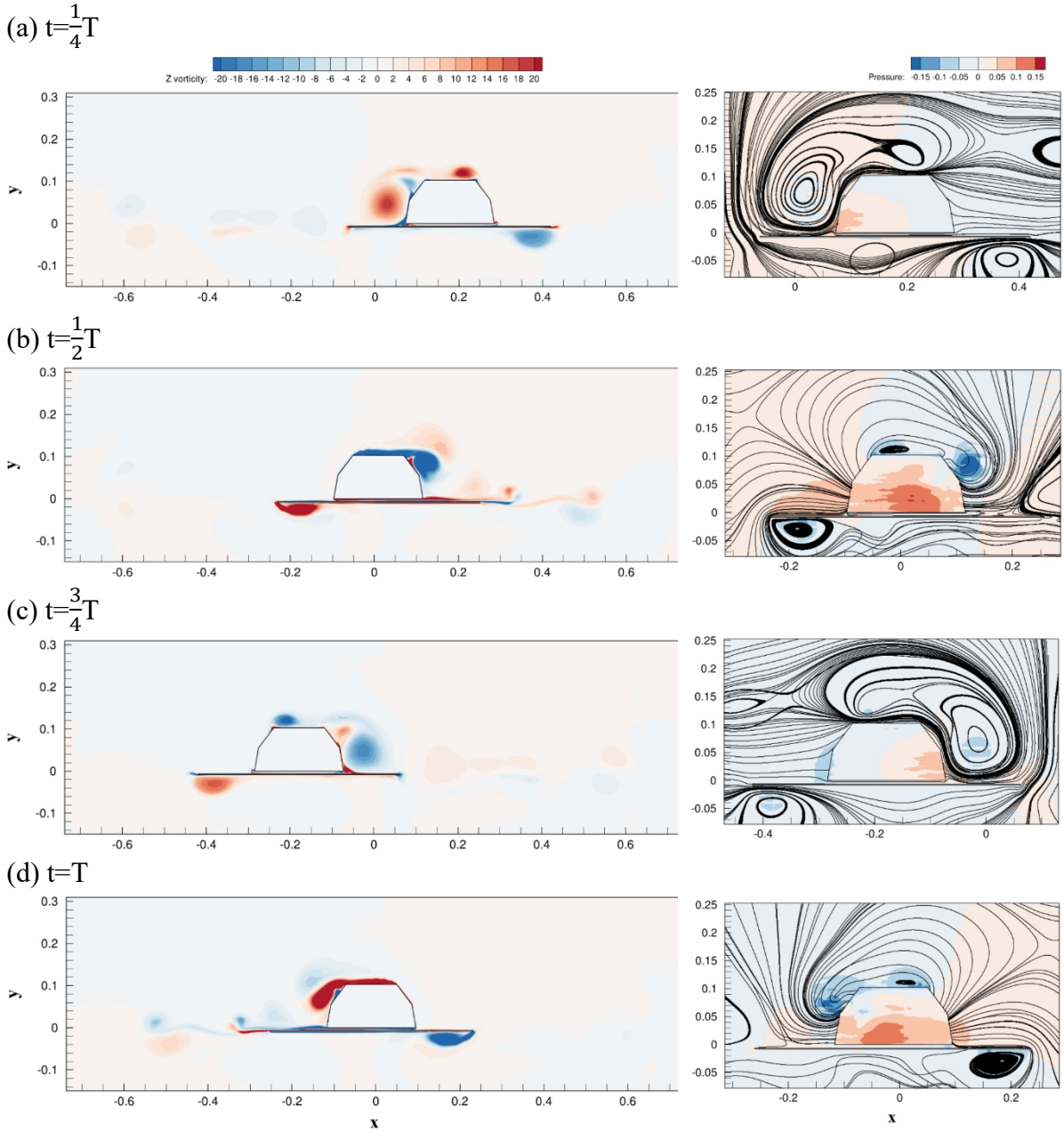

Figure 5.23 Contours of the spanwise vorticity and normalized pressure with streamlines of dysolid for KC=11

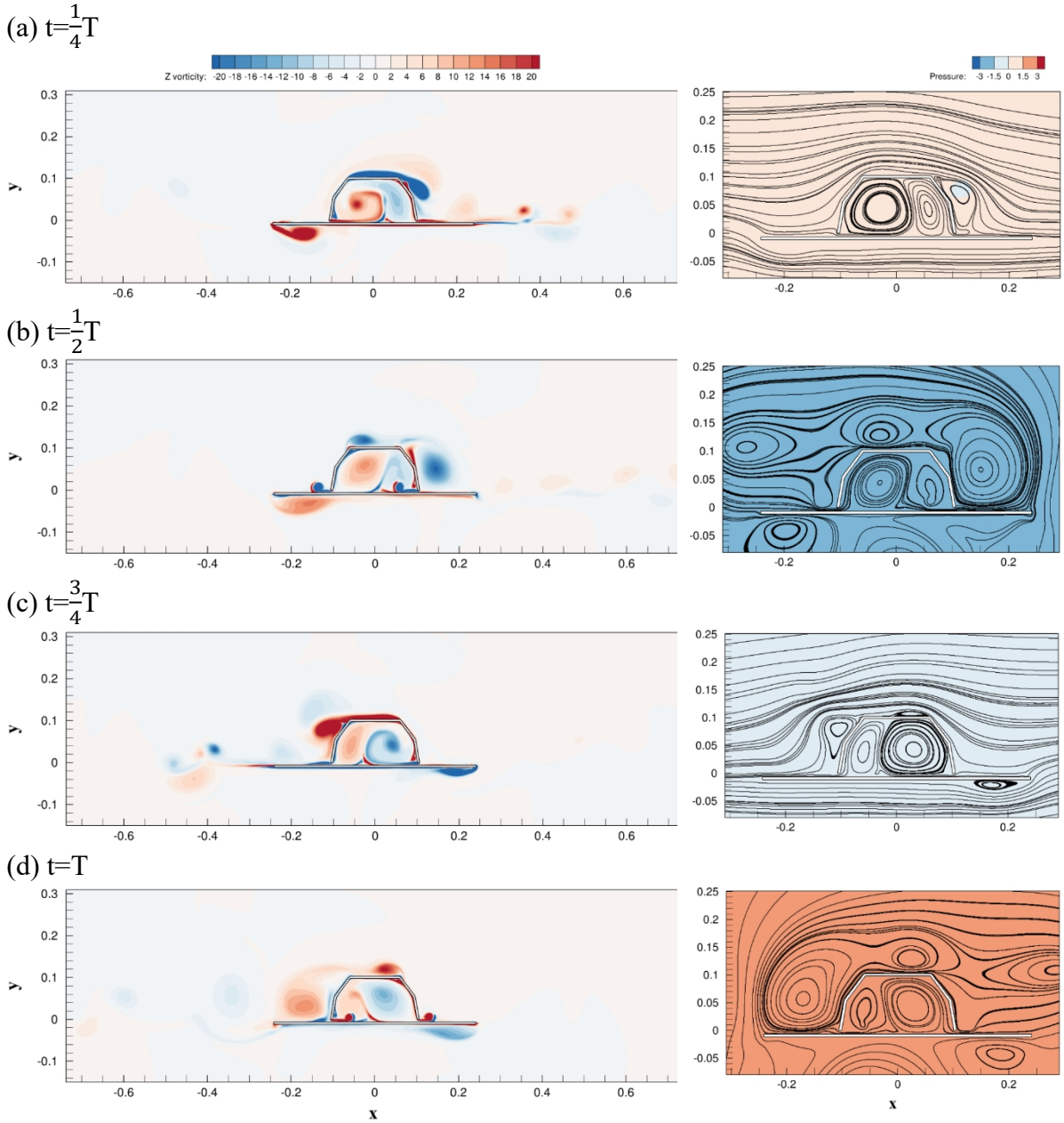

Figure 5.24 Contours of the spanwise vorticity and normalized pressure with streamlines of OCcover for KC=11

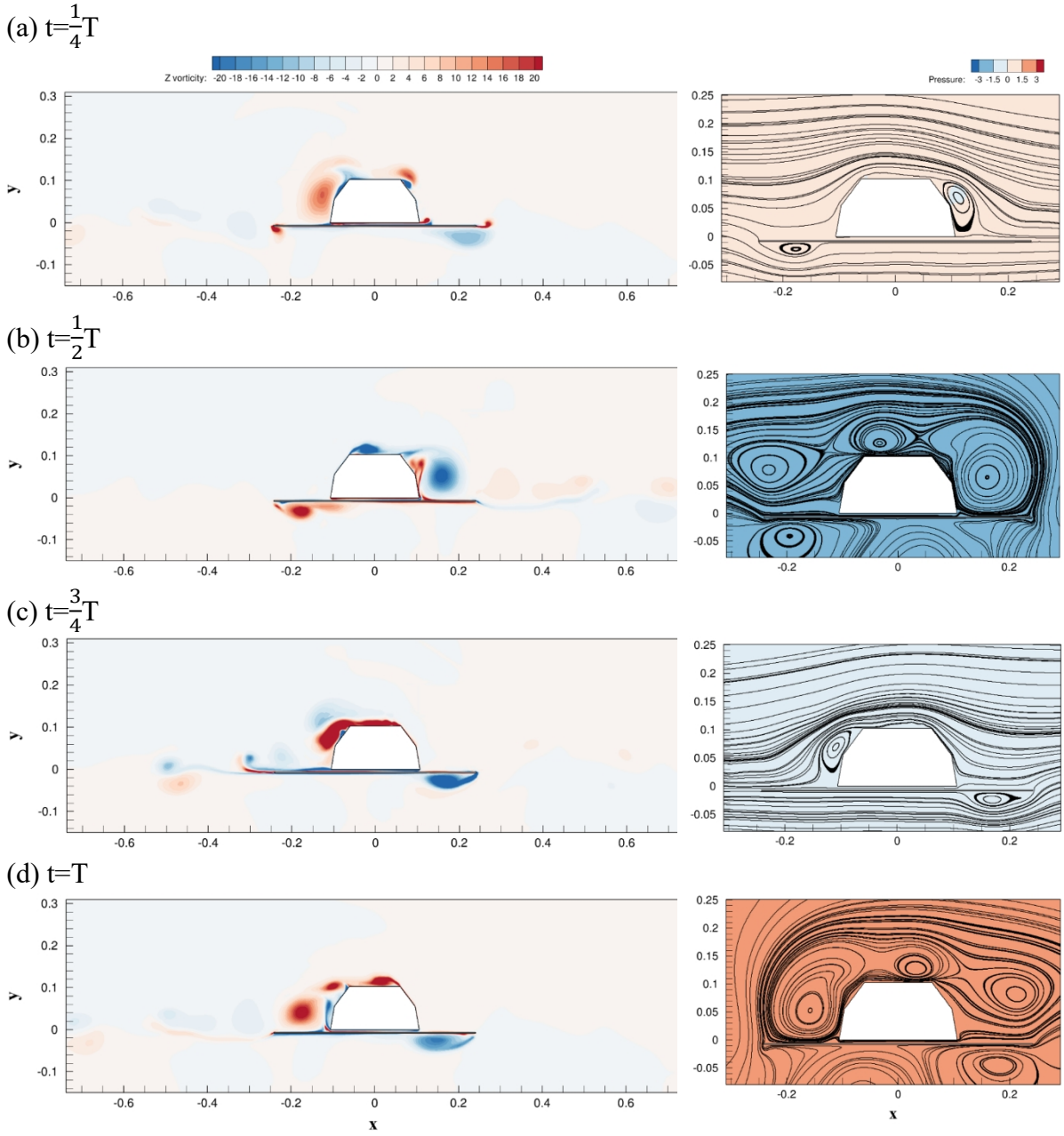

Figure 5.25 Contours of the spanwise vorticity and normalized pressure with streamlines of OCsolid for KC=11

5.5.3 KC=20

For the large KC number of KC=20, the strength of the vortices is becoming even large and the interactions between these vortices are also strong as seen from Figure 5.26 to Figure 5.29. In addition, the shedding vortices at the top corner can be divided by the shear layer from the other corner. For the hollow subsea cover cases, there are multiple vortices inside the cover. Apart from the large vortices formed due to the flow from the down corner, there are also small

vortices induced by the large one. There is strong vorticity produced between solid and plate. It might the reason why vertical forces for KC=20 solid cases are different.

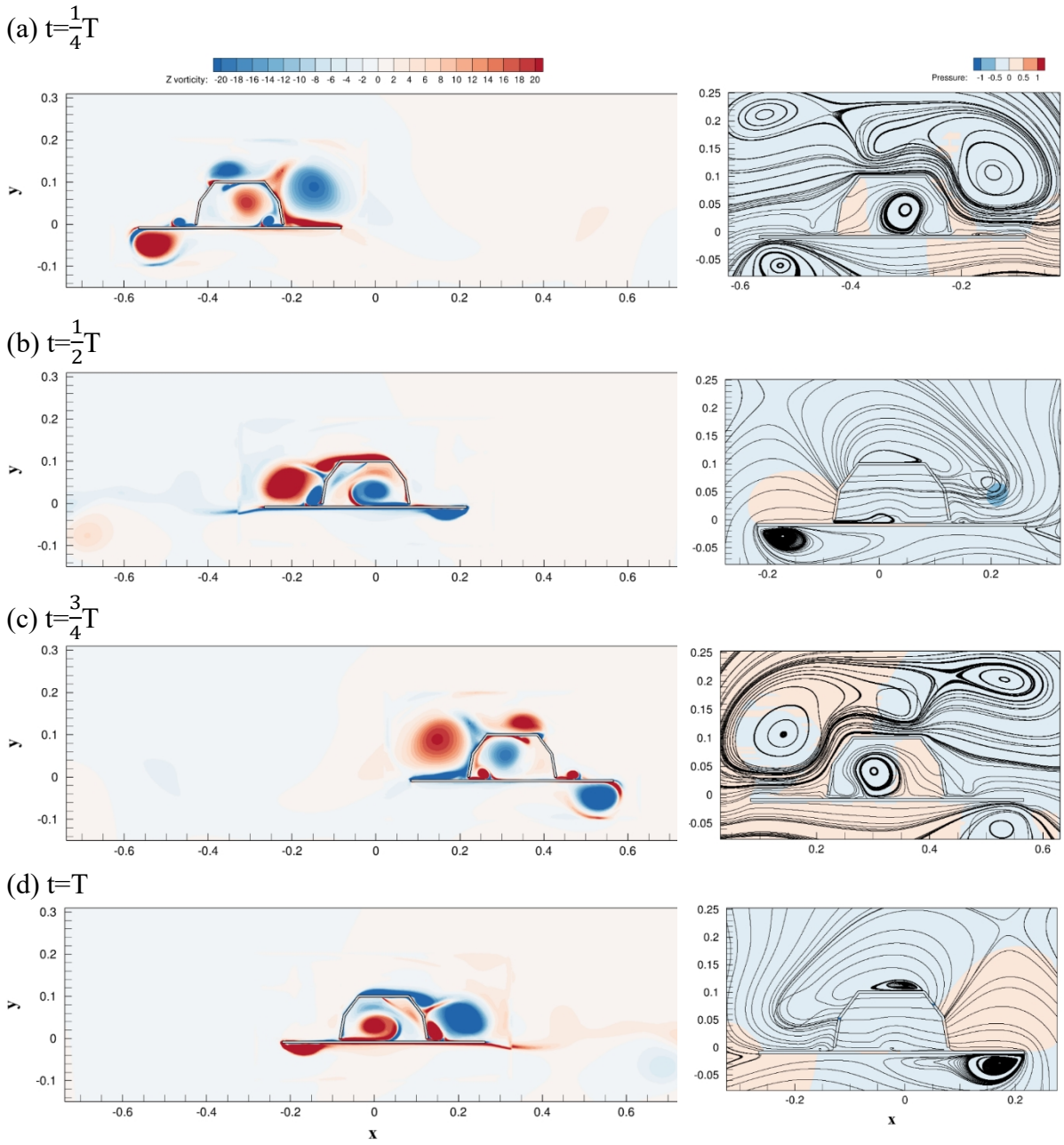

Figure 5.26 Contours of the spanwise vorticity and normalized pressure with streamlines of dyncover for KC=20

(a) t=$\frac{1}{4}$T

(b) t=$\frac{1}{2}$T

(c) t=$\frac{3}{4}$T

(d) t=T

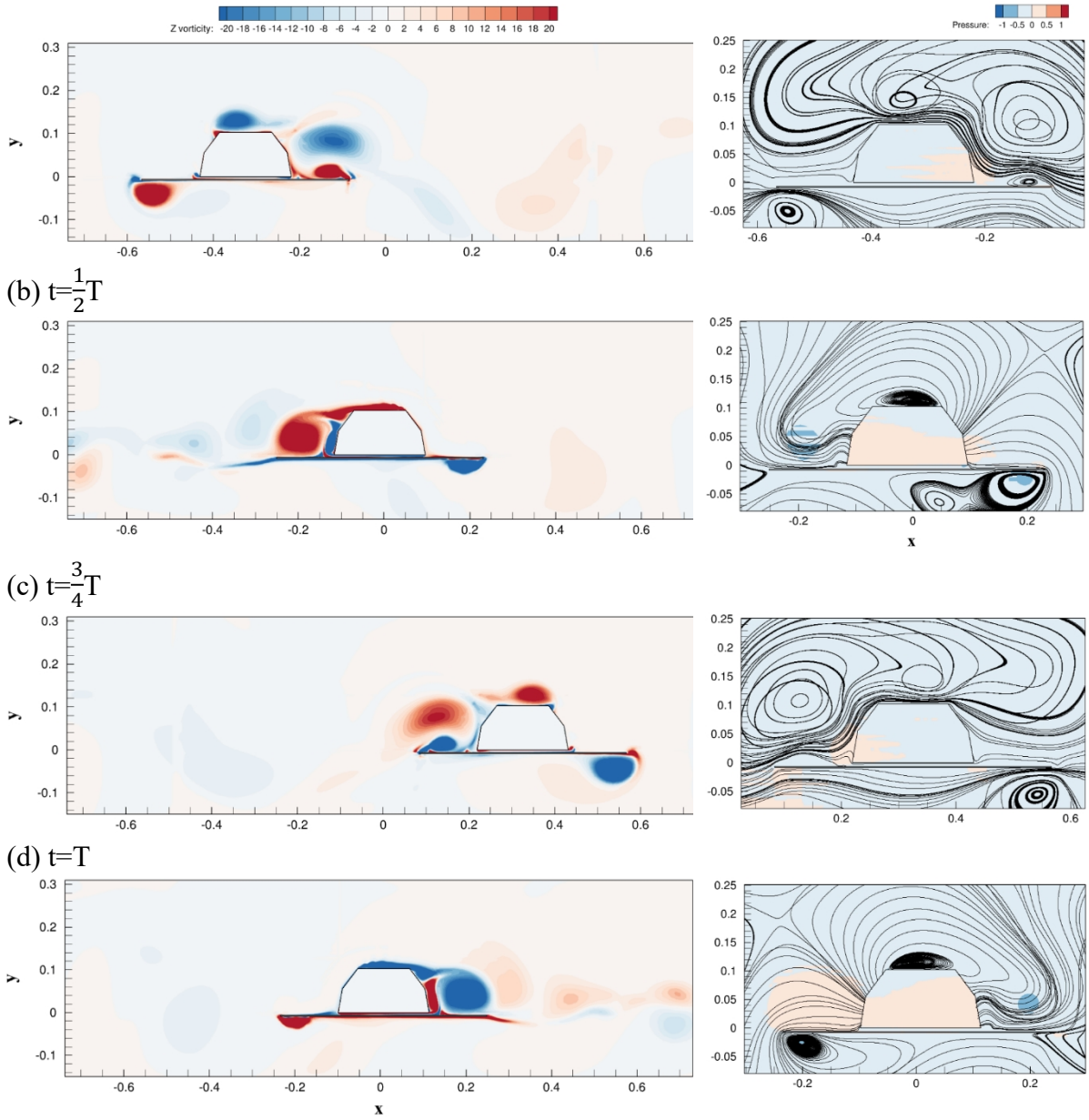

Figure 5.27 Contours of the spanwise vorticity and normalized pressure with streamlines of dynsolid for KC=20

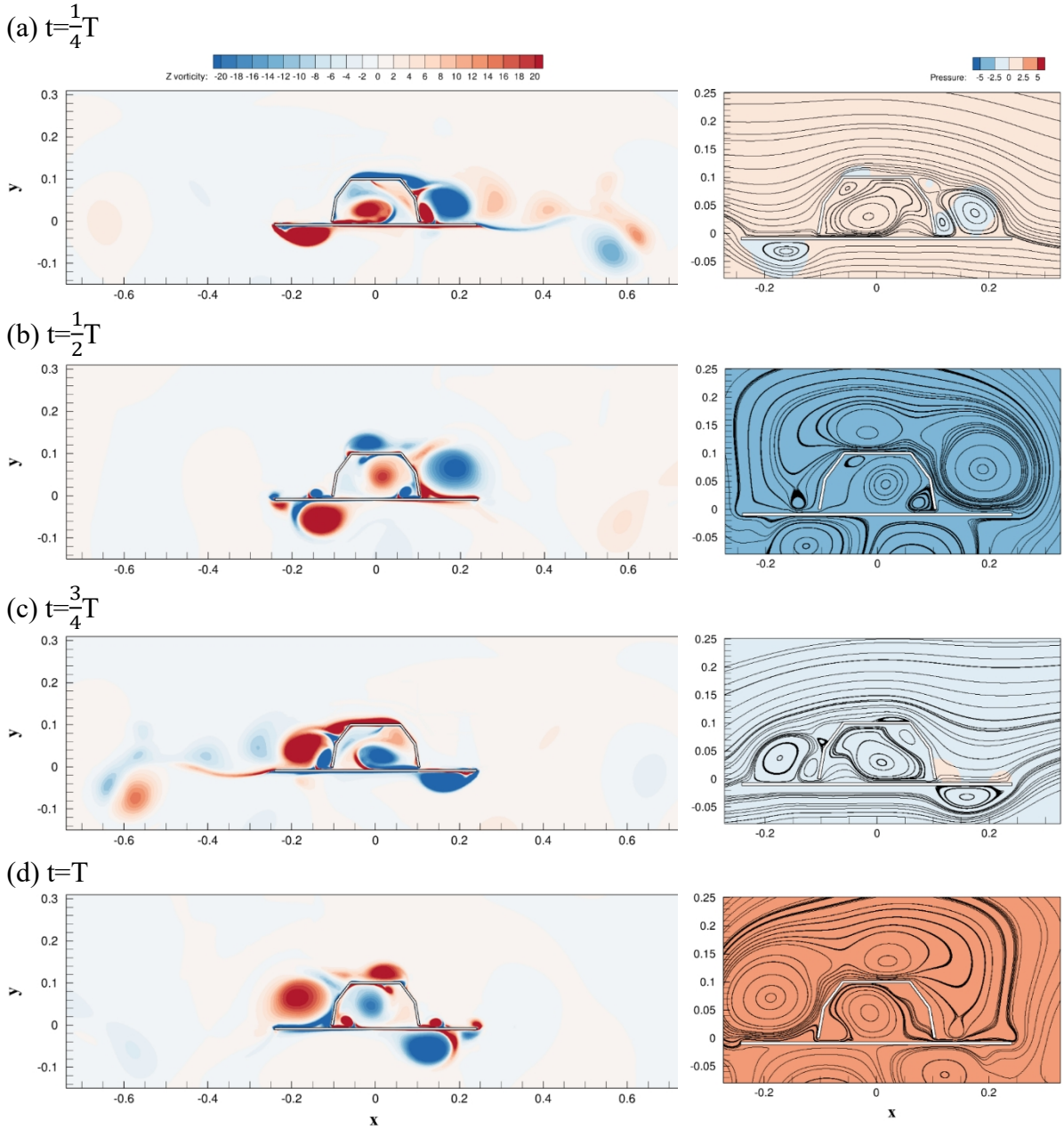

Figure 5.28 Contours of the spanwise vorticity and normalized pressure with streamlines of OCcover for KC=20

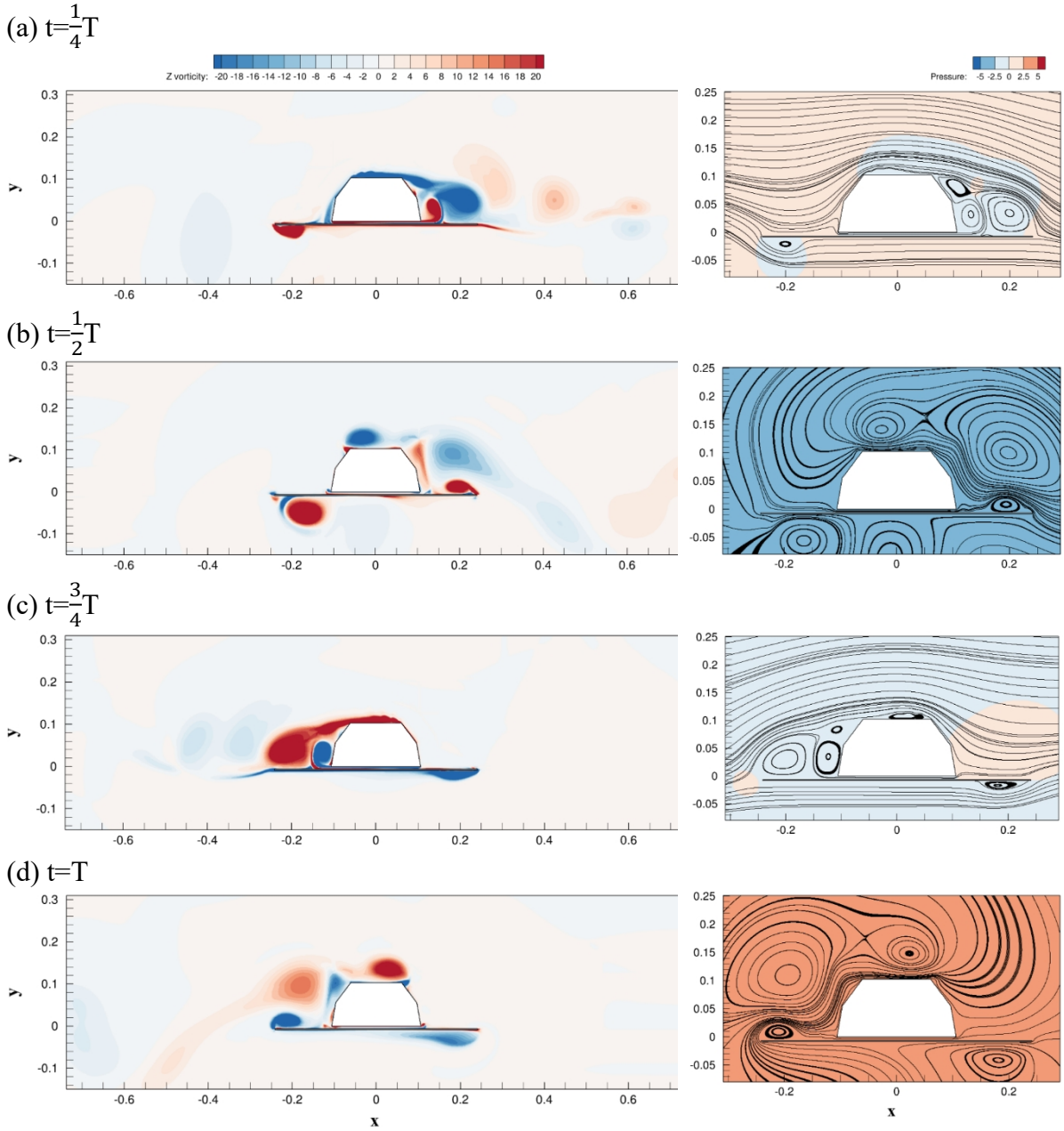

Figure 5.29 Contours of the spanwise vorticity and normalized pressure with streamlines of OCsolid for KC=20

5.6 Summary

In the present study, the flows around oscillatory subsea cover or the oscillatory flow around static subsea cover are analyzed at KC=3,5,11 and 20, which categized to low-, medium- and large-KC number region. Main conclusions are outlined as follow:

1. By oscillating a subsea cover under the 3 categized KC number region, the values of both the vertical force and the horizontal force are almost the same with those on a static subsea cover subjected to an oscillatory flow.
2. For low- KC region (KC=3 and 5), the time histories of F_x are similar to the experimental data for both the hollow subsea cover and solid structure cases. The maximum value of the present predicted F_x for the subsea cover is slightly larger than that of the experimental data which may be due to the influence of the strong flow into the hollow cover.
3. The value of the solid structure cases is in general agreement with the experiments especially in the positive F_z part under KC=5 and 11.
4. For medium-KC region (KC=11), the results of hollow cover cases and oscillatory flow around a solid structure case agree with the experimental data. However, only for the oscillating solid structure case there is obvious maximum amplitude difference compared with the experimental data.
5. For large-KC region (KC=20), the overall present predicted F_x values of all cases match well with the experimental data. As to vertical forces F_z, only the cover cases are comparable with experiment data, but the solid cases have large difference: The amplitude of F_z for the solid cases has almost vertical shift in the negative direction.
6. The spanwise vorticity increases with the KC number increases. The vorticity structure inside cover has the determined effect on vertical force. In general, increasing the communication level between the inside and outside the cover strongly affects the vertical forces. This is clearer for large KC numbers. With the increasing KC number, the stronger vortices interaction inside cover, the bigger vertical forces difference between the cover cases and the solid cases.

6 Results of further development of new structure cover model

6.1 Overview of this chapter

In this chapter, the numerical model is further revised to make it closer to the real situation compared with that in the previous chapter. There are mainly two considerations in this revision. First in order to further improve the numerical simulation results, compared to the experimental data. In this chapter, the different geometry subsea covers under different flow condition will be compared and analyzed in order to arrive at the most applicable model for the numerical simulations.

6.2 Different position and structure of cover

6.2.1 Case 1: cover only shell connected with domain

As can be seen from the results in the previous chapter, the results for the cover and solid case differ significantly, it can be inferred that the interaction of the water inside the cover and outside water through the gap beneath the subsea cover is key to influencing the value of F_z. To completely exclude the effect of water movement under the cover on the cover and explore their effects on the lift forces, the Case 1 model is designed as described below.

The size of the fluid domain needs to ensure that the inlet flow velocity is fully developed and the far field conditions need to be treated as infinite, therefore in this chapter the fluid domain size is expanded to 80H*20H, which is sufficiently large for the required requirements (Placzek et al. 2009).

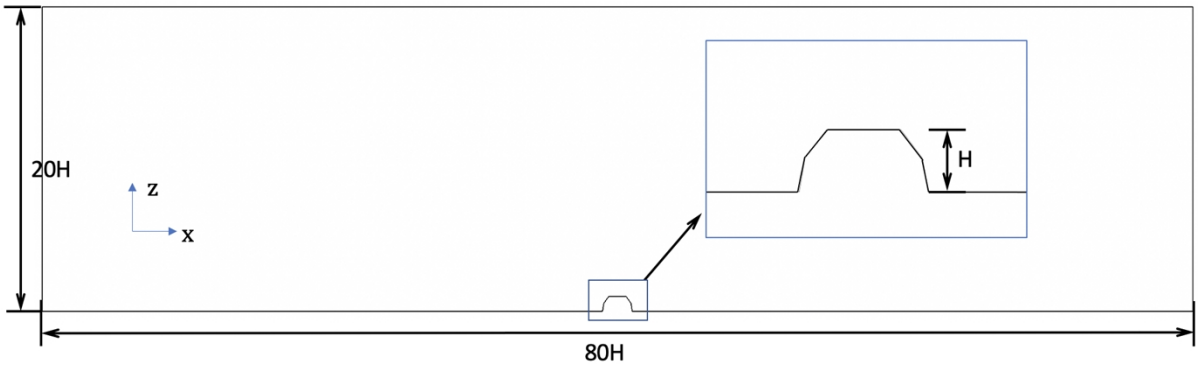

Figure 6.1 the computational domain and the subsea cover simulation model of case 1

It worth mentioning that when using OpenFOAM to perform numerical simulation of a structure subjected to an oscillatory flow, the obtained pressure $p = \tilde{p} + \overline{p}$ is fictitious pressure,

that equals to the sum of the true pressure $\tilde{p}$ and the inertial component $\bar{p}$. The inertial component $\bar{p}$ is generated due to the oscillatory flow which satisfies

$$\frac{\partial U}{\partial t} = -\frac{1}{\rho}\frac{\partial \bar{p}}{\partial x} \tag{6.1}$$

In OpenFOAM, usually a fixed value boundary condition for p is applied at the outlet as $p = 0$ at $x = L_x$ as seen in Figure 6.2, which is used to provide a reference value to obtain the pressure value in the domain.

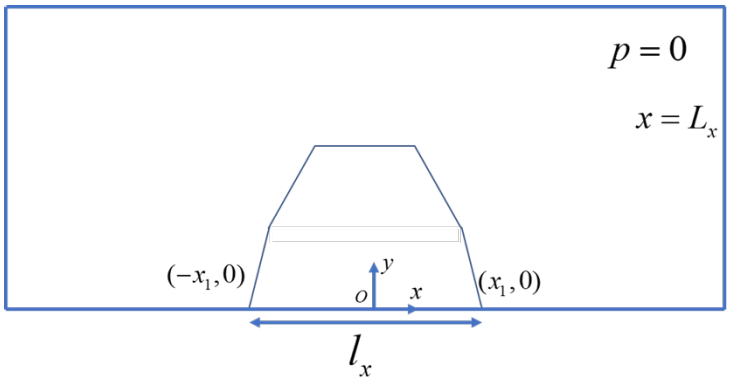

Figure 6.2 Sketch of the calculation domain

Therefore, when under the oscillatory flow condition of $U = U_m sin(\omega t)$, the inertial component $\bar{p}$ in the flow field is given as

$$\bar{p}(x,z) = 0(\text{ref value at } x = L_x) + \int_{L_x}^{x} \frac{\partial \bar{p}}{\partial x'} dx' = -\rho U_m \omega cos(\omega t)(x - L_x) \tag{6.2}$$

where L_x is the domain size and l_x is the bottom length of the structure. Then the inertial pressure induced $\boldsymbol{F}_{FK}$ force acting on the structure is given as

$$\boldsymbol{F}_{FK} = \int_S (-\bar{p})\boldsymbol{n}\, ds \tag{6.3}$$

For a subsea cover that is placed on an infinitely large domain as seen in Figure 4.6, the integral in $_{\text{FFK}=}\int_S (-\bar{p})\boldsymbol{n}\, ds$ (6.3) can be conducted along a closed surface and Gaussian Theorem can be used to transform a surface integral to volume integral (with a volume of V_p) as

$$\boldsymbol{F}_{FK} = \oint_S (-\bar{p})\boldsymbol{n} ds = -\int_{Vp} \nabla \bar{p} dV = \rho U_m \omega cos(\omega t) \int_{Vp} \nabla(x - L_x) dV = \rho U_m \omega cos(\omega t) V_p \boldsymbol{i} \tag{6.4}$$

Then there is no vertical component in this FK force.

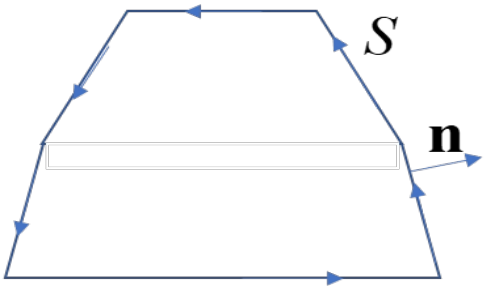

Figure 6.3 Integral path along the subsea cover

However, when the structure is placed on the bottom boundary with no gap between as seen in Figure 6.4, the integral cannot be conducted along a closed surface and there is vertical component in the FK force.

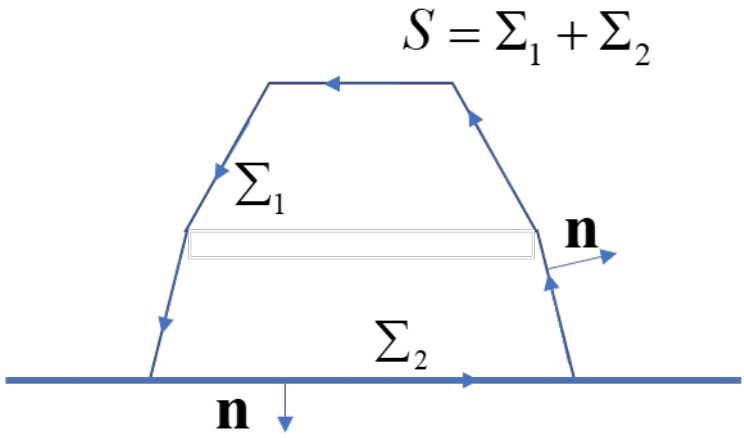

Figure 6.4 Disaggregation of the integral route along the subsea cover

The integral

$$_{\text{FFK}=}\oint_S(-\bar{p})\boldsymbol{n}ds = -\int_{Vp}\nabla\bar{p}dV = \rho U_m\omega cos(\omega t)\int_{Vp}\nabla(x-L_x)dV = \rho U_m\omega cos(\omega t)V_p\boldsymbol{i}$$

(6.4) can be done in the following way, which is mathematically strict since the surface integral along the cover surface Σ_1 can be done along the bottom surface Σ_2 where the normal vector is constant as $\mathbf{n} = -\mathbf{j}$.

$$\boldsymbol{F}_{FK} = \int_{\Sigma_1} (-\bar{p})\boldsymbol{n}ds = \rho U_m \omega \cos(\omega t) \int_{\Sigma_1} (x - L_x)\boldsymbol{n}ds$$

$$= \rho U_m \omega \cos(\omega t)\left[\oint_S (x - L_x)\boldsymbol{n}ds - \int_{\Sigma_2} (x - L_x)\boldsymbol{n}ds\right]$$

$$= \rho U_m \omega \cos(\omega t)\left[\int_{V_p} \nabla(x - L_x)dV - \int_{\Sigma_2} (x - L_x)\boldsymbol{n}ds\right]$$

$$= \rho U_m \omega \cos(\omega t)\left[V_p \boldsymbol{i} - (-\boldsymbol{j}) \int_{-x_1}^{x_1} (x - L_x)dx\right]$$

$$= \rho U_m \omega \cos(\omega t)\left[V_p \boldsymbol{i} - 2L_x x_1 \boldsymbol{j}\right] = \rho U_m \omega \cos(\omega t)\left[V_p \boldsymbol{i} - l_x L_x \boldsymbol{j}\right]$$

(6.5)

Therefore, in order to obtain the true vertical force, the vertical component of the FK force $F_{FKz} = U_m \omega cos(\omega t) l_x L_x$ (associated with the domain size L_x and the bottom length of the structure l_x as seen in Figure 6.4) should be subtracted. It can be seen in the following that after scaling to the actual scale, the value of F_{FKz} and the total vertical force F_{totalz}obtained directly from simulations are almost the same with a very large value ($\sim O(10^4)$) as seen in Figure 6.5. Therefore, the true vertical force $F_z = F_{\text{totalz}} - F_{FKz}$ (as a difference between F_{FKz} and F_{totalz} with large value) is very small ($\sim O(10^2)$) compared with F_{totalz} and F_{FKz}. Pay attention that F_{FKz} should be carefully calculated without any error in order to accurately obtain the sensitive difference value.

Based on these considerations, the results of the two methods of obtaining F_z are compared in Figure 6.6: a. setting the pressure boundary condition to cancel the inertial pressure induced FK force, seen in Eq (6.2), by setting the pressure boundary condition at the outlet as $p = U_m \omega cos(\omega t) L_x$. and b. subtracting the theoretically calculated F_{FKz} in post-processing. From Figure 6.6, it can be seen that the results obtained by both methods are consistent, demonstrating the theoretical validity and accuracy of the obtained results.

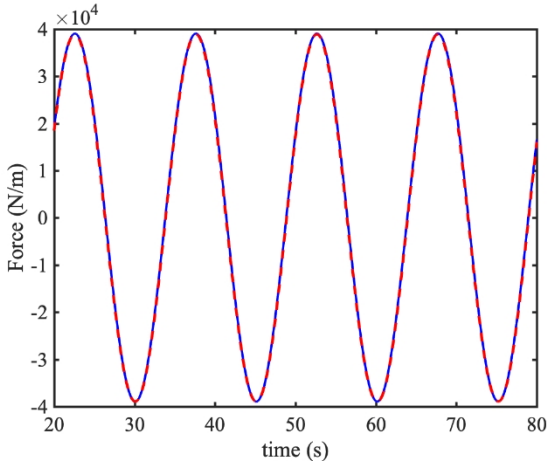

Figure 6.5 Time histories of F_{totallz} blue solid and the vertical FK force F_{FKz} red dashed for KC5

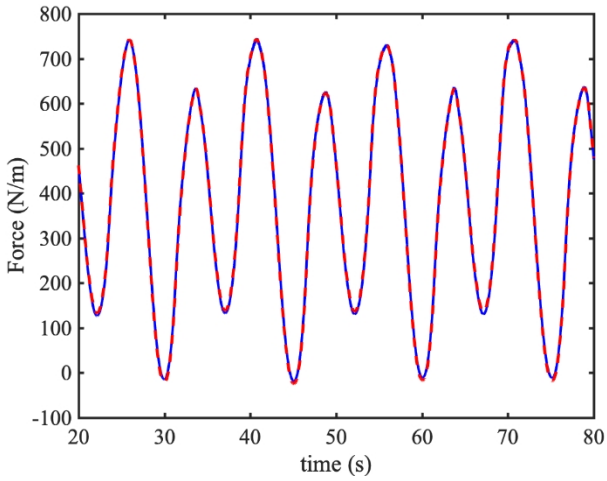

Figure 6.6 Time histories of F_z of cover by comparing 2 methods for KC=5

Error! Reference source not found. shows the results for different KC numbers of Case 1 and it can be seen that F_x is also perfect match with the experimental data, and F_z shows great agreement with the experimental data in KC=11 and 20 but only the low-KC number shows a little discrepancy. Therefore, the external surface of the subsea cover plays a decisive role in the force, and the interaction in the unconnected area under cover with plate is directly related to the F_z.

(a) (b)

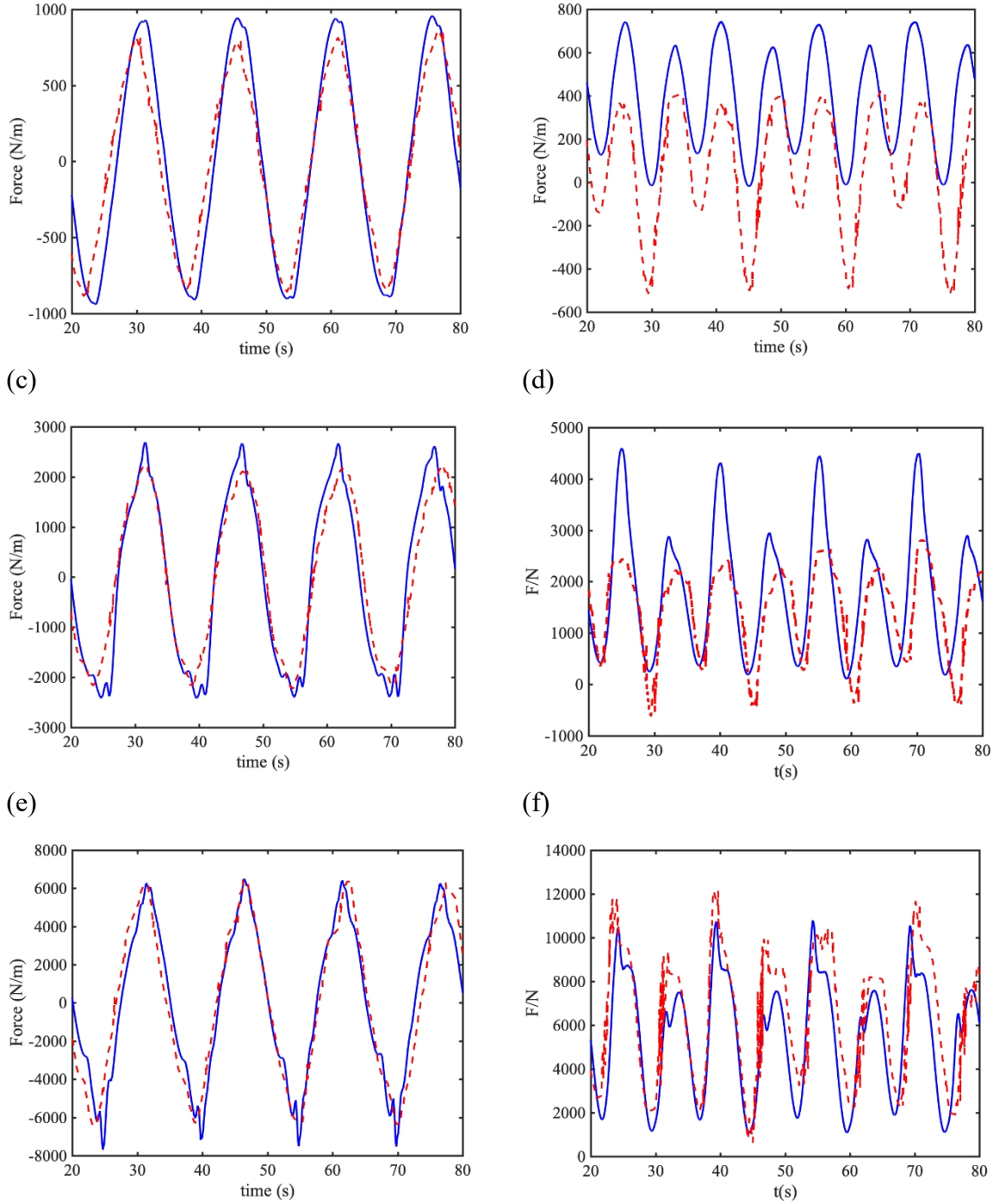

Figure 6.7 Time histories of F_x (left) and F_z (right) comparison with experiment data of dyncover case (red dash line) of case 1for KC=5 (a) and (b), 11 (c) and (d) and 20 (e) and (f)

Figure 6.8 to Figure 6.10 are plot contours of the spanwise vorticity and normalized pressure with streamlines of case 1 for KC=5 to KC=20. Overall, the geometry and flow conditions of Case 1 are closest to OCsolid cases, so the two were compared: the vorticity of Case 1 is simple. Basically, the vorticity appears only on the two corners on the top of cover and rolls down to

form a large vortex at the junction of cover and bottom. OCsolid cases are more complicated than Case 1 because additional vortices are generated in the gap and the two ends of the plate. Especially at KC=20, shown in Figure 5.29, the two kinds of additional vortex separate the vortex from the top of the cover so that the vortex shed off from the top are not touch and act on the junction of cover and bottom. This is probably the reason for the poor results for OCsolid of KC=20.

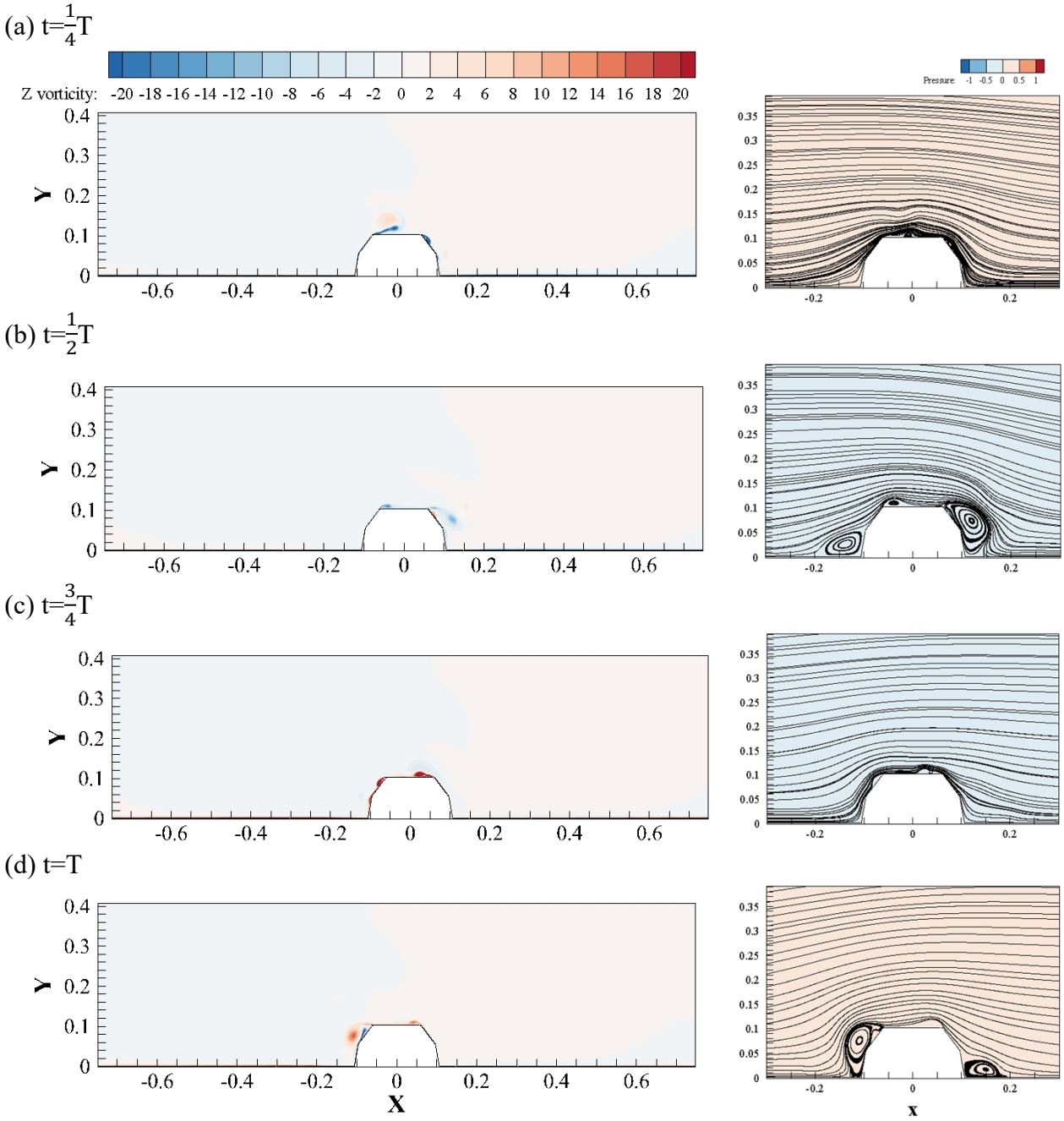

Figure 6.8 Contours of the spanwise vorticity and normalized pressure with streamlines of case 1 for KC=5

(a) t=$\frac{1}{4}$T

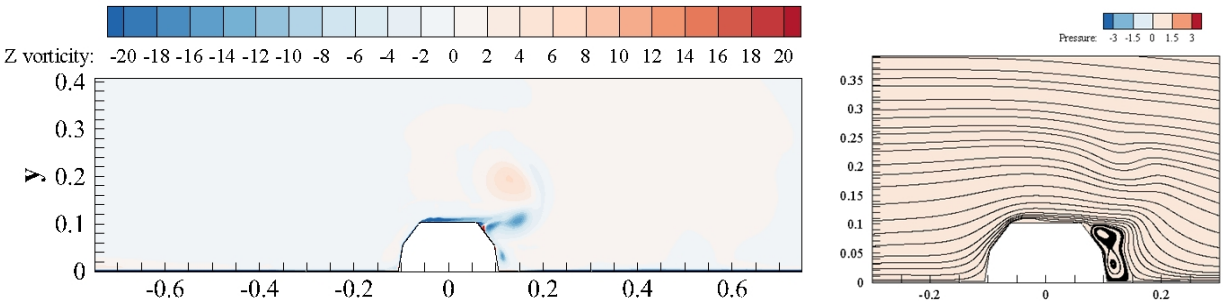

(b) t=$\frac{1}{2}$T

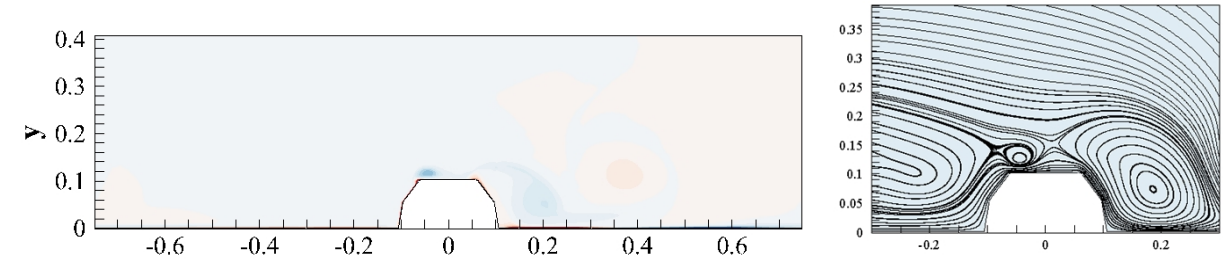

(c) t=$\frac{3}{4}$T

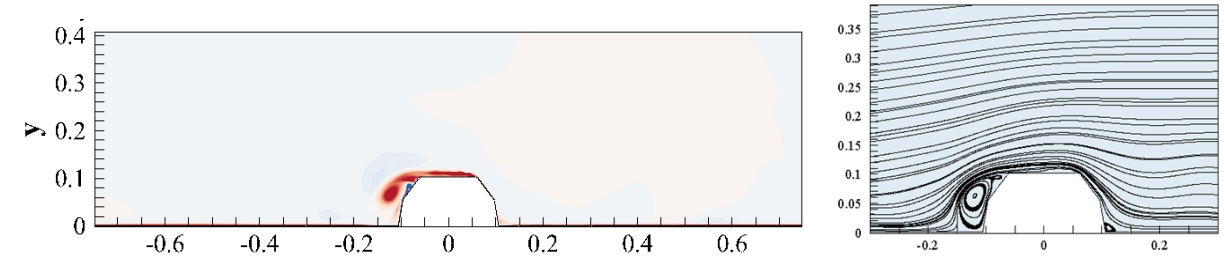

(d) t=T

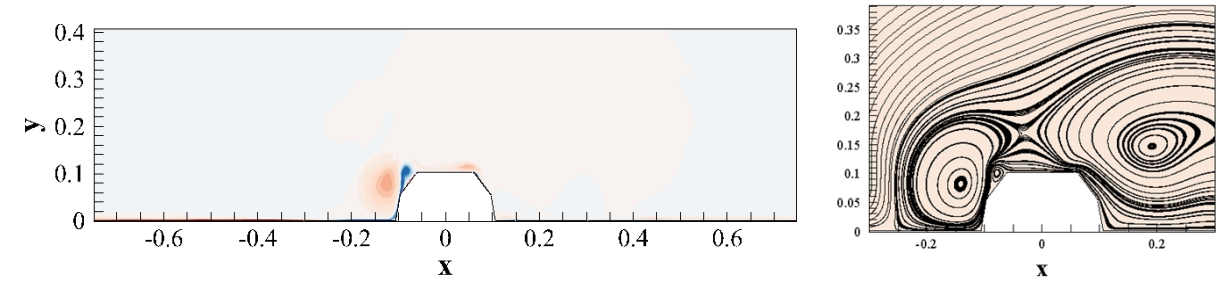

Figure 6.9 Contours of the spanwise vorticity and normalized pressure with streamlines of case 1 for KC=11

(a) t=$\frac{1}{4}$T

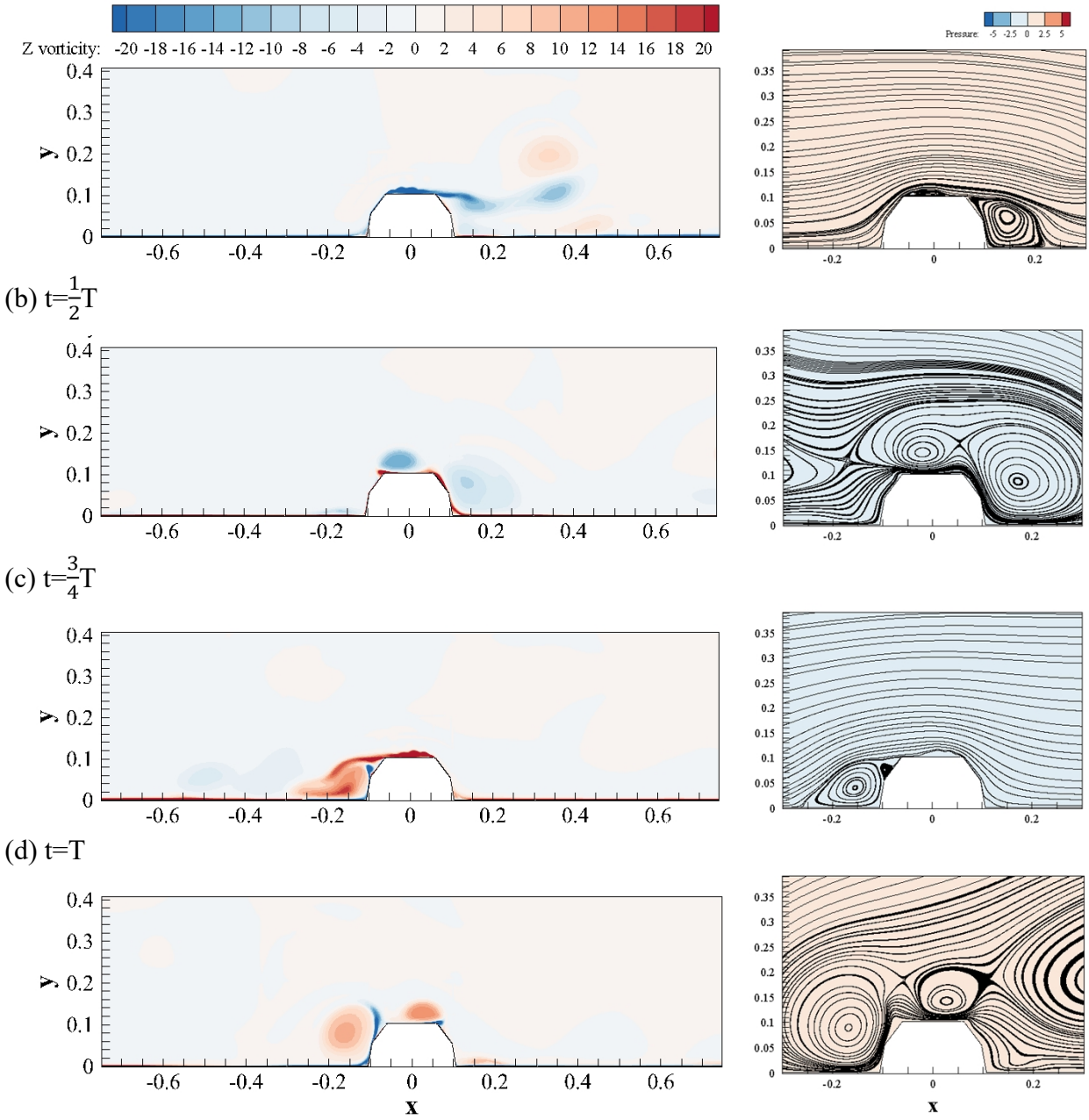

Figure 6.10 Contours of the spanwise vorticity and normalized pressure with streamlines of case 1 for KC=20

6.2.2 Case 2: cover on the domain bottom

In the original experimental set up, the flat plate below the subsea cover was used to act as a seabed floor and was moving together with the cover. However, in the real situation, the subsea covers are placed on the seabed. Therefore, oscillatory flows around a bottom-mounted subsea cover are also investigated. The computational domain and its sizes are shown in Figure 6.11.

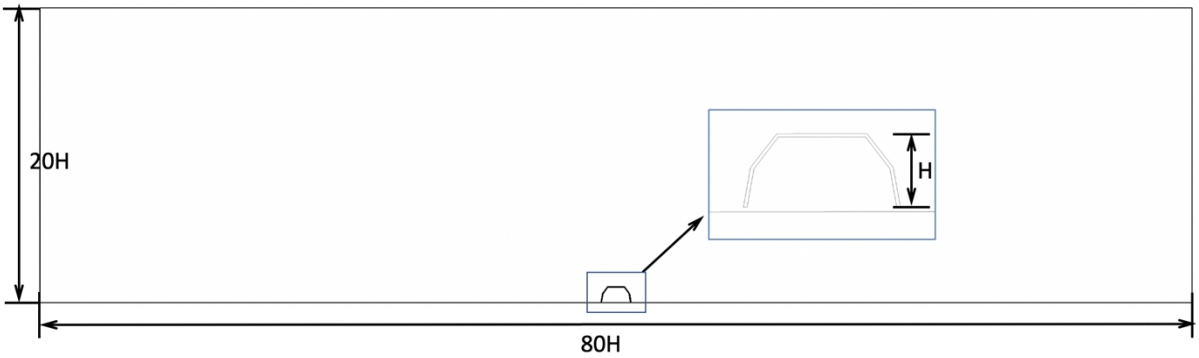

Figure 6.11 the computational domain and the subsea cover simulation model of case 1

Figure 6.12 (a) and (b) shows that at a low KC=5 number, the results for the subsea cover with the plate as used in the experimental set up are essentially the same as those for the Case 2 model placed at the bottom. Due to the low KC number, the flow field is reversed before it reaches the end of the plate such that the plate is long enough in a period.

Figure 6.12 (c) and (d) shows that at high KC=20 numbers, the predicted F_z for Case 2 is significantly larger than the experimental values and the previous results for the cover on a flat plate. This may be because for higher KC numbers, a longer flow path is required for the flow field to be fully developed and the separation flows around the plate end may interact with the cover, which leads to the difference in the predicted F_z. Therefore, the results of Chapter 5.4.2 for KC=20 should be based on Case 2, so that the predicted F_z is consistent with that at low KC numbers.

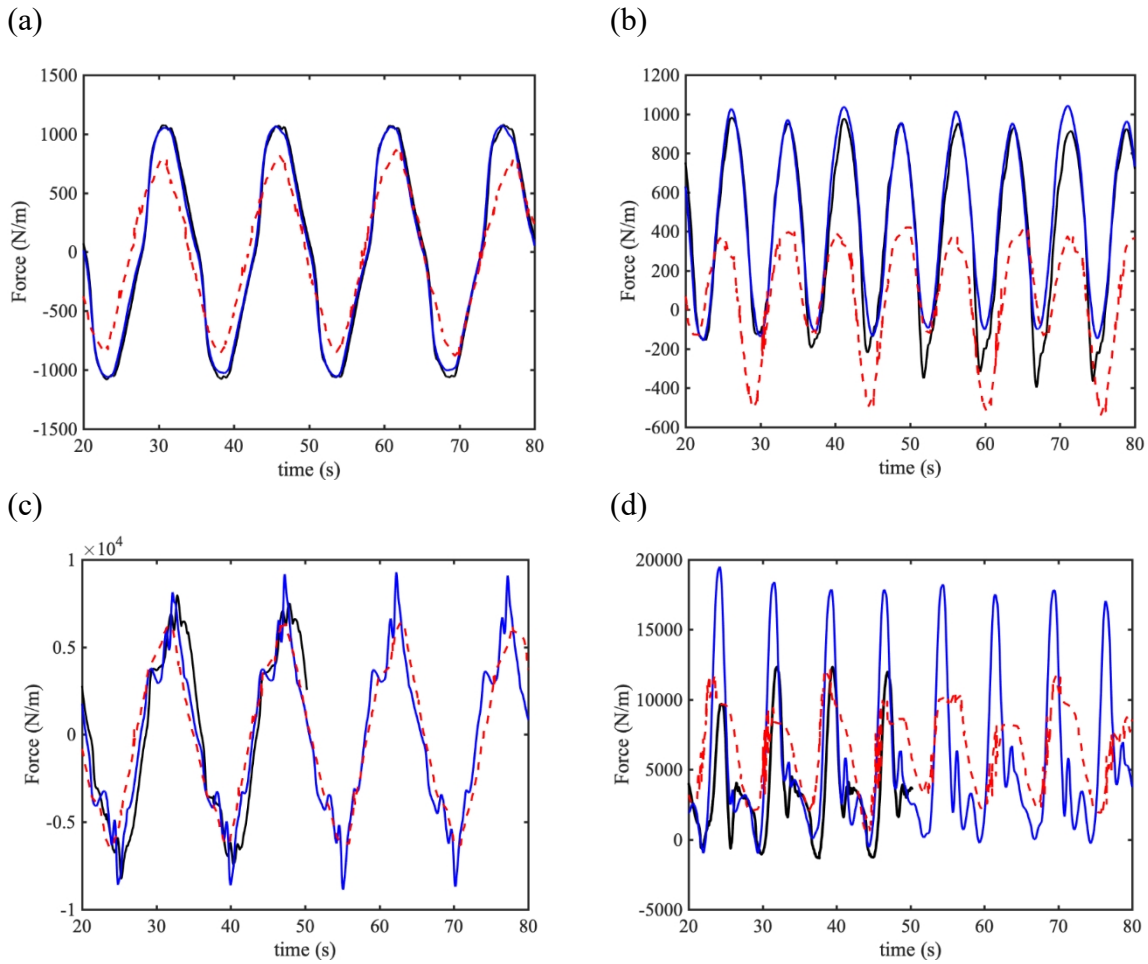

Figure 6.12 Time histories of F_x (left) and F_z (right) comparison with experiment data (red dash line) and previous results (dark line) of case 2 for KC=5 (a) and (b) and 20 (c) and (d)

6.2.3 Case 3: subsea covers with baffles of different lengths

Having determined that the subsea cover model should be placed at the bottom of the computational domain, a detailed investigation of F_z will be conducted for cases with KC=20. It can be seen from the vorticity structures displayed in Chapter 5.5 that the flow communications between the inside and outside the subsea cover have great influences on the lift force on the cover, which leads to the different hydrodynamic behaviors between OCcover and OCsolid cases. In the experimental set up, the subsea cover is immersed in the water upside-down and due to the water gravity, there is limitation for the entrance of the water inside the cover. Therefore, a new attempt is made to reduce the water entrance inside the subsea cover by adding a baffle between the bottom and subsea cover to mimic the entrance limitation. The length of the baffle will influence the communication of the water between the inside and outside the subsea cover. In this section, four different lengths of the baffle with openings of

1/2, 1/4, 1/8 and 1/16 of the subsea cover bottom length are considered, which are named as Case 3-I, Case 3-II, Case 3-III and Case 3-IV, as shown in Figure 6.13.

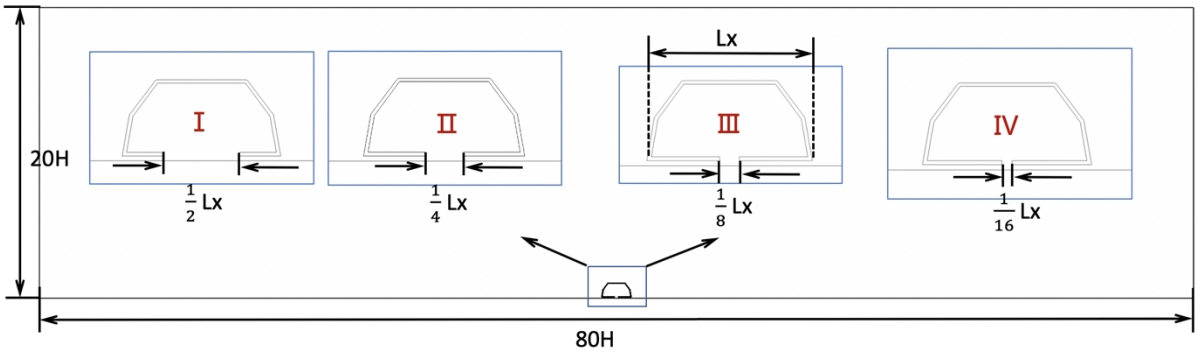

Figure 6.13 the computational domain and the subsea cover simulation model of Case 3

The numerical simulations for the four cases are carried out at KC=20 and the results are shown in *Figure* 6.14. The F_x shown in Figure 6.14 still matches well with the experimental data and its dependence on the baffles lengths is weak. With the decreasing length of the opening on the bottom edge of the subsea cover, F_z will also progressively become slightly smaller and closer to the experimental data. The improvement of the predicted F_z compared with the experimental data as further shown in Figure 6.15 compared with the results of Case 2 shows that in practice the water inside the cover indeed should be considered, however should be regarded as 'frozen water' and the communications between the inside and outside the cover should be limited. Moreover, as the length of the baffle increases and the opening decreases, the results are closer to the experimental data. Even for openings of 1/16 of the subsea cover, the peak of F_z already matches the experimental value.

(a)

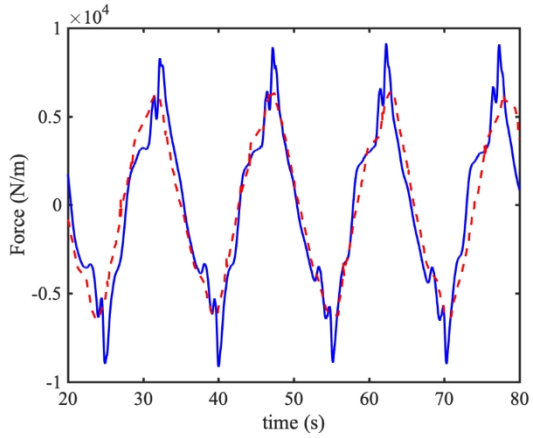
×10^4
1
0.5
0
-0.5
-1
Force (N/m)
20
30
40
50
60
70
80
time (s)

(b)

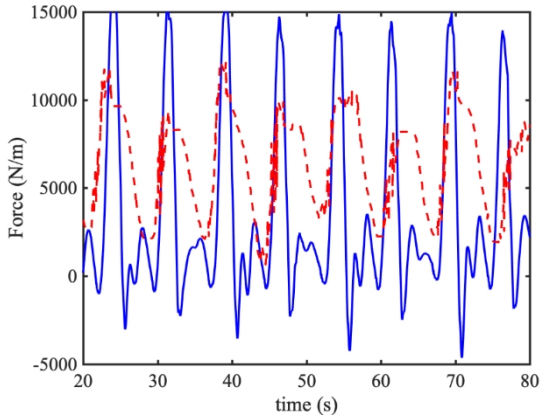
15000
10000
5000
0
-5000
Force (N/m)
20
30
40
50
60
70
80
time (s)

(c)

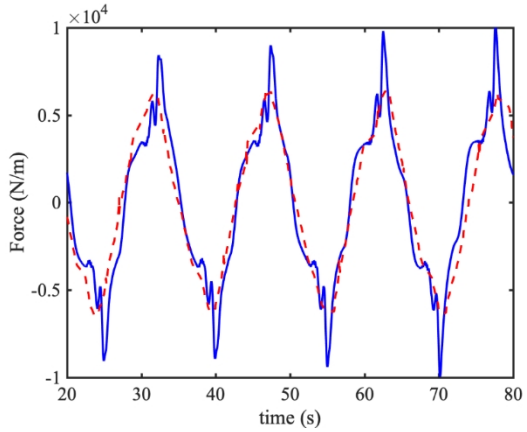
×10^4
1
0.5
0
-0.5
-1
Force (N/m)
20
30
40
50
60
70
80
time (s)

(d)

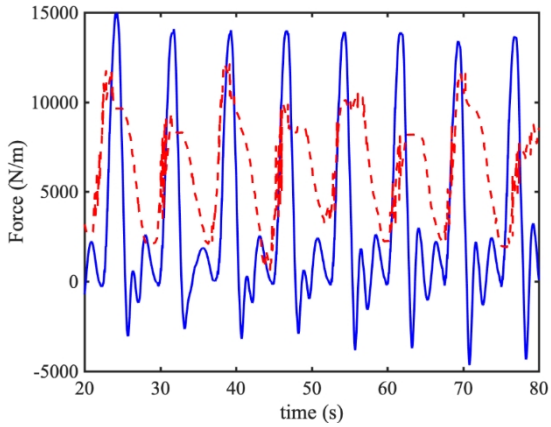
15000
10000
5000
0
-5000
Force (N/m)
20
30
40
50
60
70
80
time (s)

(e)

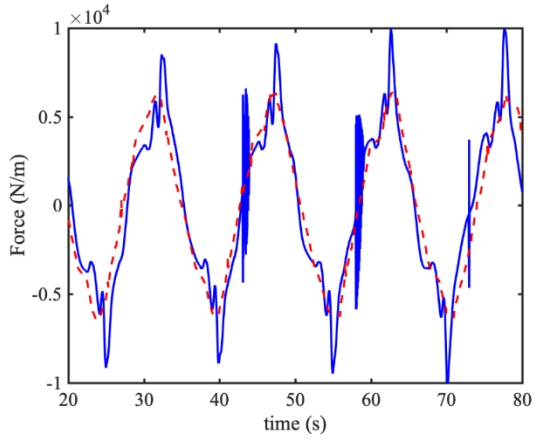
×10^4
1
0.5
0
-0.5
-1
Force (N/m)
20
30
40
50
60
70
80
time (s)

(f)

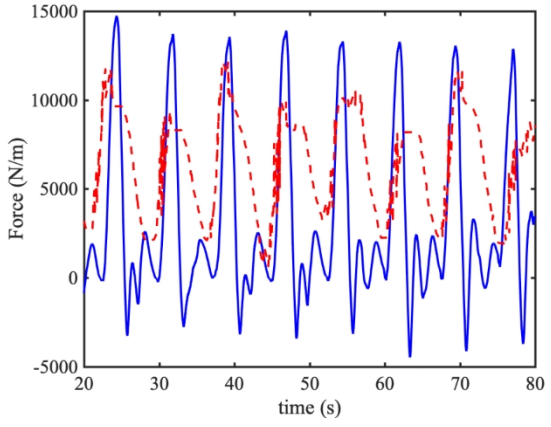
15000
10000
5000
0
-5000
Force (N/m)
20
30
40
50
60
70
80
time (s)

(g)

×10^4
1
0.5
0
-0.5
-1
Force (N/m)
20
30
40
50
60
70
80
time (s)

(h)

15000
10000
5000
0
-5000
Force (N/m)
20
30
40
50
60
70
80
time (s)

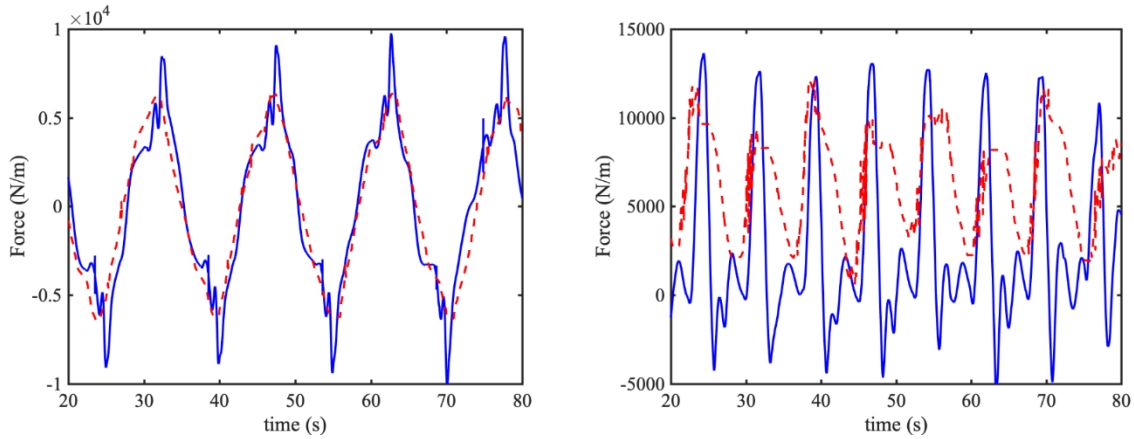

Figure 6.14 Time histories of Fx (left) and Fz (right) comparison with experiment data (red dash line) of Case 3-I (a) and (b), Case 3-II (c) and (d), Case 3-III (e) and (f) and Case 3-IV (g) and (h) for KC=20

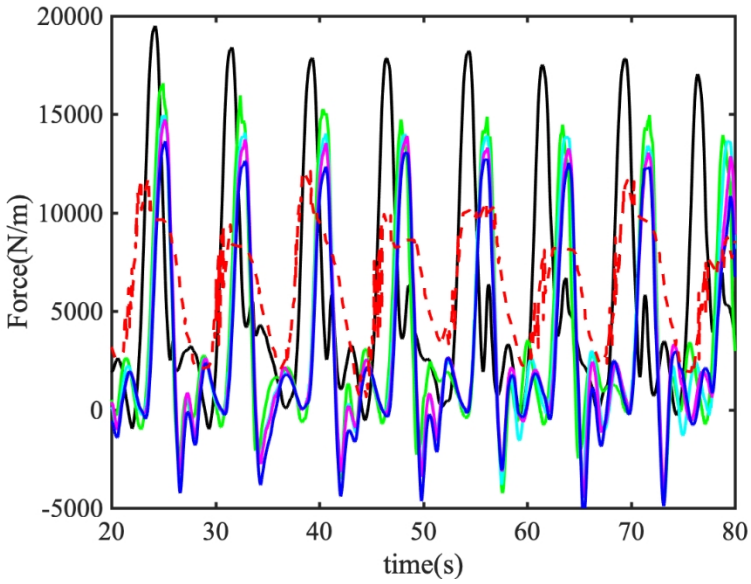

Figure 6.15 Time histories of F_z of Case 3-I (green line), Case 3-II (cyan line), Case 3-III (magenta line) and Case3-IV (blue) with experiment data (red dash line) and Case 2 (dark line) for KC=20

Figure 6.16 to Figure 6.19 present contours of the spanwise vorticity and normalized pressure with streamlines of Case 3-I to Case 3-IV. The flow field outside the cover is basically the same, while the performance of the four cases inside the cover is slightly different. Three vortices exist inside the cover of Case 3-I, and the energy exchange with the bottom flow field is so strong and frequent in one period that the vortex in the middle moves laterally inside the cover frequently. Case 3-II and Case 3-III are similar streamline pattern inside cover: there are

four vortices symmetrically distributed inside the cover, and they become more stable. The two vortices on the far side of Case 3-III are smaller compared to Case 3-II because of the smaller opening. When the opening is 1/16 length of the subsea cover bottom length, the vortexes inside cover reduced to three. Two main vortexes are almost stationary, and the middle small one varied with time. Therefore, the size of the opening determines the amount of the energy exchange, and 1/16th of the opening is small enough to make the results acceptable.

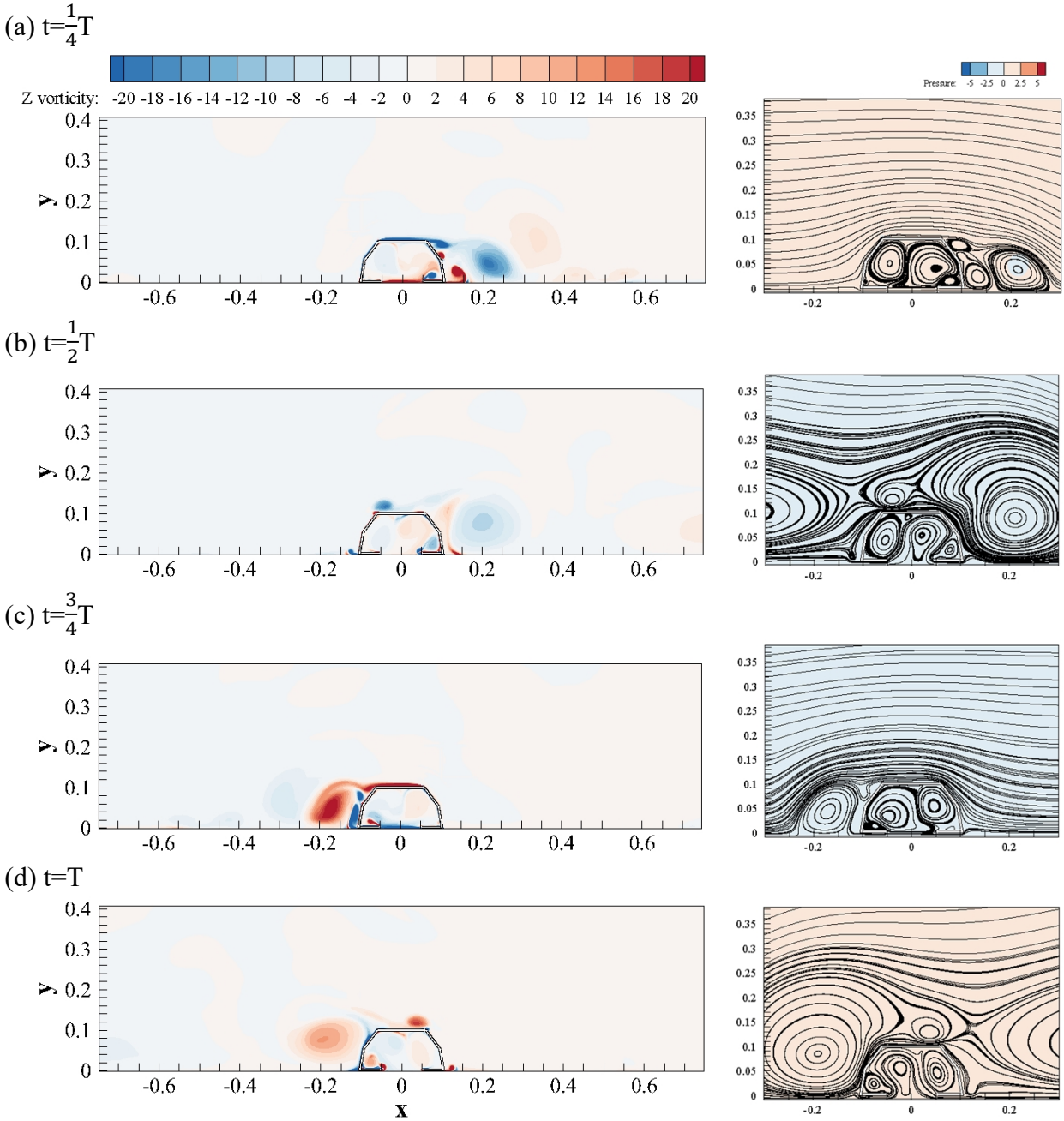

Figure 6.16 Contours of the spanwise vorticity and normalized pressure with streamlines of Case 3-I for KC=20

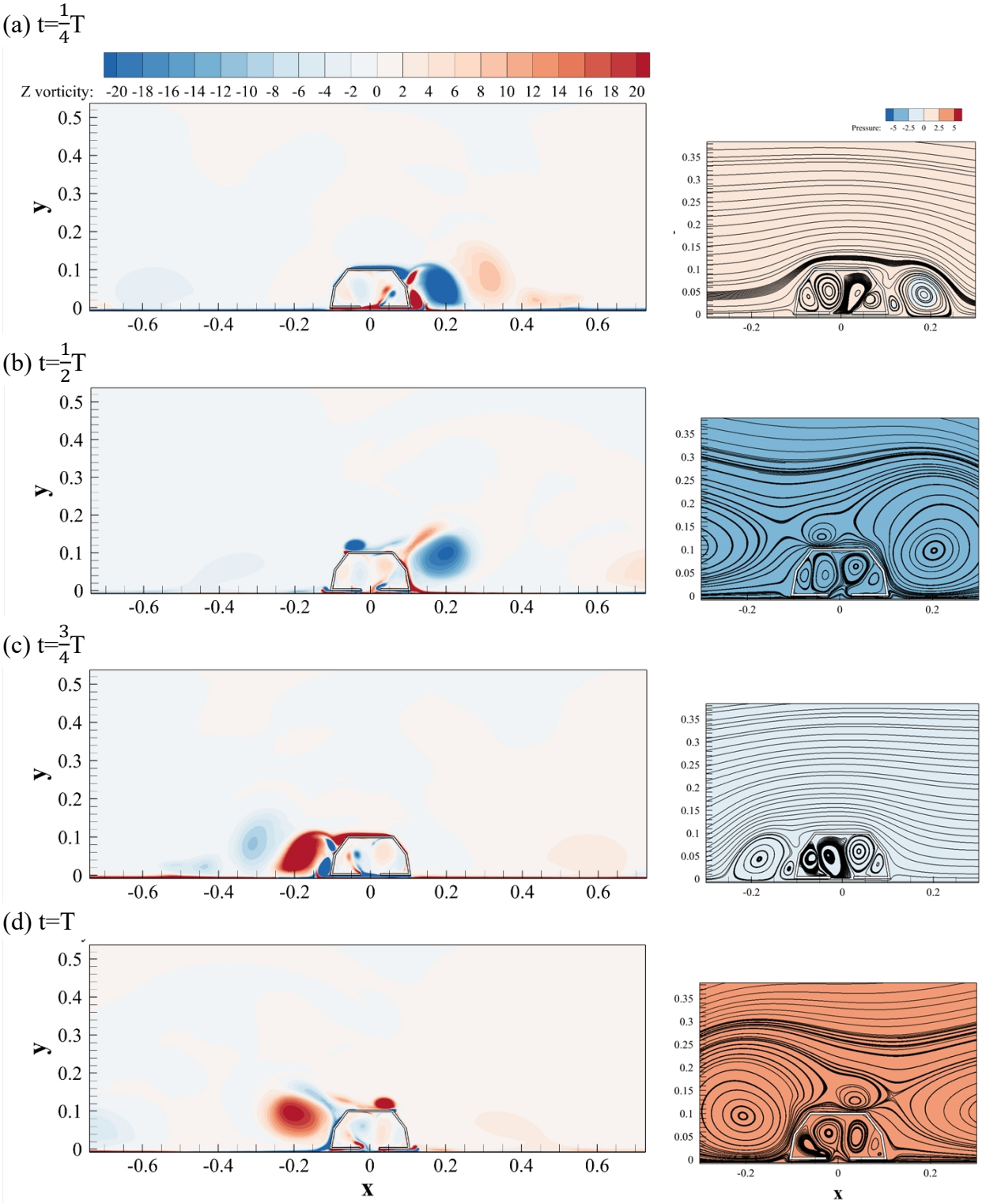

Figure 6.17 Contours of the spanwise vorticity and normalized pressure with streamlines of Case 3-II for KC=20

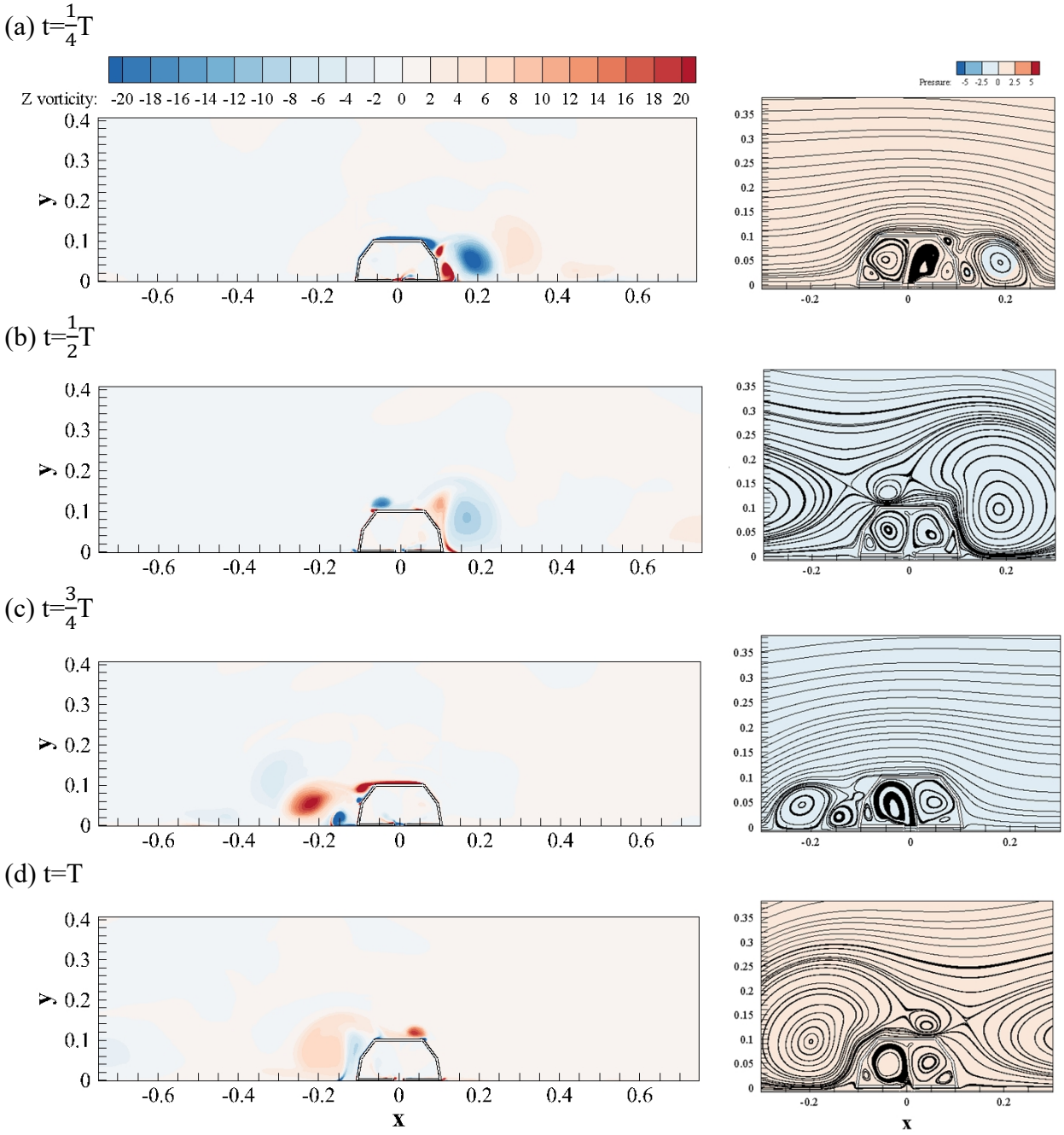

Figure 6.18 Contours of the spanwise vorticity and normalized pressure with streamlines of Case 3-III for KC=20

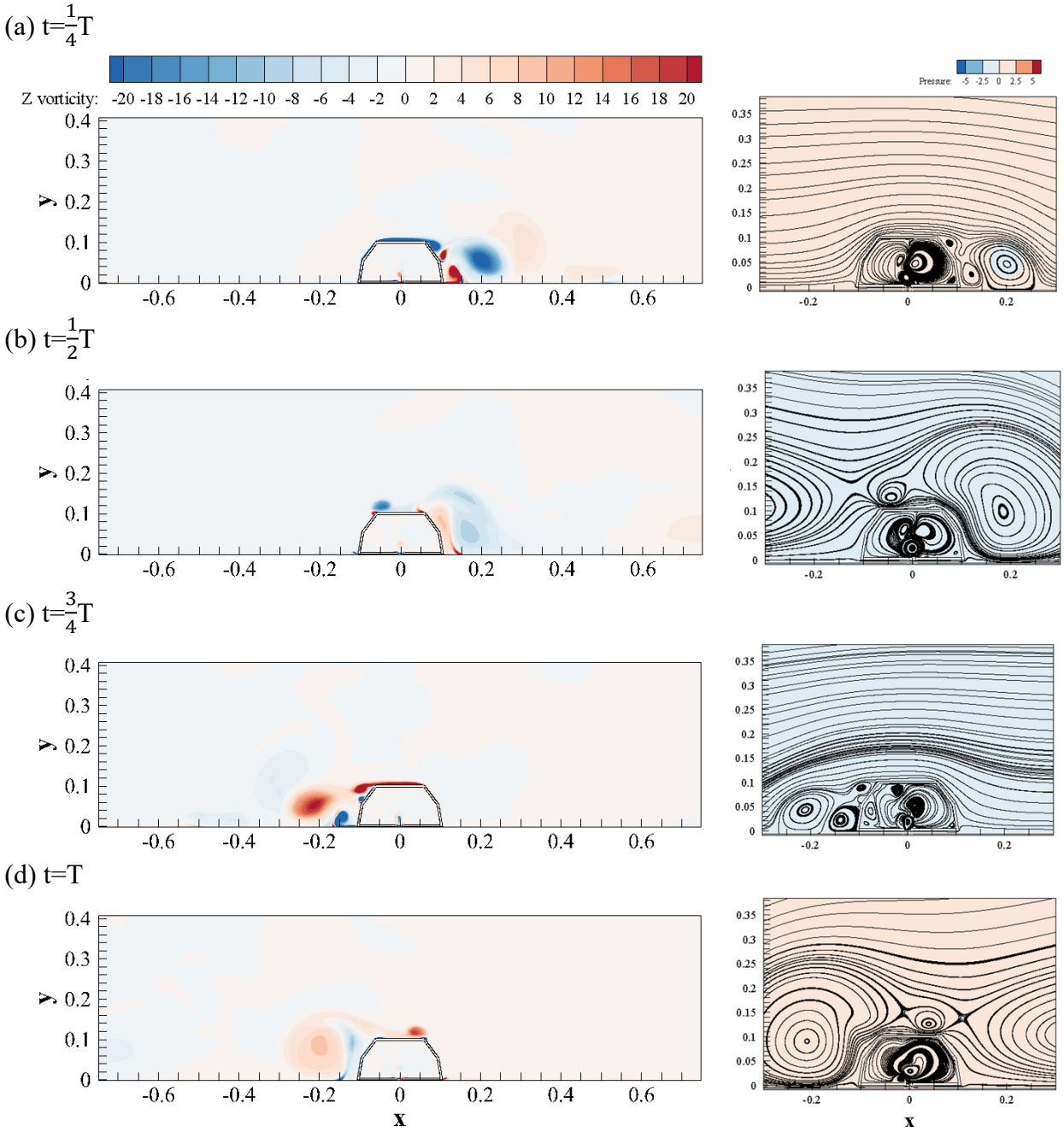

Figure 6.19 Contours of the spanwise vorticity and normalized pressure with streamlines of Case 3-IV for KC=20

Similarly, comparisons are made for KC=5 and KC=11 for 1/8 and 1/16 opening as shown in Figure 6.20. It can be seen that predicted results for the 1/16 opening are indeed slightly better than those for 1/8 baffles compared with the experimental data, which is also in consistence with the results for KC=20. Therefore, it can be concluded that the numerical model for the 1/16 opening baffles can be regarded as the closet to the experimental set up as shown in Figure 6.21.

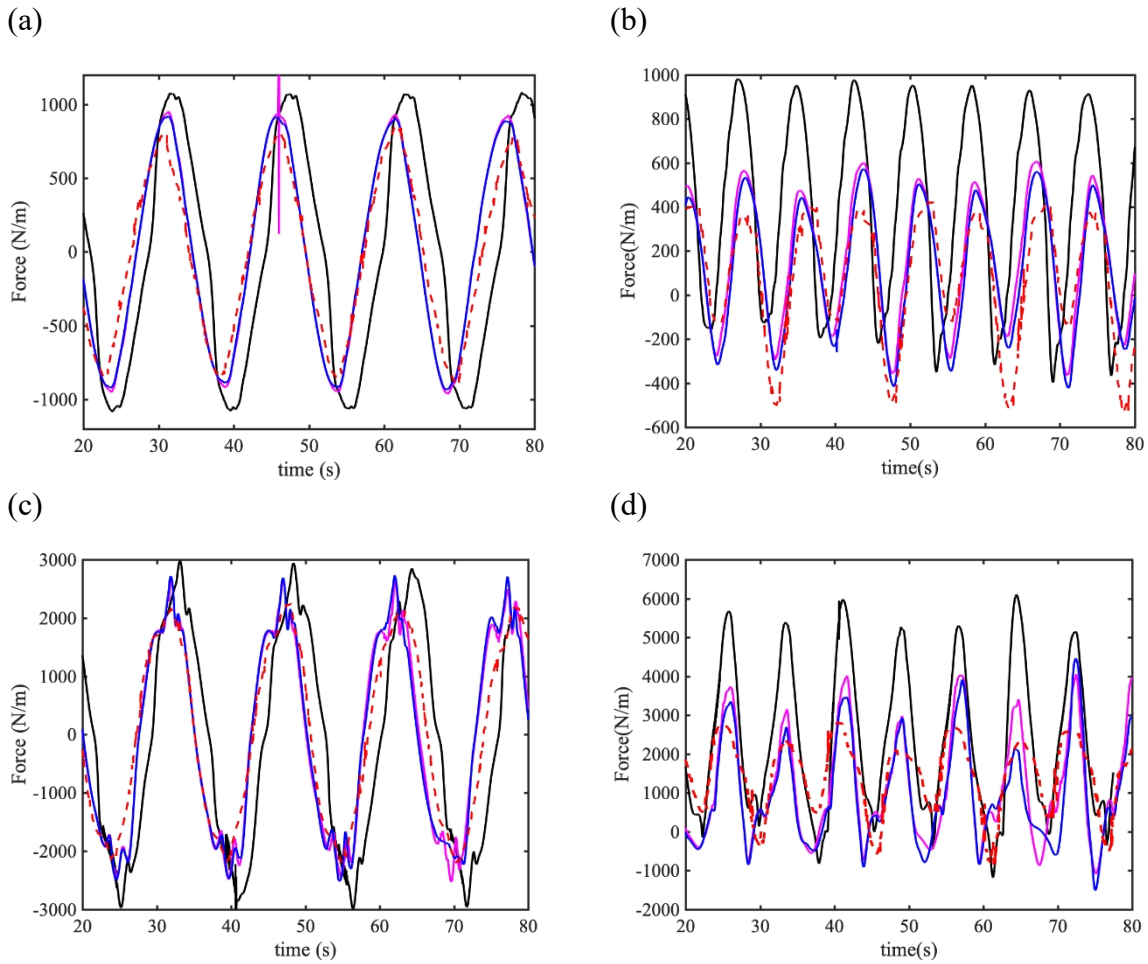

Figure 6.20 Time histories of Fz of Case 3-III (magenta line) and Case3-IV (blue) with experiment data (red dash line) and Case 2 (black line) for KC=5 (a) and (b) and KC=11 (c) and (d)

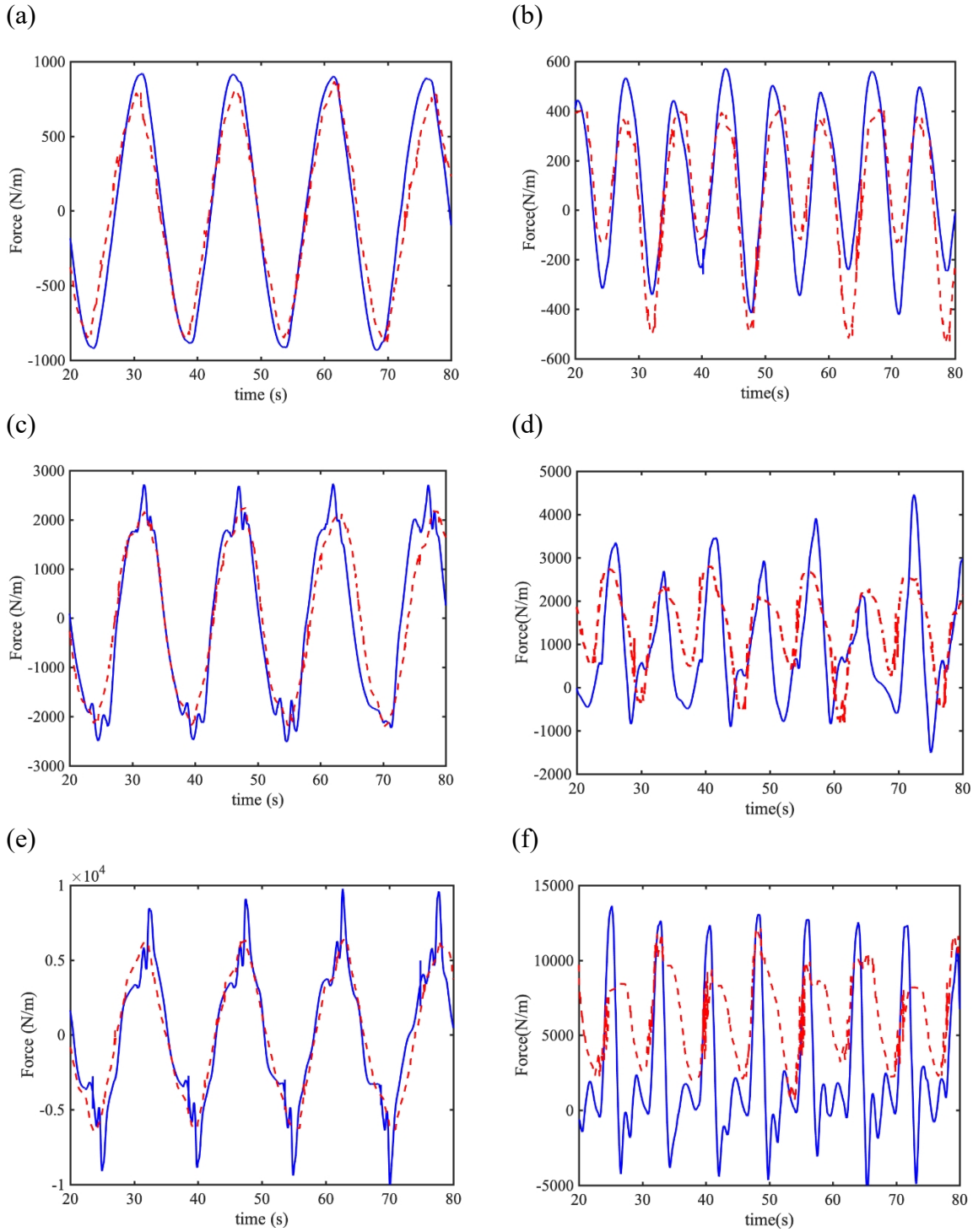

Figure 6.21 Time histories of F_z of Case 3-IV (blue) with experiment data (red dash line) for KC=5 (a) and (b), KC=11 (c) and (d) and KC=20 (e) and (f)

Figure 6.22 to Figure 6.24 present contours of the spanwise vorticity and normalized pressure with streamlines of Case3-IV for KC=5 to KC=21. For different KC number, there are different vorticity and streamline patterns, but for each case, the patterns hardly change with time.

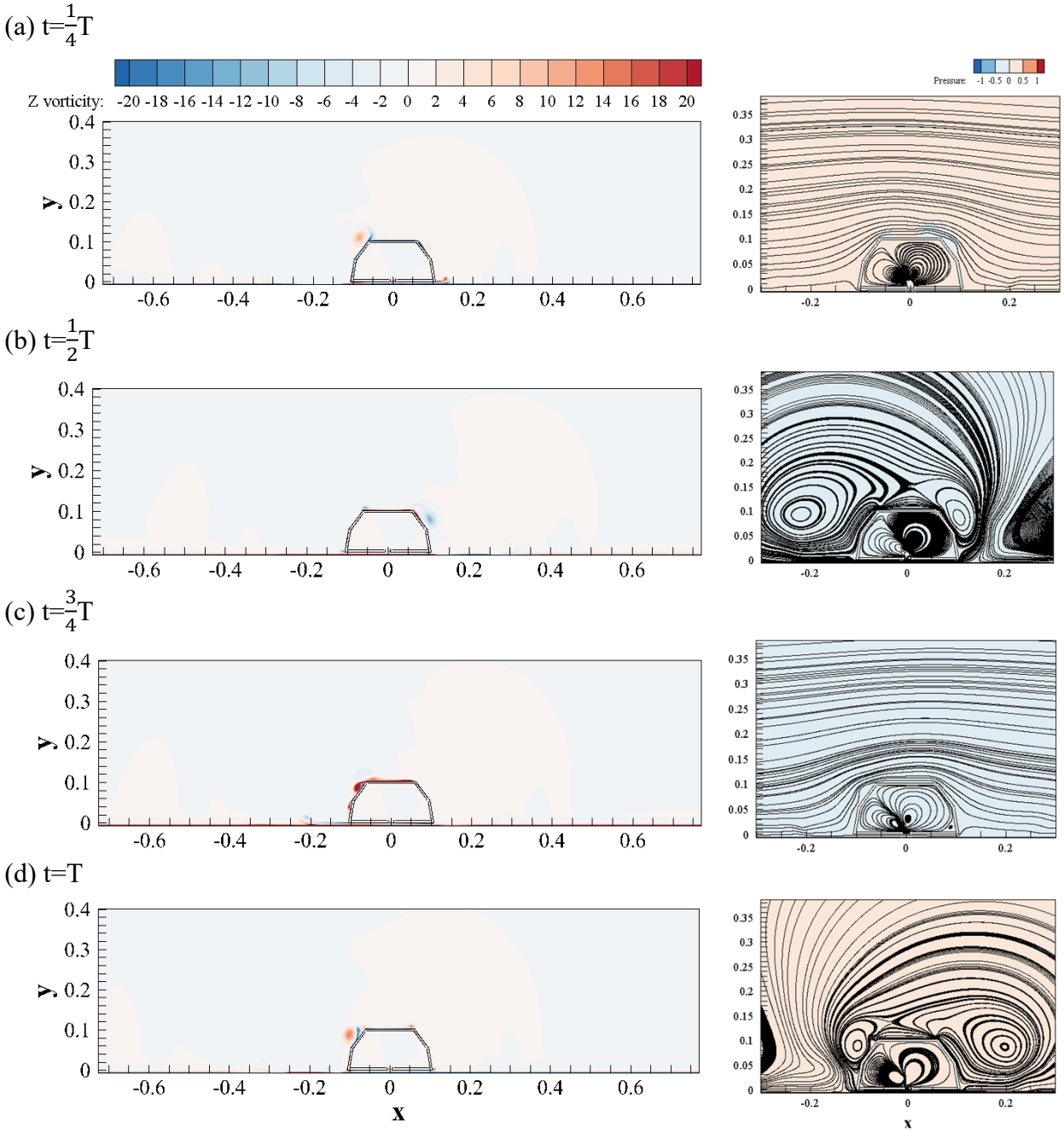

Figure 6.22 Contours of the spanwise vorticity and normalized pressure with streamlines of Case 3-IV for KC=5

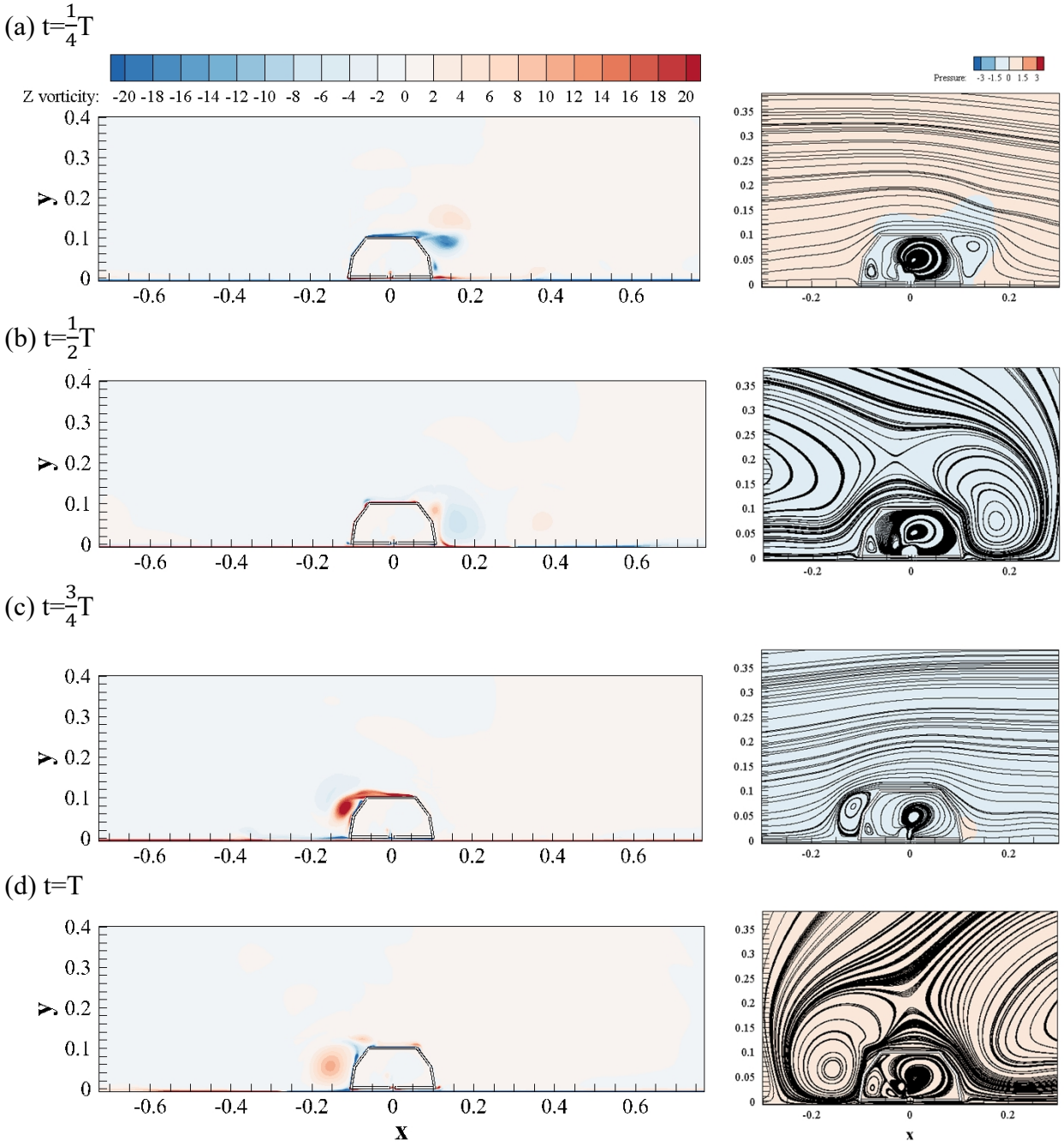

Figure 6.23 Contours of the spanwise vorticity and normalized pressure with streamlines of Case 3-IV for KC=11

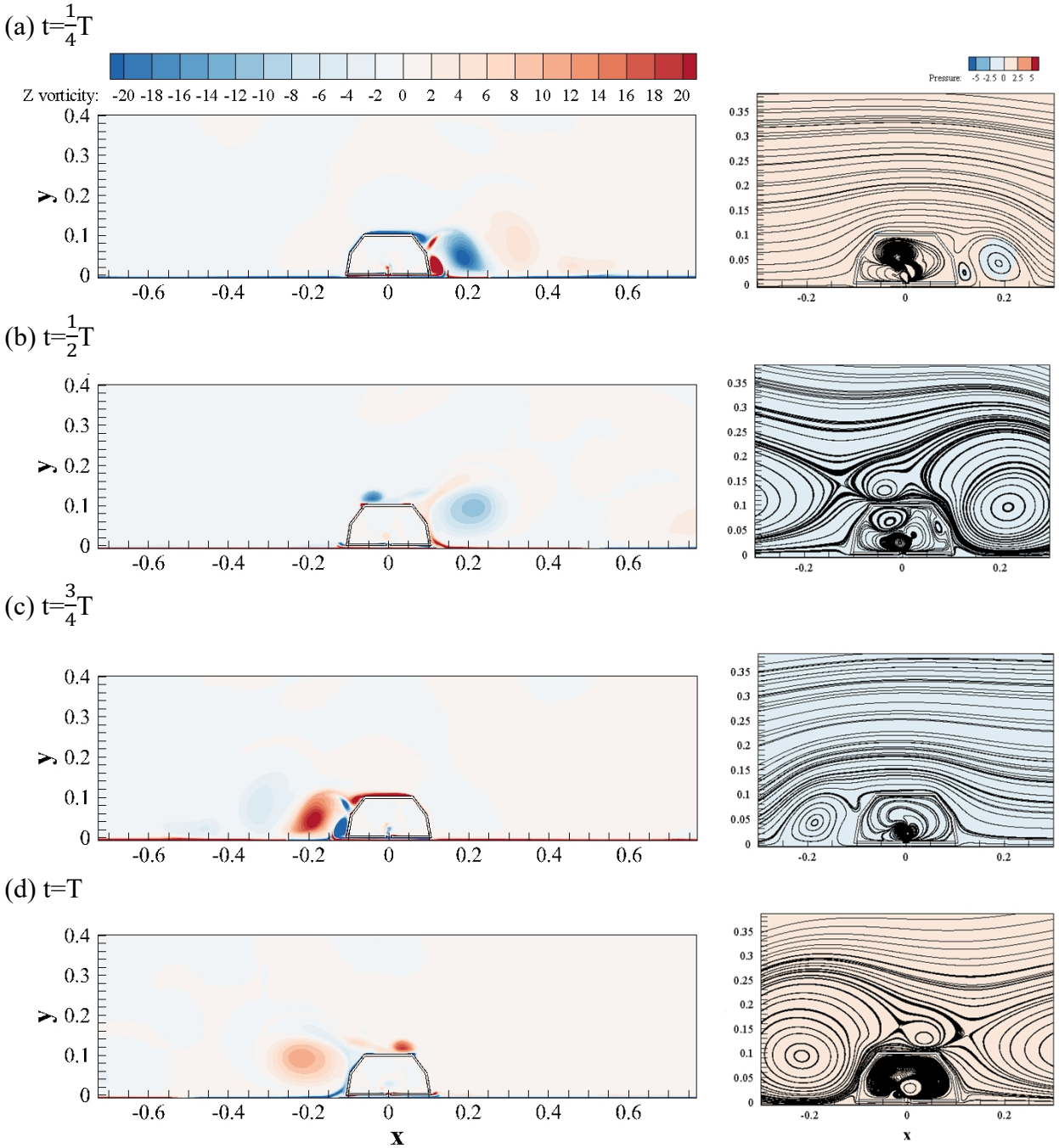

Figure 6.24 Contours of the spanwise vorticity and normalized pressure with streamlines of Case 3-IV for KC=21

6.3 Summary

In this chapter, a revision to the computation set up is investigated and three cases are considered, which set up and analyze the effects of the inner surface of the cover, the plate under the cover and the water entering the inside of the cover.

Case 1 set up that cover only shell connected with domain, and compared with 2 kind of experiment data. One for the similar structure, but huge discrepancy shows. Another still compare to experiment data of the dyncover, which is perfect match, indicating the external surface of the subsea cover plays a decisive role in the force, and the interaction in the unconnected area under cover maybe the key to improving F_z.

Case 2 is the case to establishing the foundation of cover setting up on the bottom of computational domain. The results prove the consistence of position in the domain wherever the subsea cover set up. And also considering the case of KC=20, the 'longer plate' of Case 2 is more realistic to F_z.

Case 3 is combined Case 1 and Case 2, not only settle the subsea cover on the bottom, but also add the baffle to prevent the water interaction with interior of cover and the water in the gap still influence on the cover. For further investigating the length of baffle impact on cover, 4 kinds of length are set and compared. And 3 KC numbers are all agree with the longest baffle and the results are perfect match. With the baffle length increased, the results of F_z are closer to experiment data. Therefore, the longest baffle case is as the final model used for further exploration next chapter in this paper.

7 Dynamic Mode Decomposition analysis for the flow around subsea cover

For the DMD analysis, a total number of N=300 snapshots are considered over 15 cycles of oscillation. Successive snapshots are uniformly apart from each other by t/T=1/20. The DMD analysis is carried out for z vorticity presenting by x-direction (u) and y-direction (v) of the whole computational domain for Case 3-IV at KC=5,11 and 21. Upon performing DMD analysis, the sparsity-promoted algorithm is further used to extract the dominant flow features of the DMD modes.

7.1 Case 3-IV for KC=5

Figure 7.1 (a) shows the residual $\|\boldsymbol{X} - \Phi D_a \mathrm{V}_{\mathrm{and}}\|_F$ of the optimal vector of amplitudes a, resulting from the sparsity-promoting DMD algorithm, in fraction of $\|\boldsymbol{X}\|_F$,

$$\%\Pi_{\mathrm{loss}} = 100\sqrt{\frac{J(a)}{J(0)}} = 100\frac{\|\boldsymbol{X} - \Phi D_a \mathrm{V}_{\mathrm{and}}\|_F}{\|\boldsymbol{X}\|_F}, \tag{7.1}$$

with sparsity-promoting parameter gamma γ. Figure 7.1 (b) shows a function of the number of the retained DMD modes, $N_z = \mathrm{card}(a)$ with γ.

As sparsity-promoting parameter gamma γ increases, i.e., as emphasis on sparsity, the non-zero elements N_z in the vector a gradually decrease and the quality of least-squares approximation deteriorates, so the $\%\Pi_{\mathrm{loss}}$ increases. A further reduction in the number of DMD modes has strong impact on the quality of the approximation of the generated snapshots obtained using the numerical simulations. Therefore, the results show in Figure 7.1 (a) and (b) suggest that a reasonable compromise between the quality of approximation $\%\Pi_{\mathrm{loss}}$ and the number of the retained DMD modes N_z can be chosen such that $N_z = 2$, i.e two modes can capture up to $1 - \%\Pi_{\mathrm{loss}} \approx 80\%$ of the total energy of the flow field.

The eigenvalues of the reduced-order linear operator matrix A are shown in Figure 7.1 (c). It can be seen that most of the modes are located close to the unit circle indicating that most of the modes are neutrally stable along the dynamical evolution of the systems. The modes located inside the unit circle correspond to those are quickly damped along the evolution. The frequencies of the modes calculated as Im(log(λ_i))/dt and their amplitudes obtained using sparsity-promoted algorithm are shown in Figure 7.1 (a). It can be seen that the most dominant modes with Nz=2 come in pairs with an opposite sign of the frequency. The frequency of the dominant mode is 0.25 s^{-1} which is in consistent with the characteristic frequency of the

oscillatory flow. The streamwise and cross-stream velocities of the dominant mode are shown in Figure 6.22. It can be seen that the high velocity regions are located around the top corners of the subsea cover, which is in consistent with the localized behavior for this low KC.

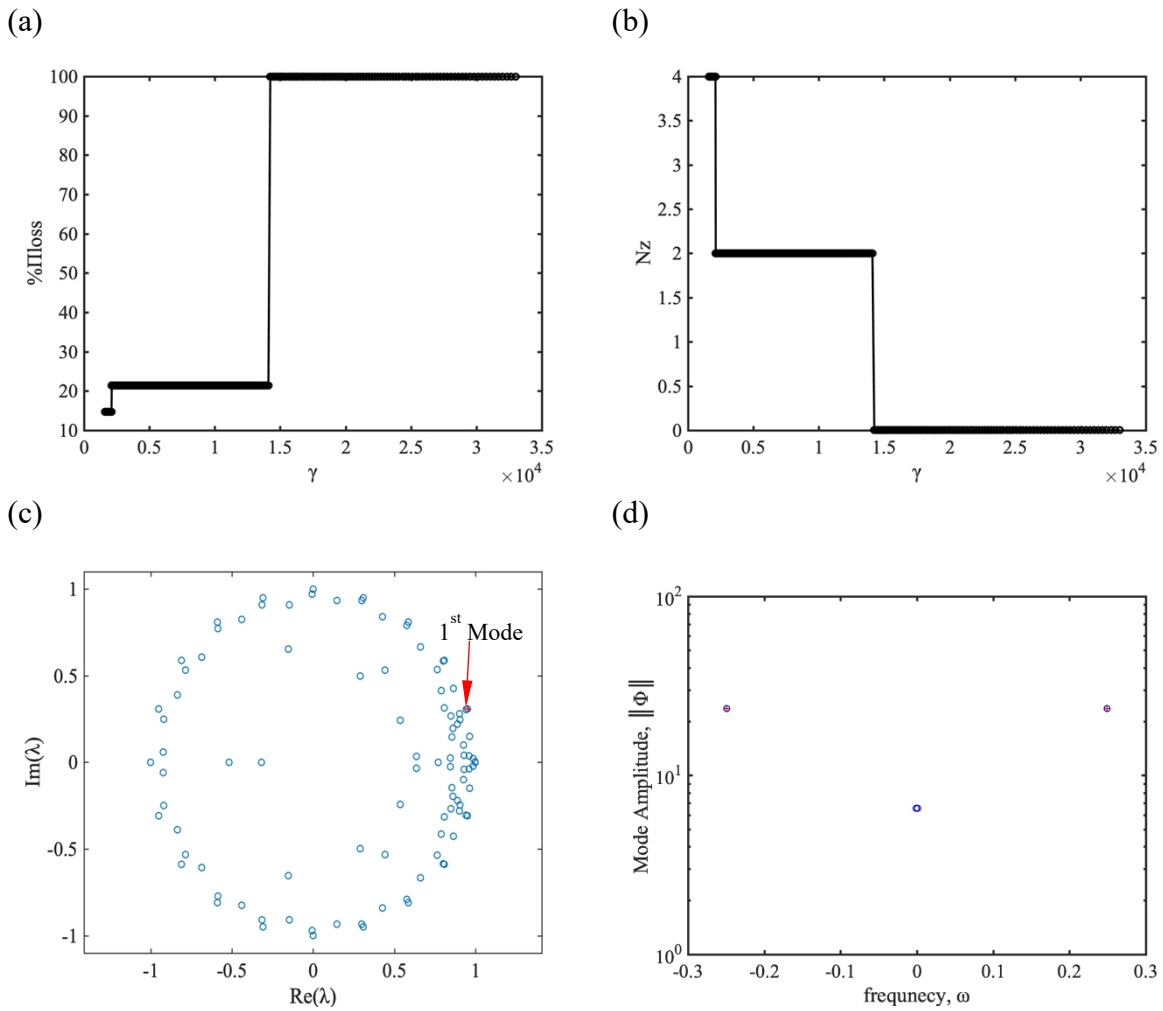

Figure 7.1 KC=5 (a) Performance loss $\%\Pi_{\text{loss}}$ of the optimal vector of amplitudes a with sparsity-promoting parameter gamma. (b) The function of the number of the retained DMD modes N_z with sparsity-promoting parameter gamma (c) Ritz values of the first mode and (d) Mode amplitude vs frequency of full-rank DMD algorithm (blue circle) and reduced modes (red plus)

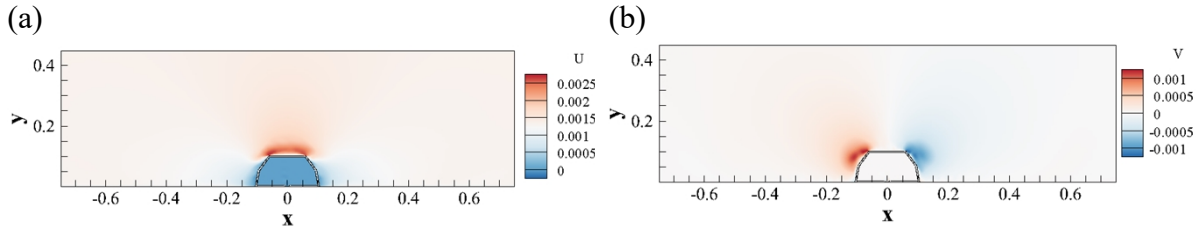

Figure 7.2 The first spatial DMD modes for KC=5 (a) real part of DMD modes (b) imaginary part of DMD modes

7.2 Case 3-IV for KC=11

The DMD analysis results are shown in Figure 7.3. The mode selection process is consistent with the KC=5 case, and as the KC number increases and the surrounding flow field is relatively becoming complex, the dominant modes number increases to capture approximately 80% of the total energy. Three dominant modes are identified in Figure 7.3 (d) and their corresponding mode shapes are shown in Figure 7.4 by their streamwise and cross-stream velocities. The first mode of KC=11 at St=0.09 is almost the same as KC=5 case. From the cross-stream velocity, the mode shape is more expanded around the corners of the subsea cover. The second mode has the twice of frequency of the dominant mode, which refers to the second harmonics of the first mode. The wave-packet form of flow structures with alternate distributions of the positive and negative values indicates the advection of the shed vortices as seen in Figure 6.23. The third mode at St=0.27 corresponds to the third harmonic of the first mode. It can be seen that the overall mode shapes are similar to those for the second mode except that the length scales of the flow structures are becoming smaller.

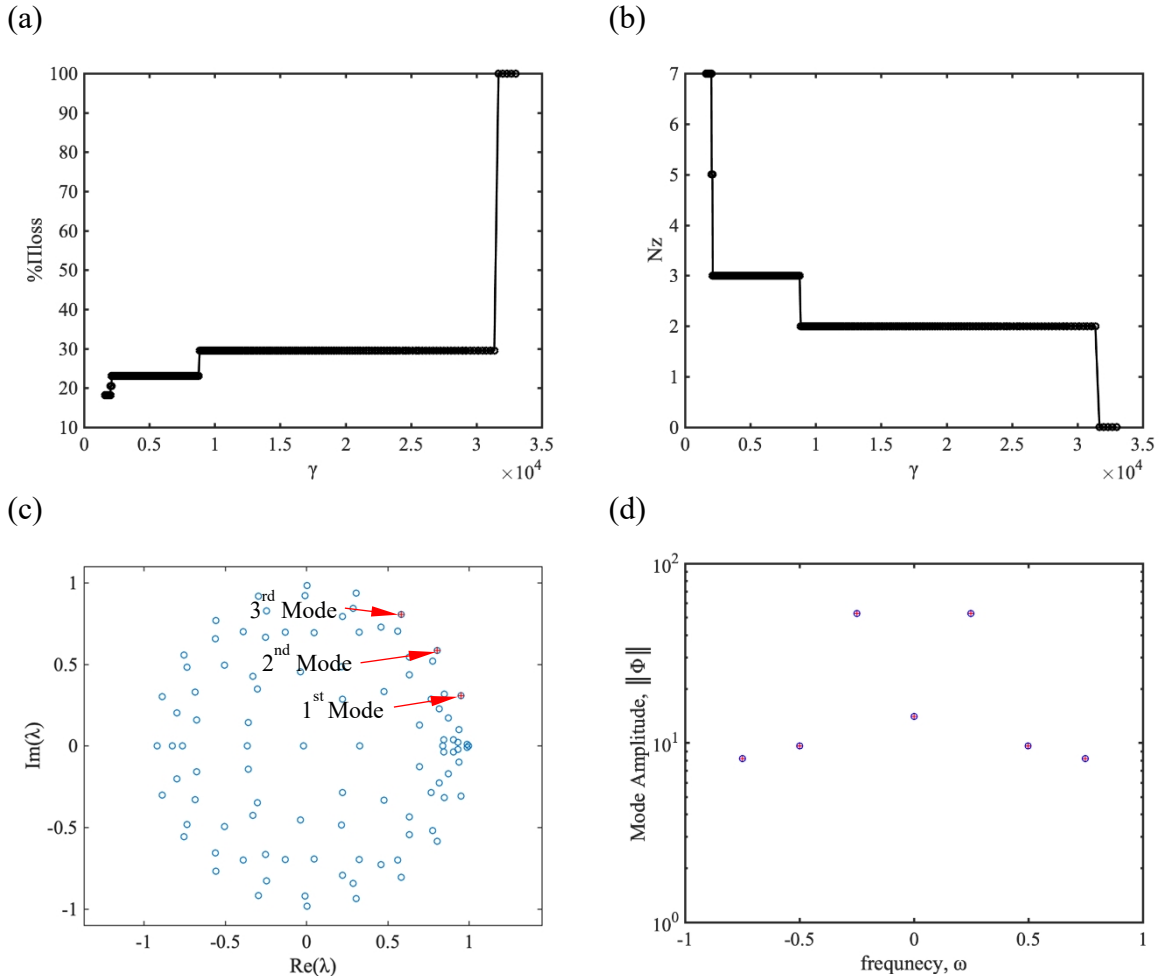

Figure 7.3 KC=11 (a) Performance loss $\%\Pi_{\text{loss}}$ of the optimal vector of amplitudes a with sparsity-promoting parameter gamma. (b) The function of the number of the retained DMD modes N_z with sparsity-promoting parameter gamma (c) Ritz values of the first three mode and (d) Mode amplitude vs frequency of full-rank DMD algorithm (blue circle) and reduced modes (red plus)

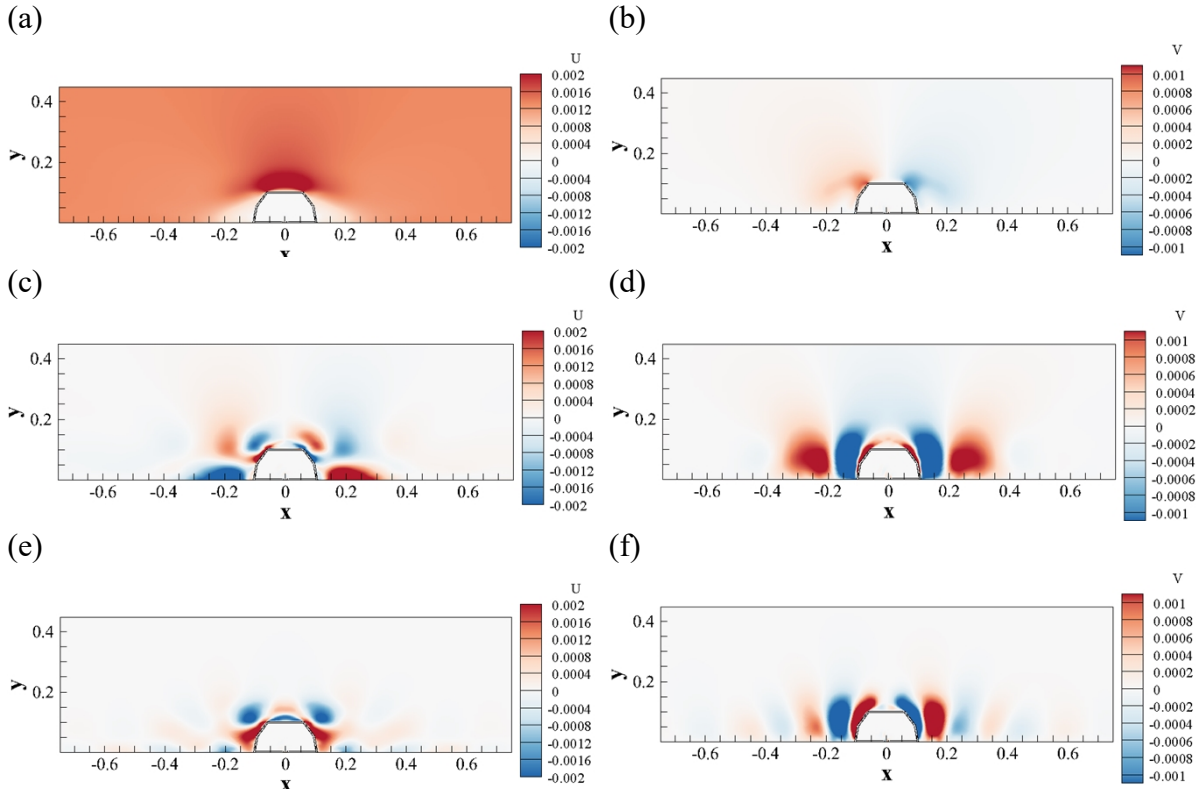

Figure 7.4 The first three spatial DMD modes for KC=11 (a), (c) and (e) real part of DMD modes (b), (d) and (f) imaginary part of DMD modes

7.3 Case 3-IV for KC=21

As can be seen in Figure 7.6, the KC=21 case with KC=5 and KC=11 are basically the same in the first and second mode, only with a greater intensity, and the case with KC=21 is essentially an enhanced version of KC=5 and KC=11. The increased KC number means having a larger velocity, vortex off along the cover toward the bottom while also continuously supplying energy at the top of the cover, thus dissipating and increasing the staggered energy forming the red and blue staggered block mode in Figure 7.6 (c), rather not the staggered stripes of KC=11 case shown in Figure 7.4 (f).

The same DMD analysis applied for KC=21 and shown in Figure 7.5. About 75% of the total energy is captured for 4 dominant modes number which are identified in Figure 7.5 (d). These modes shape is presented in Figure 7.6 by their streamwise and cross-stream velocities. Their according frequency are 0.25 s^{-1}, 0.5 s^{-1}, 0.75 s^{-1} and 1 s^{-1}, which are all multiples of the dominant frequency. The first and second modes show the similar pattern with KC=11, but stronger and further impact on sideward flow. The third and fourth modes correspond to the

third and fourth harmonic of the first mode respectively. It can be seen that there are unique red and blue mode blocks interlaced around the cover. And With the increasing frequency and decreasing amplitude of the higher order modes, the modes are no longer complete and continuous in the vertical direction. This is because for KC=5 and 11, the vortex is mainly shed off from two top corners of the subsea cover and there is seldom no vortex shed from the gap. While for KC=21, the strong vortex is shedding from the gap at the meantime the strong vortex is shedding from the top corner, shown in Figure 6.24. The two vortexes coexist and interact with each other. Therefore, the third mode well capture the vortex shed from the gap and the fourth mode shows the influence of vortex shed from top corner.

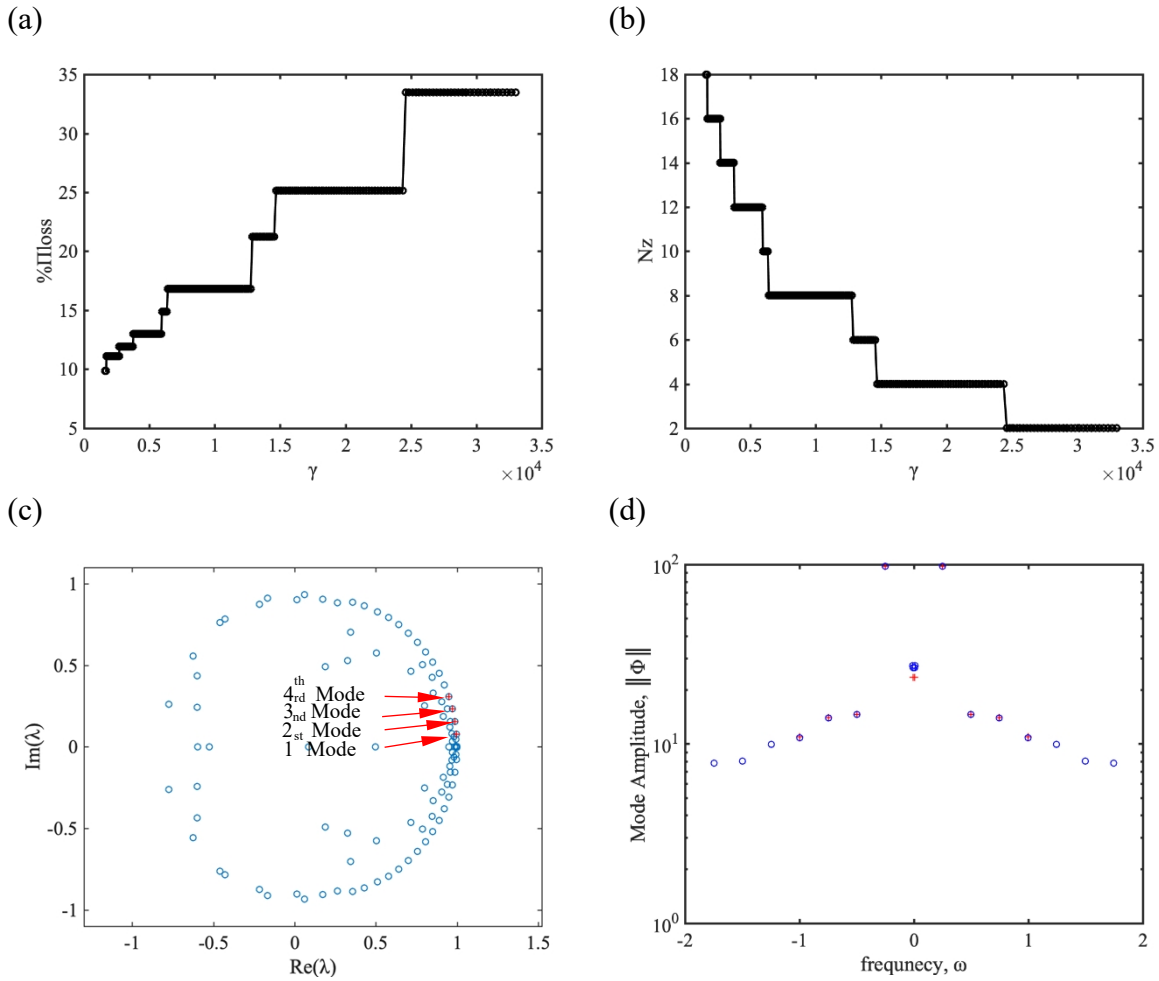

Figure 7.5 KC=21 (a) Performance loss $\%\Pi_{\text{loss}}$ of the optimal vector of amplitudes a with sparsity-promoting parameter gamma. (b) The function of the number of the retained DMD modes N_z with sparsity-promoting parameter gamma (c) Ritz values of the first four mode and (d) Mode amplitude vs frequency of full-rank DMD algorithm (blue circle) and reduced modes (red plus)

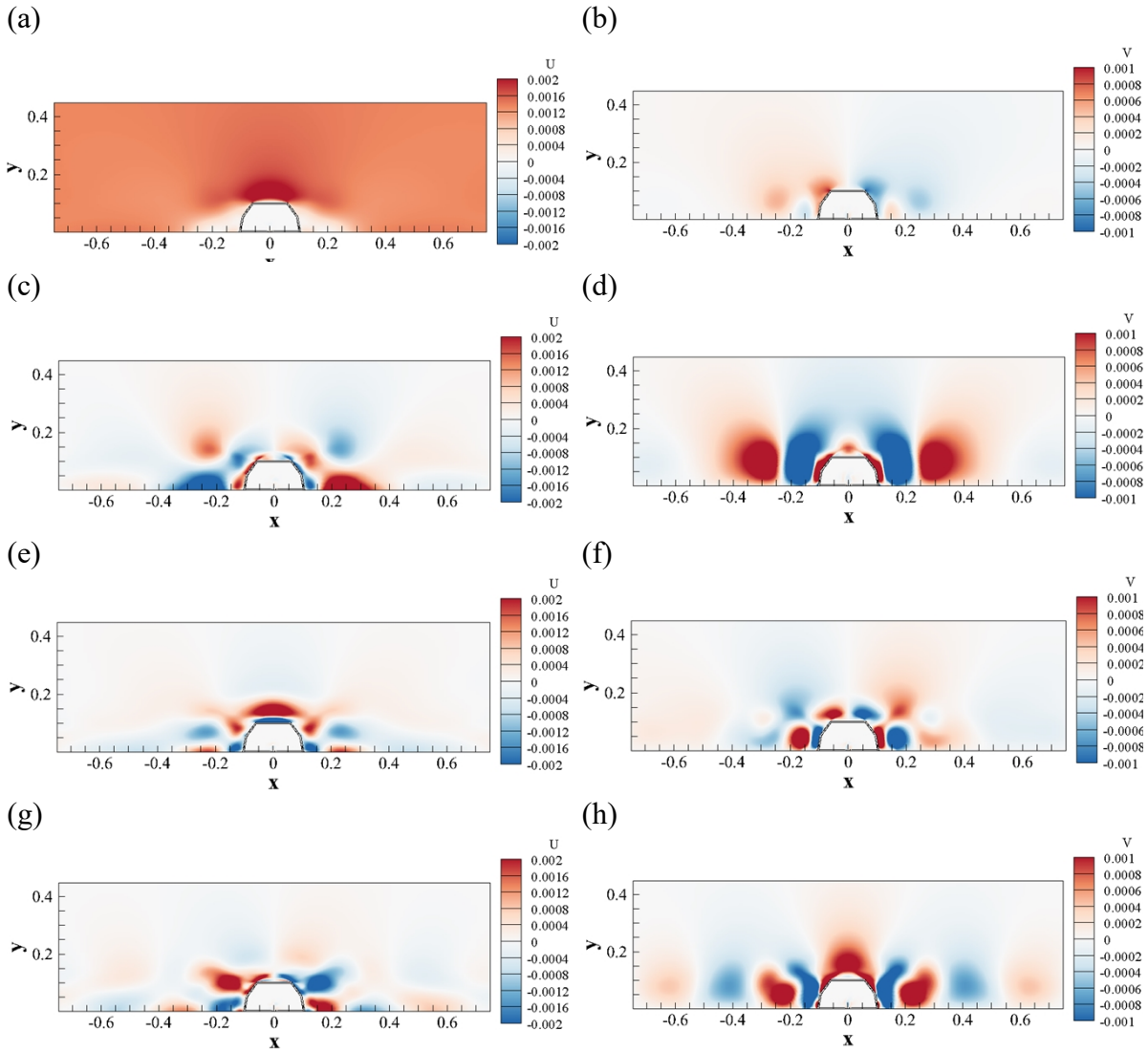

Figure 7.6 The first four spatial DMD modes for KC=21 (a), (c) (e) and (g) real part of DMD modes (b), (d), (f) and (h) imaginary part of DMD modes

7.4 Summary

This chapter illustrate the DMD analysis for the Case 3-IV for KC=5, 11 and 21. The reasonable compromise between the quality of approximation $\%\Pi_{loss}$ and the number of the retained DMD modes N_z is aim at capturing the dominant modes.

For KC=5, one dominant retained DMD modes $N_z$is chosen and keeping 80% of total energy. The frequency of the domain mode is equal to the characteristic frequency of the oscillatory flow. It is revealed that high velocity regions are located around the top corners of the subsea cover.

For KC=11, there are three modes capturing about 80 % of the total energy. The first mode is the same shape and meaning as KC=5 but the cross-stream velocity is more expanded around the corners of the subsea cover, and the second and the third modes are twice or second and third frequency and harmonic of first mode. The second mode indicates the advection of the shed vortices. The third mode shape is the similar to second mode but the length scales of the flow structures are becoming smaller.

For KC=21, 75% of total energy is captured for four dominant modes number. The first and second mode shape is similar to KC=11, revealing the energy advection. The third and fourth mode reveals the interlaced vortex shedding from the gap and the top corner of subsea cover.

8 Conclusion

Each chapter has the summary to present the results in details and here another brief conclusion.

By oscillating the subsea cover, the values of both the vertical force and the horizontal force are almost the same with those on a stationary subsea cover subjected to an oscillatory flow under the same KC number.

For all the investigated KC numbers, the time histories of F_x are similar to the experimental data. The maximum value of the present predicted F_x for the subsea cover case is slightly larger than that of the experimental data which may be due to the influence of the gap flow into the cover.

For KC=5 and 11, there are negative and positive parts in the time histories of the present predicted vertical forces F_z. The negative parts of F_z are overall in agreement with the experimental data while the positive parts are overestimated for the simulations. However, for large KC of KC=20, most of the values in the time histories of F_z are positive and they are comparable with the experiment data.

The amplitudes and the sizes of the spanwise vorticity increase with the increasing KC number. For KC=5 and 11, the vortex shedding around the top corners of the cover is weak and the vortices induced by the gap flow through the gap between the cover and the plate tend be localized around the bottom edges of the cover. The vertical structures inside cover can influence the vertical forces on the cover. For KC=5 and 11, there are two main large vortices inside the cover while for KC=20, there is only one large one.

Further revision to improve lift forces with different geometry subsea covers is conducted. The Case 1 emphasis on the only outer shell of subsea cover connected with domain and discuss the function of outer shell. It confirms that the external surface of the subsea cover plays a decisive role in the force, and the interaction in the unconnected area under cover with plate is directly related to the F_z. The Case 2 provides the foundation of replacing the plate with the domain bottom. The Case 3 compares a series of cover baffles with different lengths to prevent the water interaction with inside water, which corresponds to the subsea cover is immersed and limited in the water upside-down and due to the water gravity in the experiment set. The long baffle effectively blocks the water disturbance and keep the subsea cover as a whole. And the

longest baffle case reaches the acceptable results compared with experiment data and chosen as the final model used for further exploration.

Dynamic Mode Decomposition (DMD) is applied to capture the main modes for Case 3 at KC=5, 11 and 21. The reasonable compromise between the quality of approximation $\%\Pi_{loss}$ and the number of the retained DMD modes N_z. 75% ~80% of total energy is captured for these three KC numbers, there are 1 dominant mode for KC=5, 3 modes for KC=11 and 4 modes for KC=21. The first domain mode of each KC number with the same frequency with the frequency of oscillatory flow all reveal that high velocity that regions are located around the top corners of the subsea cover. The second and third of cases at KC=11 presents the advection of the shed vortices in different harmonic degree. While the third and fourth modes of cases at KC=21, interlaced pattern reveal the different phenomenon with the cases of KC=5 and KC=11 that the vortices shed from the gap have strong impact on the flow field and interaction with the vortices shed from the top corners of the subsea cover.

9 Recommendations for further work

In this paper, the reliability of the turbulence model has been fully verified and validated and the forces applied to the cover on the seabed have been well predicted by the study of different cover geometries and flow conditions. It is possible to address a few future research studies that would have great contribution to the topic. They are summarized as follows:

1. The whole paper is devoted to the specific structure of Base cover with no edge, 6.5 mm gap in the regular motion. Simulations for other geometries such as the width of the cover, the size of the gap, and the length of the edge need to be conducted and compared with experimental data for this numerical model.
2. The perforation and solidity ratio on the cover is a challenge for geometry set up and the 2D numerical simulation. This is also more demanding for the boundary layer and mesh. Therefore, a more complex 3D numerical model is recommended.
3. The experiments this study based on were performed using the subsea cover immersed in the water upside-down, which is unrealistic and lead to the limitation of water entrance to cover. Even though the same effect is obtained by using baffle, more realistic experimental data is essentially needed to refine the numerical model.

References

An, H., Cheng, L., & Zhao, M. 2011. Steady streaming around a circular cylinder near a plane boundary due to oscillatory flow. Journal of Hydraulic Engineering, 137(1), 23-33.

Andersen, M., Yin, G., & Ong, M. C. 2021. Numerical Simulations of Flow Around Wall-Mounted Square and Trapezoidal Structures at High Reynolds Numbers. Journal of Offshore Mechanics and Arctic Engineering, 143(1).

Antoine Placzek, Jean-François Sigrist, Aziz Hamdouni. Numerical Simulation of an Oscillating Cylin- der in a Cross-Flow at Low Reynolds Number: Forced and Free Oscillations. Computers and Fluids, Elsevier, 2009, 38 (1), pp.80-100. 10.1016/j.compfluid.2008.01.007. hal-01989261

Arie, M., kiya, M., Tamura, H., Kosugi, M., & Takaoka, K. 1975. Flow over rectangular cylinders immersed in a turbulent boundary layer: Part 2 flow patterns and pressure distributions. Bulletin of JSME, 18(125), 1269-1276.

Chen, C. C., Fang, F. M., Li, Y. C., Huang, L. M., & Chung, C. Y. 2009. Fluid forces on a square cylinder in oscillating flows with non-zero-mean velocities. International journal for numerical methods in fluids, 60(1), 79-93.

Firoozkoohi, R. 2014. Model tests of GRP covers in waves and current. MARINTEK.

Jones, W.P., Launder, B.E., 1973. The calculation of low-Reynolds-number phenomena with a two-equation model of turbulence. Int. J. Heat Mass Transfer. 16, 119-113

J. Fredsøe and M. B. Sumer, Hydrodynamics Around Cylindrical Structures (Revised Edition). World Scientific, Sep. 2006.

Lehnasch, G., Jouanguy, J., Laval, J. P. & Delville, J. (2011). POD Based Reduced-Order Model for Prescribing Turbulent Near Wall Unsteady Boundary Condition. In Progress in Wall Turbulence: Understanding and Modeling (pp. 301-308). Springer, Dordrecht.

Liu, Y. Z., Ke, F., & Sung, H. J. 2008. Unsteady separated and reattaching turbulent flow over a two-dimensional square rib. Journal of Fluids and Structures, 24(3), 366-381.

Martinuzzi, R., & Tropea, C. 1993. The flow around surface-mounted, prismatic obstacles placed in a fully developed channel flow. Transactions-American Society of Mechanical Engineers Journal of Fluids Engineering, 115, 85-85.

Massie W. W. and Journée J.M.J, Course Syllabus Offshore Hydromechanics, Delft University of Technology, January 2001

Menter, F.R., 1994. Two-equation eddy-viscosity turbulence models for engineering applications. AIAA J. 32, 1598–1605.

Menter, F. R., Kuntz, M., & Langtry, R. 2003. Ten years of industrial experience with the SST turbulence model. Turbulence, heat and mass transfer, 4(1), 625-632.

P.J. Schmid, Dynamic mode decomposition of numerical and experimental data, J. Fluid Mech. 656(7) (2010) 5–28.

Podvin, B. (2009). A proper-orthogonal-decomposition–based model for the wall layer of a turbulent channel flow. Physics of Fluids, 21(1), 015111.

Sayma, A. (2009). Computational Fluid Dynamics. Abdulnaser Sayma & Ventus Publishing ApS.

Schmid, P.J., 2010. Dynamic mode decomposition of numerical and experimental data. J. Fluid Mech. 656, 5–28.

Stenmark, E. (2013). On Multiphase Flow Models in ANSYS CFD Software ANSYS CFD Software (Unpublished doctoral dissertation).

Tauqeer, M. A., Li, Z., & Ong, M. C. 2017. Numerical simulation of flow around different wall-mounted structures. Ships and Offshore Structures, 12(8), 1109-1116.

Tong, F., Cheng, L., Zhao, M., & An, H. 2015. Oscillatory flow regimes around four cylinders in a square arrangement under small KC and Re conditions. Journal of Fluid Mechanics, 769, 298-336.

Versteeg, Henk & Malalasekera, W. (2021). An introduction to computational fluid dynamics: the finite volume method / H. K. Versteeg and W. Malalasekera.. SERBIULA (sistema Librum 2.0).

Wilcox, D.C., 1998. Turbulence Modeling for CFD, 2nd ed. DCW Ind., Inc., La Canada, CA.

Xiong, C., Cheng, L., Tong, F., & An, H. 2018. Influence of plane boundary proximity on the Honji instability. Journal of Fluid Mechanics, 852, 226-256.

Yang, K., Cheng, L., An, H., Bassom, A. P., & Zhao, M. 2013. The effect of a piggyback cylinder on the flow characteristics in oscillatory flow. Ocean engineering, 62, 45-55.

Yang, K., Cheng, L., An, H., Bassom, A. P., & Zhao, M. 2014. Effects of an axial flow component on the Honji instability. Journal of Fluids and Structures, 49, 614-639.

Yin, G., Andersen, M., & Ong, M. C. 2020. Numerical simulations of flow around two tandem wall-mounted structures at high Reynolds numbers. Applied Ocean Research, 99, 102124.